

**PERFORMANCE ANALYSIS OF VERTICAL AXIS WIND
TURBINE INTEGRATED WITH OMNI
DIRECTION-GUIDE-VANE**

BEHZAD SHAHIZARE

**FACULTY OF ENGINEERING
UNIVERSITY OF MALAYA
KUALA LUMPUR**

2017

**PERFORMANCE ANALYSIS OF VERTICAL AXIS
WIND TURBINE INTEGRATED WITH OMNI
DIRECTION-GUIDE-VANE**

BEHZAD SHAHIZARE

**THESIS SUBMITTED FOR FULFILMENT OF THE
REQUIREMENTS FOR THE DEGREE OF DOCTOR OF
PHILOSOPHY**

**FACULTY OF ENGINEERING
UNIVERSITY OF MALAYA
KUALA LUMPUR**

2017

**UNIVERSITI MALAYA
ORIGINAL LITERARY WORK DECLARATION**

Name of candidate: BEHZAD SHAHIZARE

Registration /Matric No: **KHA 130072**

Name of Degree: **Doctor of Philosophy**

Title of Thesis (“this work”):

**Performance Analysis of Vertical Axis Wind Turbine Integrated with
Omni Direction-Guide-Vane**

Field of study: **ENERGY**

I do solemnly and sincerely declare that:

1. I am the sole author/writer of this Work;
2. This Work is original;
3. Any use of any work in which copyright exists was done by way of fair dealing and for permitted purposes and any excerpt or extract from, or reference to or reproduction of any copyright work has been disclosed expressly and sufficiently and the title of the Work and its authorship have been acknowledged in this Work;
4. I do not have any actual knowledge nor do I ought reasonably to know that the making of this work constitutes an infringement of any copyright work;
5. I hereby assign all and every rights in the copyright to this Work to the University of Malaya (“UM”), who henceforth shall be owner of the copyright in this work and that any reproduction or use in any form or by any means whatsoever is prohibited without the written consent of UM having been first had and obtained;
6. I am fully aware that if in the course of making this Work I have infringed any copyright whether internationally or otherwise, I may be subject to legal action or any other action as may be determined by UM.

Candidate’s Signature

Date

Subscribed and solemnly declared before,

Witness’s Signature

Date

Name

Designation

ABSTRACT

Wind energy is the conventional source of clean and renewable energy and it is the fastest-growing source of sustainable energy in the world. Numerical computation can offer important insight and data that are either difficult or expensive to measure or to perform tests experimentally. In this dissertation, we used the Computational Fluid Dynamics (CFD) to present effects of the Omni Direction Guide Vane shape on the performance of a H-rotor Vertical Axis Wind Turbine (VAWT). For this purpose, five straight-bladed VAWTs have been simulated via the Computational Fluid Dynamics (CFD). Hence, the VAWTs without the ODGV covering were simulated and validated via the Experimental Fluid Dynamics (EFD) data. The grid and time step independence test, as well as the effect of the domain size and turbulence model have been conducted. In the next step, the VAWT was shrouded by the ODGV cover and simulated by the coupling of the CFD and RSM method in different shapes and angle conditions. Results of this study indicates that the output power of the VAWT with $\alpha=55^\circ$ and $\beta=20^\circ$ ODGV guide vanes angles has been improved by 12%, 56% and 29% respectively at three different TSRs including 0.8, 1.2 and 1.6. Furthermore, all the shape ratios had a positive effect on the power and torque coefficient improvement when the TSR is higher than one. Moreover, results showed that the best case has a shape ratio of 0.55, which improves the power coefficient by 56%. In the final step, result of the optimized ODGV was compared with three different types of guide vanes in different flow angles. Results showed an optimized ODGV had the best improvement in terms of performance of the VAWT compared to the 4, 5, 6 bladed ODGVs. Optimized ODGV also showed the lowest sensitivity in different flow angles as well as being fabricated and tested in lab test conditions to validate the numerical findings.

ABSTRAK

Tenaga angin adalah sumber konvensional tenaga bersih dan boleh diperbaharui dan ia adalah sumber yang paling pesat berkembang tenaga mampan di dunia. Pengiraan berangka boleh menawarkan wawasan penting dan data yang sama ada sukar atau mahal untuk mengukur atau untuk melaksanakan ujian uji kaji. Dalam kajian ini, kami menggunakan dinamik bendalir pengiraan (CFD) untuk membentangkan kesan Omni Direction Panduan Vane bentuk kepada prestasi yang H-rotor Vertical Axis Wind Turbine (VAWT). Bagi tujuan ini, lima VAWTs lurus bilah telah simulasi melalui dinamik bendalir pengiraan (CFD). Oleh itu, VAWTs tanpa penutup ODGV itu simulasi dan disahkan melalui Eksperimen Dynamics Fluid data (EFD). Grid dan masa ujian langkah kemerdekaan, dan juga kesan saiz domain dan model gelora telah dijalankan. Dalam langkah seterusnya, VAWT telah diselubungi oleh perlindungan ODGV dan disimulasikan dengan gandingan kaedah CFD dan RSM dalam pelbagai bentuk dan keadaan sudut. Hasil kajian ini menunjukkan bahawa kuasa output VAWT dengan $\alpha = 55^\circ$ dan $\beta = 20^\circ$ ODGV panduan ram sudut telah meningkat sebanyak 12%, 56% dan 29% masing-masing di tiga TSR berbeza termasuk 0.8, 1.2 dan 1.6. Tambahan pula, semua nisbah bentuk mempunyai kesan positif ke atas kuasa dan tork peningkatan pekali apabila TSR adalah lebih tinggi daripada satu. Selain itu, keputusan menunjukkan bahawa kes ini mempunyai nisbah bentuk 0,55, yang meningkatkan pekali kuasa sebanyak 56%. Pada langkah terakhir, hasil ODGV dioptimumkan telah dibandingkan dengan tiga jenis bilah pandu di sudut aliran yang berbeza. Keputusan menunjukkan ODGV dioptimumkan mempunyai peningkatan yang terbaik dari segi prestasi VAWT berbanding dengan 4, 5, 6 ODGVs berbilang. ODGV dioptimumkan juga menunjukkan sensitiviti yang paling rendah di sudut aliran yang berbeza serta yang direka dan diuji dalam keadaan ujian makmal memperbaiki data berangka.

ACKNOWLEDGMENTS

First and foremost, I wish sincere gratitude to my supervisors, Prof Dr. Nik Nazri bin Nik Ghazali and Prof. Dr. Wen Tong Chong for their guidance and advice for this thesis and research. Working with them have been a fruitful learning and research experience. The writing of the thesis had been the most challenging task of my life to date. I could not have completed this work without the support and help of many people. I would also like to convey thanks to University Malaya for providing the financial support and laboratory facilities. I would also like to thank my colleague Mr. Saeed Tabatabaekia for the useful discussions and help in all steps of my study. Last but not the least; heartfelt thanks are extended to my parents and my sister for their support and encouragement. Sincere thanks also to my wife Mahdokht for her continuous support and faith in me during my times of hardship...

TABLE OF CONTENT

Abstract	iii
Abstrak	iv
Acknowledgment	v
Table of Content.....	vi
List of Figures	xi
List of Tables.....	xvii
List of Symbols and Abbreviations	xviii
CHAPTER 1: INTRODUCTION.....	1
1.1 CLASSIFICATION OF WIND TURBINES	2
1.1.1 VAWTs Historic Background.....	4
1.1.2 Vertical Axis Wind Turbines Categories	5
1.1.2.1 Darrieus Lift-Based VAWT.....	6
1.1.2.2 Savonius-Drag Based VAWT.....	7
1.2 AUGMENTED TURBINES	8
1.2.1 VAWT with Guide Vanes.....	9
1.3 OBJECTIVES	11
CHAPTER 2: LITERATURE REVIEW	12
2.1 COMPUTATIONAL FLUID DYNAMICS	12
2.1.1 RANS based CFD	14
2.1.2 Dynamic Stall Phenomenon.....	18
2.2 AUGMENTED WIND TURBINES	29
2.3 SUMMARY	34

CHAPTER3: METHODOLOGY	36
3.1 AERODYNAMICS THEORY AND PERFORMANCE	
CHARACTERISTICS.....	36
3.1.1 Lift Force.....	37
3.1.2 Drag Force.....	38
3.1.3 Reynolds number	40
3.1.4 Blade Solidity.....	41
3.1.5 Tip Speed Ratio.....	41
3.1.6 Bezt Number	41
3.1.7 Rotor Performance Parameters	43
3.2 RESPOND SURFACES METHODOLOGY	44
3.2.1 Response Surface Methods and Designs	45
3.2.2 Designs for Fitting Second-Order Model.....	46
3.3 EXPERIMENTAL TEST ON THE OPTIMIZED ODGV	48
3.3.1 Fabrication of the ODGV.....	49
3.3.2 Wind Turbine	52
3.3.2.1 Major Components of the Wind Turbine.....	54
3.3.2.2 Installation Process of the Wind Turbine	54
3.3.3 Augmented turbine.....	57
3.3.4 Blowing fans	57
3.3.5 Measurements Apparatus	58
3.3.5.1 Anemometer.....	58
3.3.5.2 Dynamometer.....	59

3.3.6	Dynamometer Startup Procedure	61
3.4	NUMERICAL MODELING	62
3.4.1	GEOMETRY OF VAWT	62
3.4.2	GEOMETRY OF ODGV	63
3.4.3	CFD Solver	64
3.4.4	The wind tunnel numerical domain.....	64
3.4.5	Mesh generation and boundaries.....	67
3.4.6	Blades Y_{plus}	70
3.4.7	Domain Size	71
3.4.7.1	Side Wall Distance d_s	71
3.4.7.2	Outlet Distance d_o	72
3.4.8	Mesh Dependency Study.....	73
3.4.9	Time dependency study.....	76
3.4.10	Turbulence Modelling and Dynamic Stall.....	77
3.4.10.1	$k-\varepsilon$ vs. $k-\omega$ Turbulence modeling.....	81
3.4.11	CFD Validation.....	85
3.4.11.1	Power Coefficient	86
3.5	SUMMARY	89
CHAPTER 4: RESULTS AND DISCUSSION.....		90
4.1	THE PERFORMANCE OF THE TURBINE WITHOUT ODGV	90
4.1.1	Power Coefficient.....	90
4.2	VISUALIZATION	94

4.2.1 Time-Averaged Flow Patterns	94
4.2.2 Pressure Contours	94
4.3 INFLUENCE OF THE ODGV ANGLES.....	95
4.4 RESPOND SURFACE METHODOLOGY RESULTS	96
4.4.1 Velocity Vectors.....	111
4.5 INFLUENCE OF THE ODGV SHAPE RATIO	112
4.6 THE EFFECT OF THE NUMBER OF GUIDE VANES	121
4.6.1 ODGV with Four Bladed Guide Vane	122
4.6.1.1 Power Coefficient of the Augmented VAWT with Four Bladed ODGV	122
4.6.1.2 Torque Coefficient of the Augmented VAWT with Four Bladed ODGV	124
4.6.1.3 Visualization of the Augmented VAWT with Four Bladed ODGV....	126
4.6.2 ODGV with Five Bladed Guide Vane	127
4.6.2.1 Power Coefficient of the Augmented VAWT with Five Bladed ODGV	127
4.6.2.2 Torque Coefficient of the Augmented VAWT with Five Bladed ODGV	129
4.6.2.3 Visualization of the Augmented VAWT with Four Bladed ODGV....	132
4.6.3 ODGV with Six Bladed Guide Vanes.....	133
4.6.3.1 Power Coefficient of the Augmented VAWT with Six Bladed ODGV	133

4.6.3.2 Torque Coefficient of the Augmented VAWT with Six Bladed ODGV	135
4.6.3.3 Visualization of the Augmented VAWT with Six Bladed ODGV	137
4.6.4 Comparison between Optimized and Conventional ODGV's	139
4.7 RESULTS OF THE LAB TEST	142
4.7.1 Open Rotor Case	142
4.7.2 Augmented Turbine Cases	143
4.8 SUMMARY	145
CHAPTER 5: CONCLUSION AND RECOMMENDATION	147
5.1 SUGGESTIONS FOR FURTHER RESEARCH.....	148
References	149
List of Publications: Journal Papers	158
Appendix	159

LIST OF FIGURES

Figure 1.1: World energy demand and population predictions: 1980–2030 (Doman & Conti, 2010).....	1
Figure 1.2: Examples of wind turbines: a) drag VAWT, b) lift HAWT and c) lift VAWT.....	2
Figure 1.3: Persian windmill (Manwell et al., 2002).....	5
Figure 1.4: H rotor Darrieus wind turbine (Akwa, Vielmo, & Petry, 2012).....	7
Figure 1.5: Savonius rotor (Cooper & Kennedy, 2004).....	7
Figure 1.6: VAWT with Omni-Direction-Guide-Vane (Carlos Simao Ferreira, van Bussel, & Van Kuik, 2007b).	11
Figure 2.1: C_p curves of wind tunnel model (Howell, Qin, Edwards, & Durrani, 2010).....	15
Figure 2.2: VAWT C_p for 2D, effective 2D, and experiments(K. McLaren et al., 2012).....	16
Figure 2.3: Spin down and CFD C_p results(J. M. Edwards et al., 2012).....	17
Figure 2.4: An illustration of the dynamic stall process (adapted from(Simon Charles McIntosh, 2009)).....	19
Figure 2.5: Vorticity plots of turbulence model study(Carlos Simao Ferreira et al., 2007a).....	22
Figure 2.6: Lift hysteresis loops for a VAWT blade(Amet et al., 2009).	25
Figure 2.7: Lift coefficient predictions of different turbulence models (J. M. Edwards et al., 2012).....	28
Figure 2.8: Power coefficient plot of wind tunnel scale VAWT (Danao & Howell, 2012).....	29
Figure 2.9: Stream tube comparison between a conventional wind turbine and a DAWT.....	30

Figure 2.10: Torque coefficient contribution of single blade for different diffuser nozzle	33
Figure 3.1: VAWT model.(Templin, 1974).	37
Figure 3.2: Local forces on a blade.	38
Figure 3.3: Airflow around an airfoil.	39
Figure 3.4: Rotor efficiency vs. downstream / upstream wind speed ratio(Patel, 1999).....	43
Figure 3.5: Response surface plot $y = f(x_1, x_2) + e$	45
Figure 3.6: Sample of Contour plot in RSM.	46
Figure 3.7: Central Composite Design for $q = 2$	47
Figure 3.8: Schematic view of the experimental test.	49
Figure 3.9: Top view of the ODGV.	50
Figure 3.10: Guide rails.....	51
Figure 3.11: Assembled ODGV.....	52
Figure 3.12: Wind turbine.....	53
Figure 3.13: Installation of the pillar to the generator.....	55
Figure 3.14: Connection between pillar and test rig.	55
Figure 3.15: supporting arms.	56
Figure 3.16: Assembled augmented VAWT.	57
Figure 3.17: Series of the blowing fans.....	58
Figure 3.18: Dynamometer front view.	59
Figure 3.19: Dynamometer back view.	60
Figure 3.20: Interface of the dynamometer controller in computer.	61
Figure 3.21: 3-D model of the VAWT	62
Figure 3.22: Three-dimensional model of the ODGV.	63
Figure 3.23: Top view of VAWT intgrated with ODGV.....	63

Figure 3.24: Wind tunnel (Domain).....	65
Figure 3.25: Boundary around VAWT.	67
Figure 3.26: Density of the mesh near the blade.....	68
Figure 3.27: Boundary layers mesh around blade.....	69
Figure 3.28: Control ellipse.....	69
Figure 3.29: Results for Y_{plus} values at TSR=1.6.....	70
Figure 3.30: Blockage study results.	72
Figure 3.31: Domain length (Outlet Distance) study results for the 2D numerical model.....	73
Figure 3.32: Mesh dependency test in TSR=1.2.	75
Figure 3.33: Variation of the C_p in different types of mesh in TSR=1.2.....	76
Figure 3.34: Time dependency study.	77
Figure 3.35: Prediction of the C_m using different turbulence models.	84
Figure 3.36: Deviation of the C_p results from experiments in different turbulence models.	84
Figure 3.37: Configuration of the testing unit in wind tunnel.....	85
Figure 3.38: Results of the coefficient of the power in wind tunnel experimental test data compared to the CFD simulation.....	87
Figure 3.39: Published results from other studies showing the difference between 2D and 3D data.....	88
Figure 4.1: Performance of the bare VAWT.....	91
Figure 4.2: Torque coefficient variation at different TSR.....	92
Figure 4.3: Predicted torque coefficient for five individual blades.....	93
Figure 4.4: Average C_m for different TSRs.....	93
Figure 4.5: vorticity contours a) TSR=0.8, b) TSR=1.2, c) TSR=1.6.....	94
Figure 4.6: pressure contours a) TSR=0.8, b) TSR=1.2, c) TSR=1.6.	95

Figure 4.7: Normal probability plot of residuals in angle optimization.....	97
Figure 4.8: Predicted model Vs. actual results in angle optimization.	98
Figure 4.9: Residuals versus predicted for C_p in internally studentized for angle optimization.....	99
Figure 4.10: Predicted versus runs for C_p for angle optimization.	100
Figure 4.11: Influence of the angles on the VAWT C_p at TSR=0.8.....	101
Figure 4.12: Influence of the angles on the VAWT C_p at TSR=1.2.....	102
Figure 4.13: influence of the angles on the VAWT C_p at TSR=1.6.....	103
Figure 4.14: percentage of C_p improvements at different design points and TSRs.	104
Figure 4.15: C_p variations based on different angle (β and α) of the ODGV walls.	105
Figure 4.16: Percentage improvements of the C_p at different ODGV angles at TSR=1.2.	106
Figure 4.17: Maximum C_p at ranges of different α and β	106
Figure 4.18: Minimum C_p in different ranges of α and β	107
Figure 4.19: Comparison of the C_p with and without ODGV at three tested TSR..	108
Figure 4.20: ODGV impact on C_m of the VAWT in various azimuth angles at TSR=1.2.	109
Figure 4.21: Torque coefficient (C_m) variation in one rotation with different ODGV angles at TSR=1.2.	110
Figure 4.22: Vectors around the domain in different guide vane angles.	111
Figure 4.23: Schematic view of the investigating factors.	113
Figure 4.24: Influence of the variation of the outer diameter at $\psi=0^\circ$ and $L=100$ (a), $L=200$ (b), $L=300$ (c).	114
Figure 4.25: Influence of the variation of the outer diameter at $\psi=22.5^\circ$ and $L=100$ (a), $L=200$ (b), $L=300$ (c).	115

Figure 4.26: Influence of the variation of the outer diameter at $\psi=45^\circ$ and $L=100$ (a), $L=200$ (b), $L=300$ (c).	116
Figure 4.27: Torque coefficient versus azimuth angle at different shape ratios of the ODGV including the open rotor case at $TSR=1.2$	117
Figure 4.28: Average torque coefficient versus TSR for different shape ratios of the ODGV.	118
Figure 4.29: Torque coefficient versus Azimuth angle for open and augmented rotor at $TSR=1.2$, $R=0.55$	119
Figure 4.30: Power coefficient versus TSR for open and augmented rotors.	120
Figure 4.31: Percentage of the improvement of C_p using different $R_{shape\ ratio}$	121
Figure 4.32: Schematic view of the number of the guide vanes.	121
Figure 4.33: C_p vs. TSR at $\#G.V=4$ at different flow angles.....	123
Figure 4.34: Variation of the C_p at different TSRs and flow angles in $\#G.V=4$	123
Figure 4.35: C_m Vs. azimuth in $\#G.V=4$ at different flow angles, $TSR=0.8$	124
Figure 4.36: C_m vs. azimuth in $\#G.V=4$ at different flow angles, $TSR=1.2$	125
Figure 4.37: C_m vs. azimuth in $\#G.V=4$ at different flow angles, $TSR=1.6$	125
Figure 4.38: Vorticity contour in $\#G.V=4$ around blade number3.....	127
Figure 4.39: C_p Vs. TSR in $\#G.V=5$ at different flow angles.	128
Figure 4.40: Variation of the C_p at different TSR and flow angles in $\#GV=5$	129
Figure 4.41: C_m vs. azimuth in $\#G.V=5$ at different flow angles, $TSR=0.8$	130
Figure 4.42: C_m vs. azimuth in $\#G.V=5$ at different flow angles, $TSR=1.2$	130
Figure 4.43: C_m vs. azimuth in $\#G.V=5$ at different flow angles, $TSR=1.6$	131
Figure 4.44: Vorticity contour in $\#G.V=5$ around blade number3.....	133
Figure 4.45: C_p vs. TSR in $\#G.V=6$ at different flow angles.....	134
Figure 4.46: Variation of the C_p at different TSR and flow angles in $\#GV=6$	134
Figure 4.47: C_m vs. azimuth in $\#G.V=6$ at different flow angles, $TSR=0.8$	135

Figure 4.48: C_m vs. azimuth in #G.V=6 at different flow angle, TSR=1.2.	136
Figure 4.49: C_m vs. azimuth in #G.V=6 at different flow angle, TSR=1.6.	137
Figure 4.50: Vorticity contour at #G.V=6 around blade number3.....	138
Figure 4.51: C_p vs. TSR using different ODGV numbers at $\psi=0^\circ$	139
Figure 4.52: C_p vs. TSR using different ODGV number at $\psi=22.5^\circ$	140
Figure 4.53: C_p vs. TSR using different ODGV number at $\psi=45^\circ$	141
Figure 4.54: Validation of the lab test with wind tunnel.....	142
Figure 4.55: C_p vs. TSR in lab test and CFD while #G.V=4.	143
Figure 4.56: C_p vs. TSR in lab test and CFD while #G.V=5.....	144
Figure 4.57: C_p Vs. TSR in lab test and CFD while #G.V=6.	144
Figure 4.58: C_p vs. TSR in lab test and CFD in <i>OPT.</i> ODGV.....	145

LIST OF TABLES

Table 3.1: Properties of the wind turbine and airfoil.	54
Table 3.2: blowing fans specification	58
Table 3.3: Mesh properties.....	74
Table 4.1: Design points of the different angle of the ODGV.	96
Table 4.2: Shape ratio of the ODGV.....	112
Table 4.3: Optimized ODGV configuration.....	139

University of Malaya

LIST OF SYMBOLS AND ABBREVIATIONS

Symbol	Description	Unit
A	Swept turbine area	m ²
C	Blade chord length	mm
CFD	Computational fluid dynamics	
C_m	Torque coefficient	
C_p	Power coefficient	
D	Turbine diameter	mm
EFD	Experimental fluid dynamics	
GIT	Grid independency test	
HAWT	Horizontal axis wind turbines	
L	Length of the blade	mm
N	Number of blades	
ODGV	Omni-direction-guide-vane	
R	Radius of the wind turbine	mm
t	Thickness of the blade	mm
RANS	Reynolds Averaged Navier Stokes	
R _g	Radius of the rotating grid	mm
SST	Shear Stress Transport	
TSR	Tip speed ratio	
VAWT	Vertical axis wind turbine	
$R_{\text{shape ratio}}$	Shape ratio of the ODGV (D_i ODGV/ D_o ODGV)	
D_i	Inner diameter of the ODGV	mm
D_o	Outer diameter of the ODGV	mm
ODGV		
Greek		
α	Second angle of ODGV	Degree (°)
β	First angle of ODGV	Degree (°)
θ	Azimuth angle	Degree (°)
v	Air flow speed	m/s
ω	Turbine angular velocity	rad
Subscript		
g	Grid	
m	Mechanical Torque	N.m
P	Power	Watt

CHAPTER 1: INTRODUCTION

A general consensus has been made in the recent years that the effects of climate change is becoming more severe and prevalent (West et al., 2009). The main cause of the increasing rate of undesirable climatic conditions were identified as greenhouse gas emissions from the burning of fossil fuels used primarily for energy generation and transportation purposes. According to the United Nations Secretariat (Passel et al., 2007), the world's population in 2030 will exceed 8.3 billion. During this time, the world's energy demand will increase from 138.5 Terawatt hour to 678 Tera Watt hour(TWh)(Doman & Conti, 2010), as shown in Figure 1.1.

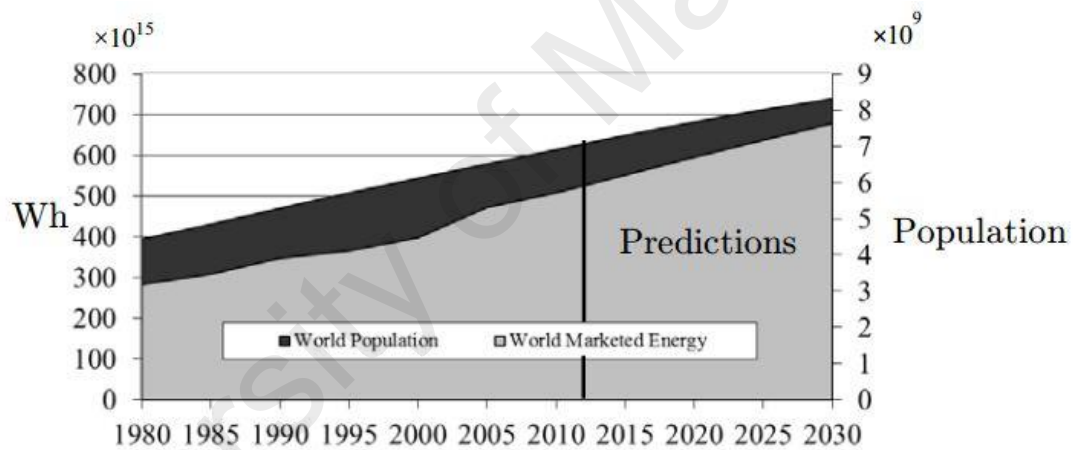


Figure 1.1: World energy demand and population predictions: 1980–2030 (Doman & Conti, 2010).

For this reason, there has been a pressing need to reduce emissions using technologies that are capable of extracting energy from the environment whilst being non-polluting and sustainable. Several alternative sources to fossil fuels have been identified: tidal, solar, biomass, and wind. These are branded as ‘renewables’ and have attracted significant research attention in the past decades. of these renewable sources, the contribution of wind to the total energy generation of the U.K. has been steadily rising over the last few years and has seen the greatest increase in 2011 by 68% for offshore installations and 45% for onshore (Panwar, Kaushik, & Kothari, 2011). Wind

has also been the leading renewable technology for electricity generation with 45% of the total 2011 renewable production. Despite these numbers, the total consumption of electricity from renewable sources only account for 9.4%. And the proportion of wind in the overall consumption is very low at 0.7% (Panwar et al., 2011). As a result, further research is needed to increase the understanding of this renewable power source to promote its wider adoption.

1.1 CLASSIFICATION OF WIND TURBINES

Wind turbines can be broken down into two general types: drag machines (Figure 1.3a) and lift machines (Figure 1.3b & c). Drag machines generate forces through the creation of large separated flows and move slower than the wind. The most common application of these devices is in water pumping. In lift machines, the wind is made to follow a curved path as it passes about a rounded object. The turning of the fluid generates forces on the object, typical of an airfoil profile, thus producing the required thrust. Blade speeds are often greater than the wind speed and far exceeds what is possible in drag machines. Lift machines are thus the more favorable from an energy production view point due to a greater potential for energy extraction (Bhuyan & Biswas, 2014).



(a)

(b)

(c)

Figure 1.2: Examples of wind turbines: a) drag VAWT, b) lift HAWT and c) lift VAWT.

There are two main methods of extracting energy by utilizing the lift concept: Horizontal axis wind turbines or HAWTs and vertical axis wind turbines or VAWTs. HAWTs have received significant research and development work over the decades, giving them a well-established and mature technology base that makes them the preferred configuration in all large-scale wind farm installations. VAWTs on the other hand have not been given the same attention. The complex aerodynamic and structural aspects of a VAWT operation make their understanding and optimization difficult, which is one of the reasons why they are less favored than their horizontal counterparts.

There are several points of contention on the use of VAWTs over HAWTs. The key point that prevails is the generally perceived superior performance of HAWTs over VAWTs. Nevertheless, VAWTs present a number of potential advantages over HAWTs when it comes to applications in a built environment:

- Easier maintenance because of the rotor's proximity to the ground (Shahzad, Asim, Mishra, & Paris, 2013). VAWTs are typically smaller in scale and mounted on masts that are many times shorter than conventional HAWT installations. Additionally, the rotor sits on a bearing and drives the generator below it.
- No need to yaw to the wind, thus reducing the efficiency loss when tracking changes in wind direction (Alaimo, Esposito, Messineo, Orlando, & Tumino, 2015; Elkhoury, Kiwata, & Aoun, 2015; Huang, Ma, Chen, Seki, & Aso, 2014; Ismail & Vijayaraghavan, 2015; Scheurich, Fletcher, & Brown, 2011).
- Sound emissions are usually lower as they operate at lower tip speed ratios (Iida, Mizuno, & Fukudome, 2004a).
- This can also reduce structural issues such as vibrations that result from high centrifugal forces.

- Potentially lower manufacturing costs due to the simplicity of the straight blade shape.
- Better performance in a skewed flow (Mertens, van Kuik, & van Bussel, 2003; Scheurich et al., 2011; Tescione, Ragni, He, Ferreira, & van Bussel, 2014).

VAWTs however are not without their disadvantages when compared to HAWTs.

The most common are:

- Lower efficiency due to the additional drag of blades moving against the wind. Moreover, HAWTs are presumably more optimized in their design as a consequence of greater efforts made in research and development.
- Less access to stronger winds in higher elevations.
- Complex aerodynamics resulting in continuously fluctuating blade loading during operation, which causes a lower fatigue life cycle.
- Difficult to implement variable pitch without complicated mechanisms. HAWT blades can be pitched easily to the optimum angle of attack to maximize energy extraction.

1.1.1 VAWTs Historic Background

The origin of VAWTs can be traced back to roots in Persia (Jha, 2011; Manwell, McGowan, & Rogers, 2002). The windmill was used as a source of mechanical power in the tenth century. Inhabitants, who lived in Eastern Persia, utilized the windmills as vertical-axis and drag type of windmills illustrated in Figure 1.3 . The invention of the vertical-axis windmills subsequently spread in the twelfth century throughout the Middle East as well as beyond to the Far East. The basic mechanisms of the primitive vertical-axis windmills were used in later centuries such as placing the sails above the millstones. This elevated the driver to a more open exposure, which improved the

output by exposing the rotor to higher wind speeds, and using reeds instead of cloth to provide the working surface (Jha, 2011).

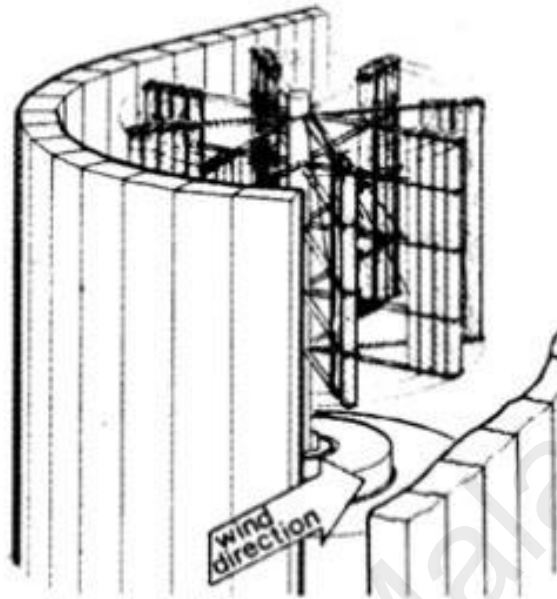


Figure 1.3: Persian windmill (Manwell et al., 2002).

A transition was witnessed from the windmills supplying mechanical power to wind turbines generating electrical power, which occurred toward the end of the nineteenth century. The initial use of wind for electricity generation as opposed to mechanical power has led to the successful commercial development of small wind generators, further research as well as experiments with large turbines. It is also worthy to note that the development of the aircraft industry in the early part of twentieth century facilitated rapid advances in airfoils which could immediately be applied to the improvement of the wind turbine (Manwell et al., 2002).

1.1.2 Vertical Axis Wind Turbines Categories

Two major types of vertical axis wind turbines are commercialized today in the wind energy market: Darrieus and Savonius types. The following section will provide an overview of these turbines.

1.1.2.1 Darrieus Lift-Based VAWT

Invented by F.M. Darrieus in the 1930s, Darrieus turbines are lift-based turbines designed to function on the aerodynamic principle of airplanes (Devine-Wright, 2005). The rotor blades are designed as an airfoil in the cross section so that the wind travels a longer distance on one side (convex) than the other side (concave). As a result, the wind speed is relatively higher on the convex side. If Bernoulli's equation is applied, it can be shown that the differential in wind speed over the airfoil creates a differential pressure, which is used to pull the rotor blade around as the wind passes through the turbine. The Darrieus VAWT is primarily a lift-based machine, which is a feature that makes it compete in performance with the conventional HAWTs. Figure 1.4 shows a typical Darrieus wind turbine characterized by its H-shaped rotor. It is normally built with two or three rotor blades. It has a low starting torque but a high rotational speed, making it suitable for coupling with an electrical synchronous generator. For a given rotor size, weight and cost, its power output is higher than any drag-based VAWTs. However, the Darrieus VAWT suffers a disadvantage by not self-starting. Experimental studies of Savonius – Darrieus wind turbines have been conducted (Islam, Ting, & Fartaj, 2008). The result of the combined designs shows an improvement in power generation efficiency. The high starting torque of the drag in the Savonius turbine type is an advantage to starting the Darrieus machine under a hybrid system.



Figure 1.4: H rotor Darrieus wind turbine (Akwa, Vielmo, & Petry, 2012)

1.1.2.2 Savonius-Drag Based VAWT

Savonius wind turbines are drag based VAWTs that operate on the theory and principle of a paddle propelling a boat through water. It was invented by a Finnish engineer, S.J. Savonius (Akwa et al., 2012). If no slip exists between the paddle and water, the maximum speed attained will be the same as the tangential speed of the paddle. Similarly, in a drag based VAWT, the speed at the tip of the blade can seldom exceed the speed of the wind. In other words, the drag can also be described as the pressure force or the thrust on the blades created by the wind as it passes through it.

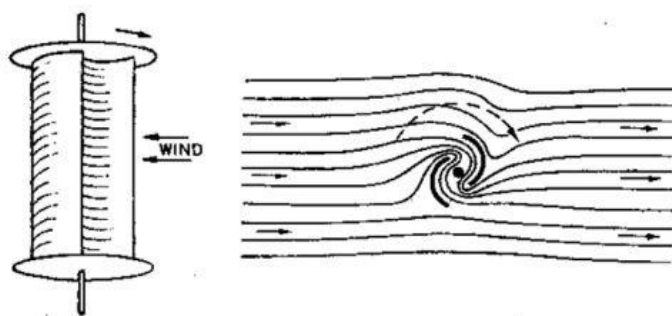


Figure 1.5: Savonius rotor (Cooper & Kennedy, 2004).

Various types of drag based VAWTs have been developed in the past, which use plates, cups, buckets, oil drums, etc. as the drag device. The Savonius rotor is an S - shaped cross section rotor (See Figure 1.5) which is predominantly drag based, but also uses a certain amount of aerodynamic lift. Drag based VAWTs have a relatively higher starting torque and less rotational speed than their lift based counterparts. Furthermore, their power output to weight ratio is also less (Akwa et al., 2012; Altan & Atilgan, 2008). Because of the low speed, this is generally considered unsuitable for producing electricity, although it is possible by selecting proper gear trains. Drag based windmills are useful for other applications such as grinding grain, pumping water and a small output of electricity. A major advantage of drag based VAWTs lies in their self-starting capacity, unlike the Darrieus lift-based vertical axis wind turbines.

1.2 AUGMENTED TURBINES

Much of the early research on modern wind turbines were concerned with the increase of the power coefficient by improving the aerodynamic design of the rotor. The research has been fruitful in that it has resulted in a wide range of rotor designs which are aerodynamically efficient, simple in form, and relatively easy to manufacture. As some designs have peak power coefficients approaching 0.5 and given the Betz's limit of 0.593, further refinements of the aerodynamic design of these rotors are not likely to be of significance in improving the cost effectiveness of the wind power system. Furthermore, a long-term operation will cause a buildup of dirt, insects and leading edge erosion, which will spoil the aerodynamic cleanliness of the airfoil sections, negating any further approach to the theoretical limit. As a result, considerable interest has been shown in increasing the power output from wind rotors by using power augmentation devices, where its main function is to increase the wind energy incident on the rotor.

The earliest use of power augmentation of wind rotors was by the ancient Persian windmills. Old vertical axis, such as the cross flow wind rotors, a section of the rotor moves against the wind, thus offering considerable resistance to rotation, hence the term, "differential drag". Effective use was therefore made of the wind-deflecting device, capable of reducing the velocity of the wind incident on the section of the rotor moving against the wind.

1.2.1 VAWT with Guide Vanes

It is a special drag based turbine with lift to boost its power output. The modular and scalable design is quiet, visually appealing and practical for residences and institutions, Figure 1.6.

The vertical axes wind turbine has some drawbacks such as possessing a low tip-speed ratio, inability to self-start and not being able to control the power output or speed by pitching the rotor blades, low coefficient of power various configurations (W. Chong et al., 2013; W. T. Chong et al., 2013; Danao, Edwards, Eboibi, & Howell, 2014). Researchers find that by using the omni-direction-guide-vanes, some of these problems can be solved (W. T. Chong et al., 2013). The omni-direction-guide-vane (ODGV) is a revolution of the power-augmentation-guide-vane (PAGV) design, as fully discussed in the references (Chong, Fazlizan, Poh, Pan, & Ping, 2012; W. T. Chong et al., 2013). It is designed to improve the performance of a wind turbine in terms of power output, rotational speed and self-starting behavior.

The first modern concepts to integrate wind energy into buildings were introduced in the 1930s and 1940s in Germany. Hermann Honnef, a German engineer, stimulated some enthusiastic discussions about wind power and proposed the construction of a gigantic multirotor wind power tower, producing as much as 60,000 kW of power (Heymann, 1998). The design from Chong et al. (2011) is also intended to integrate a

hybrid wind–solar energy system on the top of a highrise building with more emphasis on visual impact, safety, noise pollution and improvement on the starting behavior of the wind turbine. This patented design overcomes the inferior aspect of low wind speed by guiding (to obtain a better flow angle of the wind turbine blade) and increasing the speed of high altitude wind through the ODGV.

The system can be of cylindrical shape or any shape of design, depending on the building architectural profile, such as in the shape of an ellipse, etc. The wind turbine is located in the middle of the system, surrounded by the ODGV. As safety is the main public concern, this design is safe in the case of blade failure. The ODGV consists of an upper wall duct, lower wall duct and guide vanes. The ODGV is designed to be fixed or yawable with the help of a rudder.

The use of VAWT in this system has tackled the concerns of noise and vibration produced by the HAWTs. A VAWT produces much lower levels of noise and vibration compared to the HAWT because the blades do not stick out so far, thus exerting less pull (Almohammadi, Ingham, Ma, & Pourkashan, 2013). In addition, since the VAWT is surrounded by the ODGV, the noise is minimized. The large size of the wind turbine may be able to produce a higher amount of power, but when the wind speed is low, the turbine works much lower than its rated power. For this system, the ODGV will help the smaller size of the VAWT (inside the ODGV) to spin close to its rated power even if the wind speed is low.

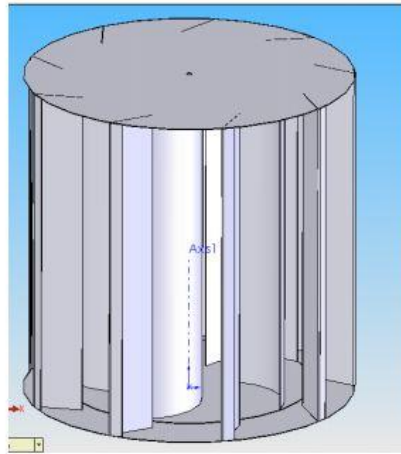


Figure 1.6: VAWT with Omni-Direction-Guide-Vane (Carlos Simao Ferreira, van Bussel, & Van Kuik, 2007b).

This study aims to improve the power output of the VAWT shrouded with optimized ODGV.

1.3 OBJECTIVES

The objectives of this study are:

- ❖ To investigate the aerodynamic behavior of the H-rotor vertical axis wind turbine using the numerical method.
- ❖ Optimization of the shape ratio of the Omni-Direction-Guide-Vane in order to improve the performance of the H-rotor VAWT.
- ❖ Optimization of the angles of the ODGV in different working conditions.
- ❖ To investigate the effect of the number of the guide vane on the performance of the H-rotor VAWT.
- ❖ Determining the performance of the ultimate model and validating it using lab test.

CHAPTER 2: LITERATURE REVIEW

This chapter is divided into two main sections: computational fluid dynamics, and augmented wind turbines. The contributions of each are discussed to show the current understanding of the different factors that affect the performance of the VAWT.

2.1 COMPUTATIONAL FLUID DYNAMICS

Research into the VAWT design was carried out as far back as the 1970's, notably at the USA Department of Energy Sandia National Laboratory. Both numerical and experimental studies were performed that set the baseline for subsequent research in the field. This ranged from the development of mathematical models to experimental work, and more recently to high fidelity computational models.

One of the objectives of numerical modelling of the VAWT is to create a mathematical representation of the problem such that extensive studies can be performed at a relatively low cost. Parametric design studies that involve multiple candidate aerofoil with several geometric configurations subjected to various operating conditions can be carried out in a virtual environment without the need for fabrication work and the setups that laboratory experiments entail.

There are generally two well-accepted types of numerical modelling used in current research work. The first is usually termed mathematical modelling, where the VAWT problem is described in mathematical expressions in which the flow field and blade loading are solved using simplistic generalizations. These are derived from fundamental aerodynamic theories. As in the case of the Blade Element Momentum models, the flow properties around the VAWT blade are assumed, and blade loading is determined by referring to the static aerofoil data from published experimental data. More accurate models employ the use of the dynamic stall models (another set of

mathematical models) that simulate the loading that is expected in a pitching and/or plunging aerofoil. The use of these effects is to complement the static aerofoil data set. The main advantage of mathematical models is the speed of the simulation. Typically, the computing costs are very low and results are available in minutes to hours. However, the downside is the lack of fidelity when it comes to near wall modelling. As such, the boundary layers on blade surfaces cannot be studied in detail. They cannot necessarily be trusted beyond conservative limits.

The second class of numerical modelling is computational fluid dynamics (CFD). In this approach, the entire flow field including the near wall can be computed using several forms of the Navier–Stokes equations. Reynolds Averaged Navier Stokes (RANS) is one such form and uses turbulence closure equations, known as turbulence models. These models are used to make the problem solvable. The fluid domain is discretized into cells or elements, and all flow variables are calculated for each. There is an intrinsic advantage to this method because there is no assumption made as to the forces acting on the blades as well as no lookup to data tables. All pressure and viscous loads are computed for each fluid cell or element. This in turn avoids the use of inappropriate data sets that could give misleading results. Due to the high fidelity of the solution, the major disadvantage to using CFD is the enormous computing costs that it demands. Solutions can be obtained from as low as tens of hours to a few weeks depending on how fine the domain is meshed. Fortunately, with the advances in computing hardware including the multi–core chips that offer parallel computing on a desktop machine and increasing storage sizes that can accommodate gigabytes of data, CFD has become a more widely used tool in VAWT research.

In our study, we focused on the simulation of the augmented VAWT using the CFD method. In the following sections, a review of the current body of literature involving CFD modelling of the VAWT is presented.

2.1.1 RANS based CFD

Simao Ferreira et al. (2007a) presented a systematic analysis of a two-bladed 2-D VAWT configuration. Validation was made by way of comparing the vertical structures generated by the CFD to the stereo particle image velocimetry (PIV) data. Results show the suitability of the PIV data for validation purposes, but also the unsuitability of one turbulence model for the highly unsteady problem. Although a good agreement was observed between the CFD and PIV flow structures, no attempt was made to compare the force data from CFD to that of experiments. As such, a definitive conclusion to the suitability of the CFD model could not be made.

Hamada et al. (2011) presented 2-D and 3-D CFD simulation results of a roof-top H-VAWT using the commercial package Fluent. Different variations of the $k-\epsilon$ turbulence model were used on a mesh that has undergone sensitivity studies in grid spacing and time step size, both of which are necessary owing to the unavailability of validation data. They have shown that power extraction in the upwind greatly influences performance in the downwind. In their 3-D model, blade tip vortices, center shaft wake and support arm wake caused significant reduction in the performance when compared to their 2-D model. A major drawback of this study was the lack of benchmarking of the presented numerical results to actual measurements. The conclusions made were only good for comparative purposes and not an authoritative statement of the overall VAWT performance.

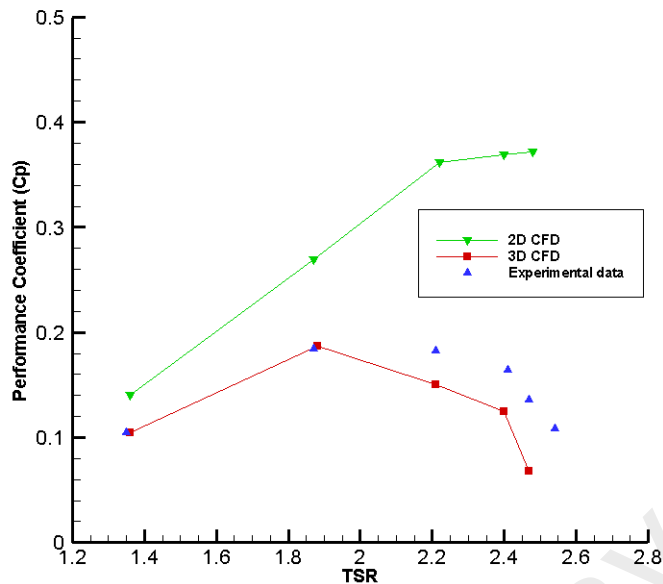


Figure 2.1: C_p curves of wind tunnel model (Howell, Qin, Edwards, & Durrani, 2010).

Similar studies were conducted by Howell et al. (2010), Edwards et al. (2007) and Raciti Castelli et al. (2011) that have shown consistent results in the observed gap between the 2-D and 3-D performance curves. Howell et al. (2010) based their model on a wind tunnel scale VAWT of 0.043m in diameter and 0.020m in height running at an average Reynolds number of about 30,000. The turbulence model selection was based solely on information provided by the CFD software documentation and educated assumptions of the expected flow features. As such, the $k-\epsilon$ RNG was chosen with wall functions enabled. Over prediction of the power coefficient (C_p) was observed for the 2-D cases, while a good agreement was seen with the 3-D cases versus the experiment results (Figure 2.1).

McLaren et al. (2012) performed 2-D CFD simulations for a high solidity, small scale H-type VAWT. The three-bladed rotor was operating at an average Reynolds number of 360,000 over a wide range of blade speed ratios. Commercial code ANSYS CFX was used for the simulations and model validation was made by comparing lift coefficients of static NACA0012 aerofoil runs to experimental data by Sheldahl and Klimas (1981). The hybrid $k-\omega$ shear stress transport (SST) was considered the

turbulence model that was most appropriate to carry out the dynamic modelling that the problem requires. 2-D VAWT simulations were conducted over blade speed ratios covering the full operating conditions of a typical VAWT from the dynamic stall region, to the power-producing region, then up to the viscous effects region. Results are consistent to previous studies where the actual 3-D experimental data are significantly lower than the 2-D CFD predicted performance (Figure 2.2). A correction factor was applied to the 2-D CFD results to account for the major 3-D components of the problem that are not modelled in the 2-D simulations.

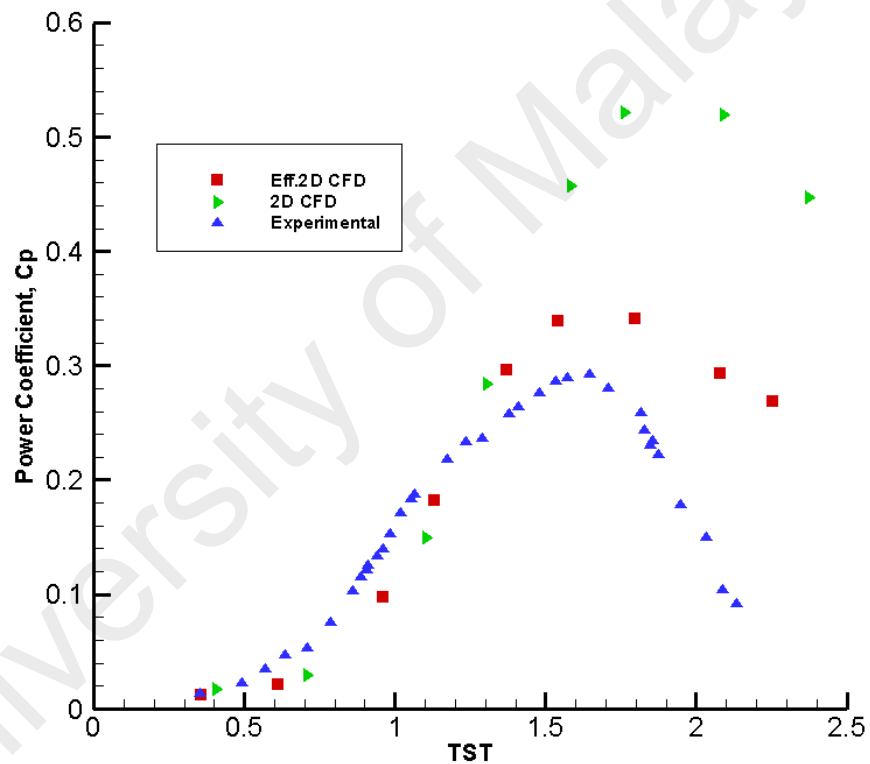


Figure 2.2: VAWT C_p for 2D, effective 2D, and experiments (K. McLaren et al., 2012).

Edwards et al. (2012) provided the necessary resolution to performing a validation of the CFD model using both performance data from a novel experimental method and from PIV visualizations. The validation study was twofold in a sense that firstly, the selection of an appropriate turbulence model was narrowed down by means of a pitching aerofoil study using experimental data from Lee and Gerontakos (2004).

Secondly, the CFD model of the VAWT was tested using experimentally generated data. For the turbulence model study, it was determined that the $k-\omega$ SST turbulence model was the best candidate for the highly dynamic and unsteady problem of a pitching aerofoil characteristic of which that is not too different from a VAWT blade.

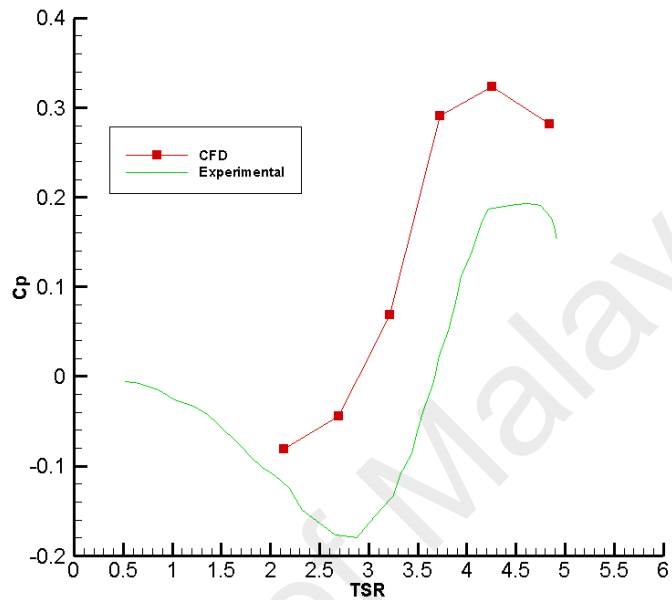


Figure 2.3: Spin down and CFD C_p results(J. M. Edwards et al., 2012).

Similar to observations by previous researchers, they have seen that 2-D CFD simulations show an over prediction in blade performance when compared to actual 3-D experiment measurements (Figure 2.3).

Li et al. (2016) studied aerodynamic forces and inertial contributions to rotor blade deformation on VAWT using CFD. 3-D CFD carried on the two-bladed VAWT. The turbulence model was selected as $k-\varepsilon$ and $k-\omega$ SST. From comparing the results of the wind tunnel experiments and numerical analysis, it was found that the fluid force decreased with the increase of span wise positions, excluding the position of support structure. Furthermore, according to the result from the six-component balance, the waveforms of the power coefficient C_p have similar characteristics and show smaller values than the CFD calculations.

2.1.2 Dynamic Stall Phenomenon

One of the major stumbling blocks of mathematical modelling of the VAWT is the dynamic stall phenomenon usually expected in many operating conditions. When an aerofoil is under oscillating motion in a moving fluid, stalling can be considerably delayed beyond the static stall angle. A consequence of this is that static aerofoil data is no longer suitable because the forces on the blade exceed the static stall values and large hysteresis are exhibited with respect to the instantaneous angle of attack (Figure 2.4). This is more prominent in oscillations with amplitudes in the order of the static stall angle (McCroskey, 1981). Without any doubt, this poses similar or an even greater challenge to CFD modelling because the absence of a reference case that is the static aerofoil to which CFD can benchmark from adds to the uncertainty of the solution.

Dynamic stall is characterized by the shedding of a vortex over the suction surface of an aerofoil under pitching motion in a stream of fluid. If the frequency, amplitude and maximum incidence are sufficiently high, an organized and clearly defined shedding of vortices is observed. Dynamic stall is broadly characterized by the following sequence of events:

STAGE 1: at incidence pass the static stall angle, flow reversal develops near the trailing edge of the aerofoil and moves forward to the leading edge.

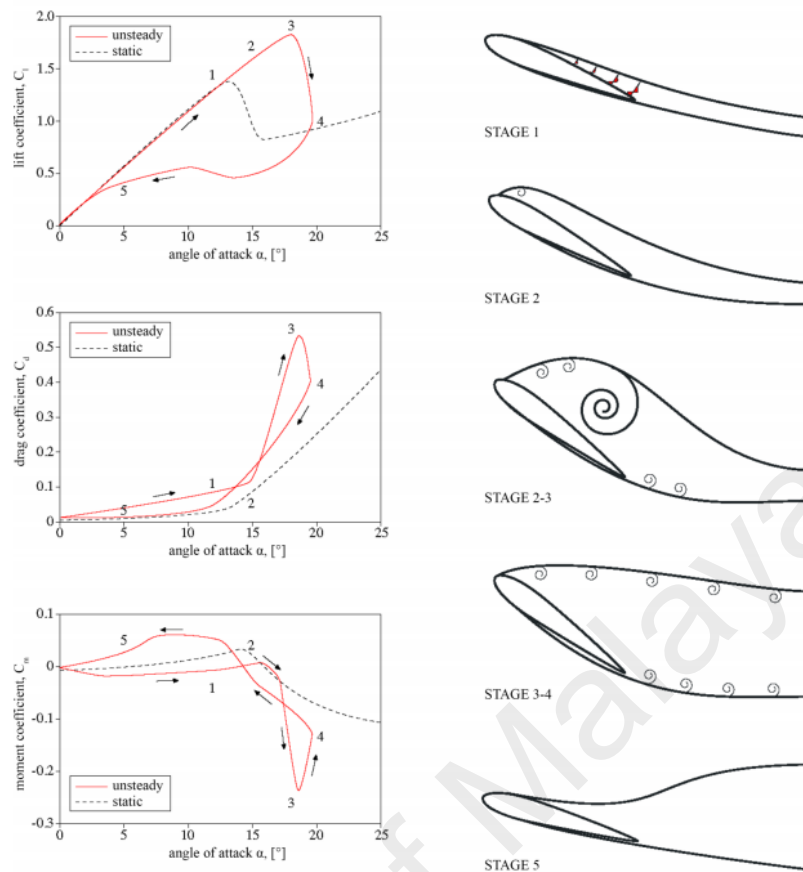


Figure 2.4: An illustration of the dynamic stall process (adapted from(Simon Charles McIntosh, 2009)).

STAGE 2: further increase in incidence causes the separation point to move towards the leading edge. The boundary layer starts to separate and the center of pressure moves downstream causing the nose of the blade to pitch down. The boundary layer separation also induces an increase in drag. Lift continues to increase way beyond maximum static values. The free–shear layer that is formed in the leading edge starts to roll up forming the dynamic stall vortex.

STAGE 3: the dynamic stall vortex continues to grow due to further input of vorticity from the leading edge separation, causing the lift to continue to rise and reach maximum values.

STAGE 4: as the dynamic stall vortex leaves the blade surface, there is a sharp drop in the lift and full separation takes place. Depending on the rate of pitching and subsequent growth of the leading edge, vortices may occur alongside the roll up of

trailing edge vortex structures forming a band of alternately shed vortex blobs behind the blade.

STAGE 5: decreasing incidence eventually causes the flow to reattach to the blade starting from the leading edge and moving downstream towards the trailing edge. Similar delays are observed in the reattachment process causing the lift to undershoot static values before full recovery of the flow closing the hysteresis loops of the force and moment coefficients.

Qin et al.(2011) discussed the effects of dynamic stall with respect to force coefficient variation against azimuthal position and noted that the lift generated by the VAWT blade exceeds static stall values in the upwind pass. There is also a significant difference seen in the predicted lift between the upwind and downwind pass, which proves that the VAWT blade cannot be directly compared to a pitching aerofoil. However, they have not shown a systematic method of selecting the appropriate turbulence model, but instead relied on available literature to assess the suitability of a turbulence model for problems involving large flow separations that is present in the VAWT problem. There was also the lack of validation data to which the CFD model can be compared.

To address the issue of non-availability of VAWT validation data, some work has been conducted with pitching aerofoils that exhibit very similar dynamic stall events with VAWTs. The close likeness of VAWT blades and pitching aerofoils in as far as dynamic stall is concerned make pitching aerofoils a viable validation candidate. Martinat et al. (2008) studied a pitching NACA0012 aerofoil at 10^5 and 10^6 Reynolds numbers and have shown that standard turbulence models have a significant dissipative character that attenuates the instabilities and vortex structures related to dynamic stall. On the other hand, organized eddy simulation (OES) and the SST model have shown a

better prediction of a dynamic stall, especially at high Reynolds numbers. However, they seem to show to have a need of transition modelling at low Reynolds numbers.

Wang et al. (2010) presented a numerical investigation of turbulence modelling of dynamic stall of low Reynolds number oscillating aerofoils. They observed that $k-\omega$ SST based DES is more superior in predicting the dynamic stall process over RANS models $k-\varepsilon$ RNG, $k-\omega$ standard, $k-\omega$ SST, and transition SST. Good agreement was seen with the transition SST model in the pitching up stroke where the predicted maximum lift coefficient is very close to experiments. Where the transition SST fails, the DES is seen to prevail. Better prediction in lift coefficient was seen in the DES model with less undershoot in the pitching down stroke. Although a detailed comparison with force predictions was performed, the lack of flow validation through comparison of vorticity fields is seen as the downfall of their study. Their extensive presentation of CFD visualizations is not complemented by comparison to an actual experimental visualization, such as smoke streaks and PIV that were available in the case studies (Lee & Gerontakos, 2004; Wernert, Geissler, Raffel, & Kompenhans, 1996) that they have analyzed.

The popularity of some turbulence models has influenced the direction of numerous research works on VAWT modelling. For its robust qualities and proven record of excellent predictions in a variety of engineering problems, the standard $k-\varepsilon$ model and its variants have become a popular choice for researchers. Carlos Simao Ferreira et al. (2007a) investigated the use of the standard $k-\varepsilon$ model on a VAWT running at $TSR=2$. It was observed that the fully turbulent model suppressed the development of the leading edge separation bubble seen in their PIV tests and was predicted by a fully laminar model (Figure 2.5). The predicted normal and tangential forces on the blade were also seen to be opposite in trend versus the laminar model.

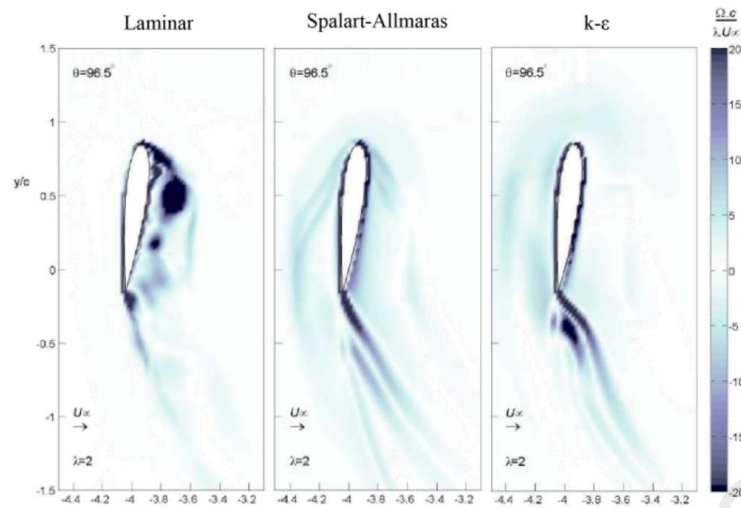


Figure 2.5: Vorticity plots of turbulence model study(Carlos Simao Ferreira et al., 2007a).

Wang et al.(2016) presented a numerical study on the aerodynamic performance of a vertical axis wind turbine with adaptive blades. Simulation was conducted by the United Computational Fluid Dynamics code. Firstly, analysis and comparison of the performance of undeformed and deformed blades for the rotors having different blades were conducted. Then, the power characteristics of each simulated turbine were summarized and a universal tendency was found. Secondly, investigation on the effect of blade number and solidity on the power performance of the Darrieus vertical axis wind turbine with deformable and undeformable blades was carried out. The results indicated that the maximum percentage increase in power coefficient that the low solidity turbine with three deformable blades can achieve was about 14.56%.

Hamada et al. (2008) and Howell et al. (2010) used the three available variants of the $k-\epsilon$ model in a commercial CFD package Fluent in their simulations and have shown that the $k-\epsilon$ standard model deviates from $k-\epsilon$ RNG and $k-\epsilon$ Realizable in the torque predictions. They argue that for problems involving strong streamline curvatures, vortices and rotation, the standard variant is less superior to the RNG and Realizable models. Moreover, the Realizable variant is prone to produce non – physical turbulent viscosities when the domains include stationary and rotating fluid zones. Two-

dimensional and three-dimensional CFD models were studied and it was seen that the RNG variant consistently over-predicted the C_p for the 2-D model while under-predicting C_p in the 3D case. Although a reasonable agreement was seen between the 3-D model and experiments, the CFD predictions tended to diverge from the measurements as the TSR increased. The only non-conforming result was at the highest test wind speed and highest TSR where the predicted C_p was above the measure C_p and within the assumed experimental error.

Beri et al. (2011) and Untaroiu et al. (2011) used the $k-\epsilon$ model to examine self-starting capabilities of the VAWTs. Beri et al. (2011) concluded that cambered aerofoils have the potential for self-starting but unfortunately, they reduce the peak efficiency. A static aerofoil study was presented as validation of their CFD model and it was observed that the RNG model properly predicted the lift forces on the aerofoil at a low incidence. However, it also showed delayed stalling when compared to the experimental data. They contended that the model was suitable for VAWT simulations because the incidence angle of the flow relative to the VAWT blades is said to be within the low range. This is only true if the operating conditions were such that no observed stalling of the blades is expected i.e. high TSR beyond the peak performance point. A low TSR usually pushes the performance of the VAWT within the dynamic stall region where incidence angles exceed static stall values of up to 1.5 times. Delayed stalling causes inaccuracies in performance prediction because it induces a longer positive torque production of the blades, resulting a higher power production.

Untaroiu et al. (2011) carried out 2-D and 3-D simulations of a wind tunnel scale VAWT using the standard $k-\epsilon$ model. They studied the self-starting potential of a high solidity rotor and found consistent results to what has been reported by Howell et al. (2010) regarding the over-prediction of 2D models and the under-prediction of 3D models. During the rotor start-up, simulations show a very steep ramp up of the rotor's

angular speed versus experiments. There is also the absence of the intermediate velocity plateau seen in experiments before a full operating speed is attained. This was claimed to be an effect of poor near-wall modelling of the $k-\epsilon$ resulting to a lower viscous drag induced and may be avoided by using more superior turbulence models for wall bounded flow problems such as $k-\omega$ and its variants.

Raciti Castelli et al. (2010) conducted 2-D and 3-D, single and three bladed VAWT simulations in an attempt to develop a performance prediction methodology based on the CFD. A modelling strategy was presented and validated using a wind tunnel measured performance of a full-scale low solidity VAWT. To assess the suitability of a turbulence model, the wall y^+ parameter was inspected. It was observed that for models with wall functions enabled ($y^+ > 30$), the $k-\omega$ model was appropriate, whereas models with enhanced wall treatment ($y^+ \approx 1$) necessitated the use of the $k-\epsilon$ Realizable model. Their basis for this conclusion was a statistical study of the y^+ parameter and the suitability of the turbulence model was dependent on the distance of the mean y^+ from the recommended values and degree of the spread of the wall y^+ about the mean. A comparison between the 2D CFD predicted C_p and experimental data has shown that the 2D results over-predict the C_p but replicate the general curve. There was no inspection and assessment of the flow field as to the model's accuracy in predicting stall and reattachment, which is critical in explaining performance trends.

The inability of the $k-\epsilon$ turbulence model to properly compute the flows of many engineering problems with strong adverse pressure gradients and separation led to the development of alternative turbulence models that can address the issue. The behaviour of turbulent boundary layers up to the separation was a challenge to the family of $k-\epsilon$ models. This led to researchers turning to another well-established turbulence model known to be more superior in near wall modelling, the $k-\omega$ model. This does not come without its own drawbacks. The $k-\omega$ model, shown to be

successful for flows with moderate adverse pressure gradients, fails to predict flows with pressure induced separation and shows a strong sensitivity to the values of ω in the free stream (Menter, Kuntz, & Langtry, 2003).

Despite this limitation, researchers were still motivated to use this alternative turbulence model in VAWT simulations.

Amet et al. (2009) conducted 2D simulations at two extreme tip speed ratios, $TSR=2$ and $TSR=7$. Lift (Figure 2.6) and drag coefficients around a full rotation were compared to experiments performed by Laneville and Vittecoq (1986). Although the general shape and trend of the curves were similar, significant differences were observed between simulations and experiments. There is a clear upward shift of the CFD-computed lift coefficients but maximum values are very close to experimental values. A non-zero lift is seen in the simulation at zero incidence, whereas experiments show negligible lift. However, they question the validity and accuracy of the experimental data instead of discussing the possible reasons for the differences.

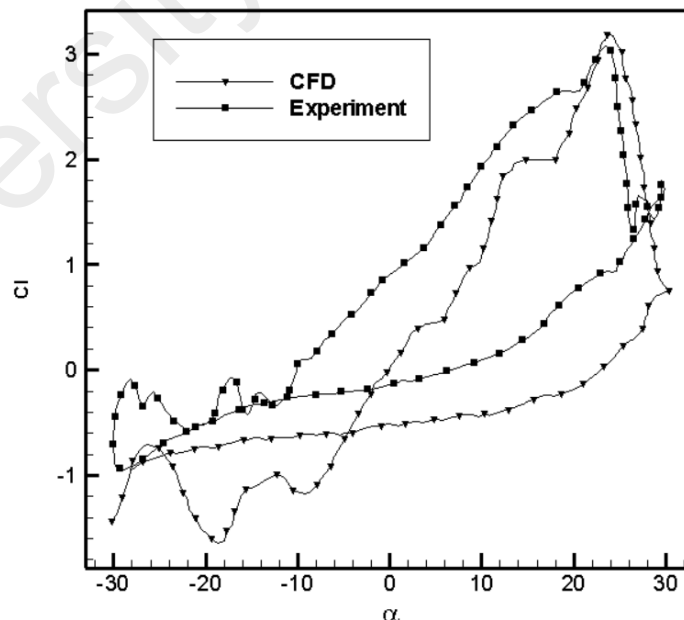


Figure 2.6: Lift hysteresis loops for a VAWT blade(Amet et al., 2009).

Nobile et al. (2011) compared the $k-\omega$ model against the $k-\varepsilon$ model and a new variant of the $k-\omega$ model, the $k-\omega$ SST. The vorticity field predictions of the $k-\omega$ model were put side by side with the PIV data from (CJ Simao Ferreira, Bijl, Van Bussel, & Van Kuik, 2007; CJ Simão Ferreira, Van Zuijlen, Bijl, Van Bussel, & Van Kuik, 2010) and a key difference was observed. While the separation point and depth of stall prediction was better than the $k-\varepsilon$ model, the evolution of the dynamic stall vortex was still suppressed and significant dissipation of the eddies was seen. The absence of the trailing edge vortex expected from the dynamic stall process is also noted.

The hybrid turbulence model $k-\omega$ SST has seen popular use as a step forward in VAWT modelling because it combines the near wall capabilities of the $k-\omega$ model and the free stream stability of the $k-\varepsilon$ model. Some researches that have been carried out on VAWT simulations also included applications in water turbines. Dai et al. (2009) and Consul et al. (2009) conducted numerical studies on tidal turbines of the Darrieus type. Dai et al. (2009) performed a study on the effects of scale on a straight-bladed turbine in an effort to predict the performance of large-scale tidal turbines. The obtained results are in good agreement with expected values and trends. Hydrodynamic performance and structural load predictions were considered acceptable despite the lack of proper validation of the CFD model. Instead of a thorough validation, a sensitivity analysis was carried out on the time step size. A comparison of the turbine performance was presented for one operating condition and showed that the $k-\omega$ SST only slightly over predicted C_p in spite of the fact that the simulation is 2-D. They continue to conclude that the model is sufficiently validated and is further used on a 1MW scale model.

Consul et al. (2009) performed numerical investigations on the effects of solidity on a tidal turbine. Validation of the 2-D model by way of static aerofoil study on lift and drag predictions was done on published experimental data by Sheldahl and

Klimas(1981) of a NACA0015 profile. The one-equation Spalart-Allmaras (SA) turbulence model was compared to the two-equation $k-\omega$ SST model, and minor differences in lift and drag were seen between the two. Both deviate from experimental results in terms of the predicted stalling angle and maximum lift before stalling. The average error of the numerically computed drag of the SA model is seen to be greater than the $k-\omega$ SST model, while the errors of a computed lift is very similar

McLaren et al. (2011) tested the predictive capabilities of the $k-\omega$ SST model by conducting static aerofoil tests on a NACA0015 blade at the Reynolds number of 360,000. Similar to the reference case used by Consul et al. (2009) earlier, lift and drag predictions of three turbulence models were compared against experimental data. A better trend was seen with the $k-\omega$ SST model results versus the $k-\omega$ standard model and the $k-\epsilon$ standard model. The latter two models over predict the maximum lift and stalling angle, while very close outcomes are seen with the $k-\omega$ SST model.

A point of contention can be made with a lot of the work presented above when it comes to the efforts in the validation of the CFD models. The reference point to which the models are compared to do not represent the unsteady flow behavior that is seen in VAWT dynamics. The rigorous prerequisites of modelling a pitching and plunging aerofoil in constantly changing relative velocities and incidences are satisfied neither by a static aerofoil study, nor by simple numerical sensitivity analyses. The wide range of possible flow conditions that a VAWT blade encounters within one operating condition warrants a validation method that can live up to the demands of a highly transient problem. Modelling the stalling and reattachment of flow on a VAWT blade directly affects the predicted performance of the wind machine and as such, is critical to the validity of the numerical model being used. A more thorough validation that covers both, force prediction as well as the flow prediction is necessary to address this need.

Edwards et al. (2012) and Danao et al. (2012) addressed the challenge of proper validation of the CFD model by conducting a systematic one-to-one evaluation of force and flow predictions to both published pitching aerofoil data as well as their own generated VAWT experimental data. The process of narrowing down the list of turbulence model candidates involved the investigation of a pitching aerofoil study conducted by Lee and Gerontakos (2004). What Edwards et al. (2012) found out is that the most appropriate turbulence model that correctly predicts both, the forces (Figure 2.7) and the flows past an oscillating aerofoil is the $k-\omega$ SST. They have shown that the $k-\omega$ SST is the closest when it comes to pitching aerofoil simulations.

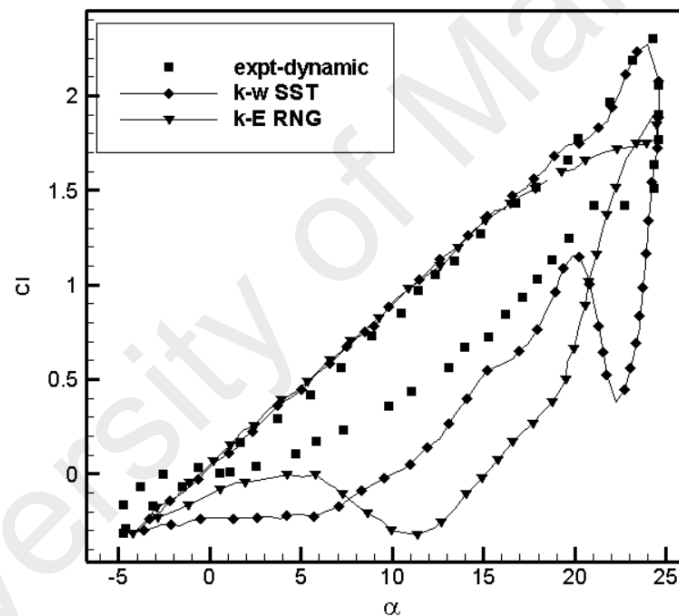


Figure 2.7: Lift coefficient predictions of different turbulence models (J. M. Edwards et al., 2012).

Further investigations by Danao and Howell (2012) improved the simulation accuracy by considering the Transition SST turbulence model which, previously examined by Wang et al. (2010). It was observed that the Transition SST resolves the delayed stalling at $TSR=2$ that is seen in the fully turbulent $k-\omega$ SST and better prediction in the blade force is also achieved resulting to a closer prediction of C_p to experiments (Figure 2.8). The use of the Transition SST model also predicts the stalling

of the blades at $TSR = 4$, a factor in the significant reduction of C_p at a high TSR . There is a perceived convergence of performance predictions between the transitional model and the fully turbulent model at $TSR > 5$. It seems that the Transition SST is behaving more like its fully turbulent cousin, causing similar values in rotor efficiency.

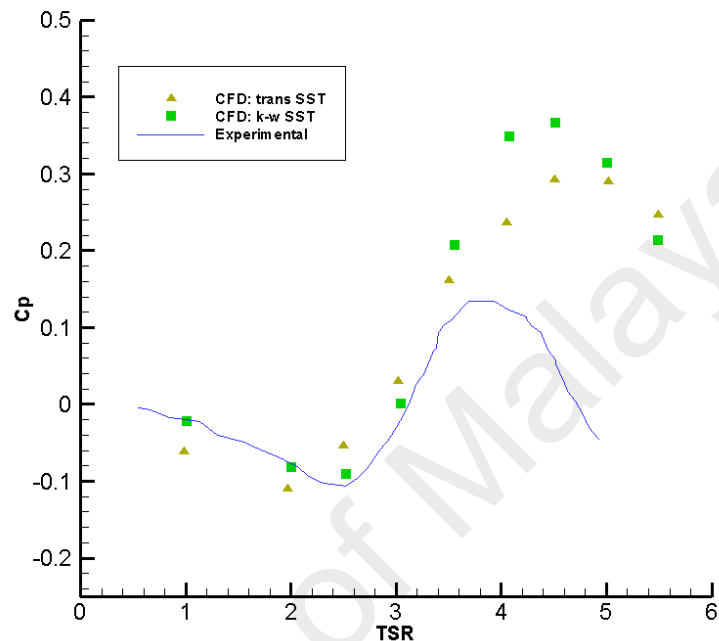


Figure 2.8: Power coefficient plot of wind tunnel scale VAWT (Danao & Howell, 2012).

2.2 AUGMENTED WIND TURBINES

One of the main goals of wind turbine development is increasing the power output of the turbines. According to the equation (2.12) there are two parameters that affect the value of the power, swept area of blades and the wind speed. Therefore, the power output can be increased by increasing one of the two parameters. One of the methods to increase the effective wind velocity is to use a duct around the rotor. That design is sometimes referred to as a Diffuser-Augmented Wind Turbine (DAWT). Figure 2.9 illustrates a schematic of this design applied to a HAWT, and the change in the stream tube is compared to the conventional (free-stream) wind turbine.

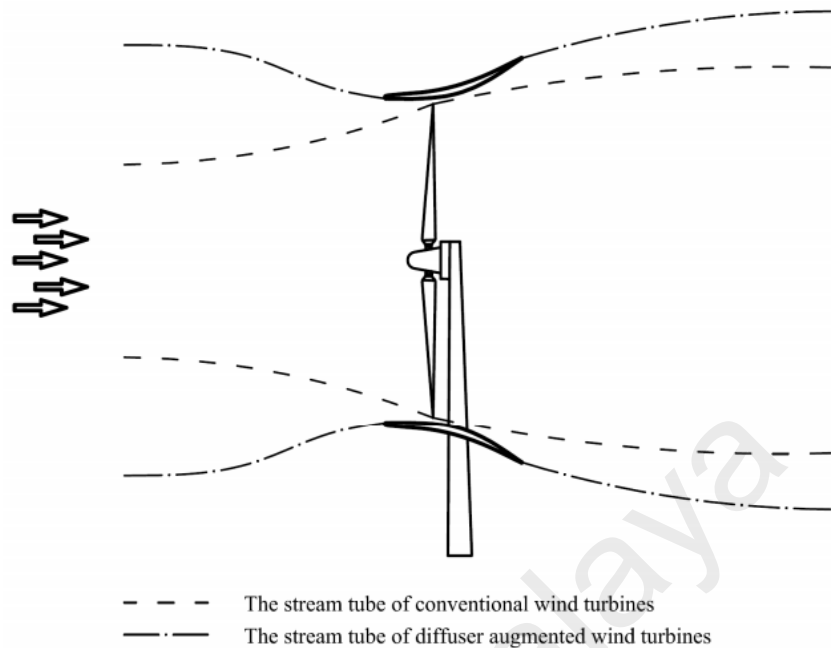


Figure 2.9: Stream tube comparison between a conventional wind turbine and a DAWT.

The duct around the rotor increases the flow rate of the air through the area swept by the rotor, thus increasing the wind velocity at the rotor. Therefore, the effective range of the wind speed for generating the desired power is higher than conventional design. DAWTs also have a higher power per unit of rotor area than the turbines without a diffuser. Another advantage of using a diffuser around the blades is that the theoretical maximum power of a ducted wind turbine is not limited by the Betz limit, and is related to the pressure difference and the flow rate in the duct (Kirke, 2005). By analytical simulation, Riegler (1983) demonstrated that the maximum power coefficient of the diffuser shape ducted wind turbine is 3.3 times higher than the Betz limit for a free-stream turbine.

Several studies regarding the diffuser design for the HAWTs have been reported in previous literatures. One of the early investigations for the diffuser-augmented wind turbines was done by Igra (1977). In the experimental study, the author used a NACA 4412 airfoil as a diffuser around a HAWT to present the power improvement by a factor

of two. In his later work (Igra, 1981), Igra investigated different NACA airfoils for the diffuser-profile and also different designs by using an airfoil-ring behind the diffuser as well as at the entrance.

Another diffuser design was done by Abe et al. (2005). The authors suggested a diffuser with a flange at the end of the diffuser to increase the power output of a HAWT. In that work, the authors performed a numerical and experimental investigation to show the effect of the flange downstream. They also investigated the effect of the entrance of the diffuser by using a diffuser with wider entrance section.

The flanged diffuser was used for a further experimental study of Ohya et al. (2008) to design a commercial diffuser-augmented turbine. Furthermore, they studied the flange at the end of the diffuser for different diffuser lengths to design more compact diffusers.

Although the majority of the diffuser developments were done for HAWTs, few works focused on the diffuser design for VAWT applications. In particular, Takahashi et al. (2006), studied the performance of a Darrieus vertical axis wind turbine with a flanged diffuser. The authors compared the performance of the bare rotor with two different flanged diffusers. Furthermore, a numerical and experimental investigation were done by Roa et al. (2010) for a cross flow water turbine with and without a diffuser. The authors used a Darrieus-shaped rotor for tidal applications with two different airfoil profiles for the diffuser.

A lotus-shaped micro-wind turbine was also developed by Wang and Zhanas (2015) for a decoration for urban and rural areas. Barchans dune was used as a model to design the guide blades of the wind turbine. The performance of each section of the semi-circular blades was also analyzed. Findings suggest that the power coefficients for 151, 201, or 251 slopes of the rotor are roughly identical at the same tip speed ratio, and their values are relatively larger than those of the other rotors without the guide blades

or with a 0° or 30° slope. Furthermore, their maximum values are approximately 120% of the rotor with null slope or without guide blades. The performance of the wind rotor is minimally dependent on the skew angle of the barchans dune guide blade within the range of $\alpha=15-25$.

Chong et al. (2013) designed a novel Omni-Direction-Guide-Vane (ODGV) that surrounded a vertical axis wind turbine (VAWT) to improve the wind turbine performance. Wind tunnel testing was performed to evaluate the performance of a 5-bladed (Wortmann FX63-137 airfoil) H-rotor wind turbine, with and without the integration of the ODGV. The test was conducted using a scaled model turbine, which was constructed to simulate the VAWT enclosed by the ODGV placed on a building. The VAWT shows an improvement on its self-starting behavior where the cut-in speed was reduced with the integration of the ODGV. Since the VAWT is able to self-start at a lower wind speed, the working hour of the wind turbine would increase.

The working concept of the ODGV is to minimize the negative torque zone of a lift-type VAWT and to reduce turbulence and rotational speed fluctuation. It was verified by re-simulating the torque coefficient data of a single bladed (NACA 0015 airfoil) VAWT published by the Sandia National Laboratories (Mann, 1998). From the simulation results, with the presence of the ODGV, it was shown that the torque output of the NACA 0015 airfoil, the single bladed VAWT was increased by 58% and 39% at $TSR = 2.5$, and $TSR = 5.1$ respectively. The negative torque zone was minimized thus; the positive torque that provides a higher power can be obtained.

Pope et al.(2010) investigated the effect of the stator vane on the vertical axis wind turbine. 3-D and 2-D CFD simulations validated with experimental tests. Two different fluid flow formulations were investigated, which are the multiple reference frame and moving grid transient formulation. A Spalart-Allmaras model was used for the

turbulence effect on the MRF prediction. Both numerical methods show the same trend for the change of fluid dynamic in the VAWT geometry.

Experimental test on the straight bladed VAWT with directed guide vanes row was investigated by Takao et al.(2007). Test VAWT has NACA 0015 as a profile of the turbine with a radius of 0.3m. The guide vane row has three arc plates that rotate around the rotor. Using the vanes improve the C_p approximately 1.5 times higher than the original turbine which has no guide vane. A weakness of this study was that there was no CFD and numerical works.

Kosasih et al. (2012) studied the performance of the bare and diffuser shrouded micro turbine under axial and non-axial inflow conditions by experimental work. Similar to Takao et al (2007), there was not any numerical simulation in this study. The authors used the horizontal axis wind turbine with a different diffuser angle and nozzles to find the optimum shape of the diffuser. They concluded that the C_p of the micro wind turbine increased by approximately 56% with the addition of a conical diffuser.

The Aerodynamic Analysis of a Vertical Axis Wind Turbine in a Diffuser was illustrated by Geurts et al.(2010). The VAWT is shrouded with a unique shape of a diffuser simulated in a CFD.

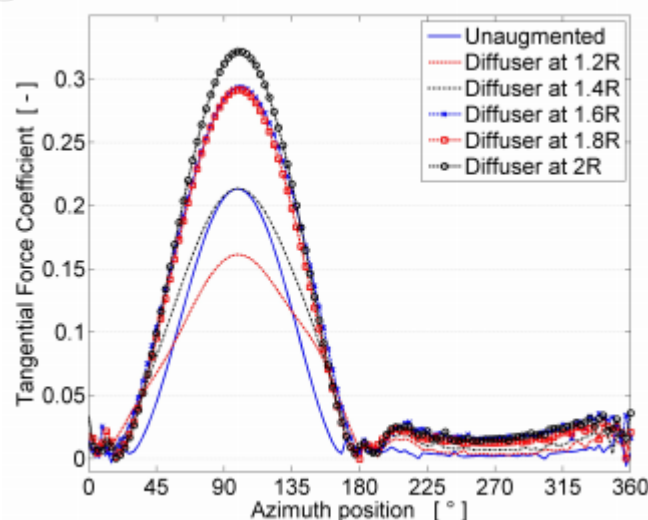


Figure 2.10: Torque coefficient contribution of single blade for different diffuser nozzle

Results show that using a diffuser in comparison of 2R from the VAWT has the highest effect of tangential force coefficient compared to the unaugmented turbine (see Figure 2.10). However, this study was not validating the CFD simulation against any experimental data. Therefore, the simulation accuracy was not reliable.

Chong et al. (2016) investigated an application of an adaptive neuro-fuzzy methodology for performance investigation of a power-augmented vertical axis wind turbine. The aim of the study was to determine the accuracy of a soft computing technique on the rotational speed estimation of a vertical axis wind turbine with PAGV (power-augmentation-guide-vane) based upon a series of measurements. An ANFIS (adaptive neuro-fuzzy inference system) was used to predict the wind turbine's rotational speed. Experimental tests were done to verify the accuracy of the ANFIS model. However, the lack of the CFD simulation was a major drawback of this study.

2.3 SUMMARY

In this chapter background of the VAWT simulation using the CFD method was discussed. It was found that there is not proper CFD investigation on the augmented wind turbine in previous researches. In most cases, researchers are focused on the bare VAWT. Research gap can be monitored in the field of the augmented wind turbine.

It was observed that the accuracy of the CFD simulation are highly depends on the mesh spacing and turbulence model, There have been significant advances in the study of VAWTs using CFD, all pointing to the ability of the $k-\omega$ SST turbulence model in properly modelling the unsteady aerodynamics that accompanies the operation of VAWTs. Investigations using the $k-\omega$ SST turbulence model are in its infancy. However, promising results have been shown lately that improve on the excellent

agreement of its fully turbulent cousin when it comes to force and flow predictions of dynamic stalling and its effects that is present in the VAWT's drawbacks.

University of Malaya

CHAPTER3: METHODOLOGY

In this chapter, the aerodynamics theory and performance characteristics of the VAWT, respond surface methodology and methodology of the experiment and numerical methods used to acquire performance data and relevant flow visualizations are discussed. Initially, the performance characteristic and surface respond methodology are discussed then experiment facility is described in sufficient detail. In the next step, the development of the numerical model used in all CFD simulations in this thesis is presented in this chapter. A detailed description of the numerical domain is initially presented which outlines the general features of the model such as multiple meshes, boundary extents and conditions, and inlet and outlet conditions. Next, the different parametric studies are presented to provide in depth understanding as to why specific features in the model are used, such as blade node density, domain size, time step size, and turbulence model. Finally, the numerical model is compared to experimental data to assess its capability in predicting performance data such as the power and torque coefficient.

3.1 AERODYNAMICS THEORY AND PERFORMANCE CHARACTERISTICS

The aerodynamic analysis of VAWTs is complicated due to their orientation in the oncoming wind. The VAWTs have a rotational axis perpendicular to the oncoming airflow. This accounts for the aerodynamics that is more complicated than a conventional HAWT. However, the configuration has an independence of wind direction. The main shortfalls are the high local angles of attack and the wake coming from the blades in the upwind part and axis. This disadvantage is more pronounced with the Savonius (pure drag) VAWTs, when compared to the Darrieus VAWTs.

Understanding the aerodynamics of the VAWT will give important insight in improving the performance and designing this turbine for a better and more efficient harnessing of the wind energy.

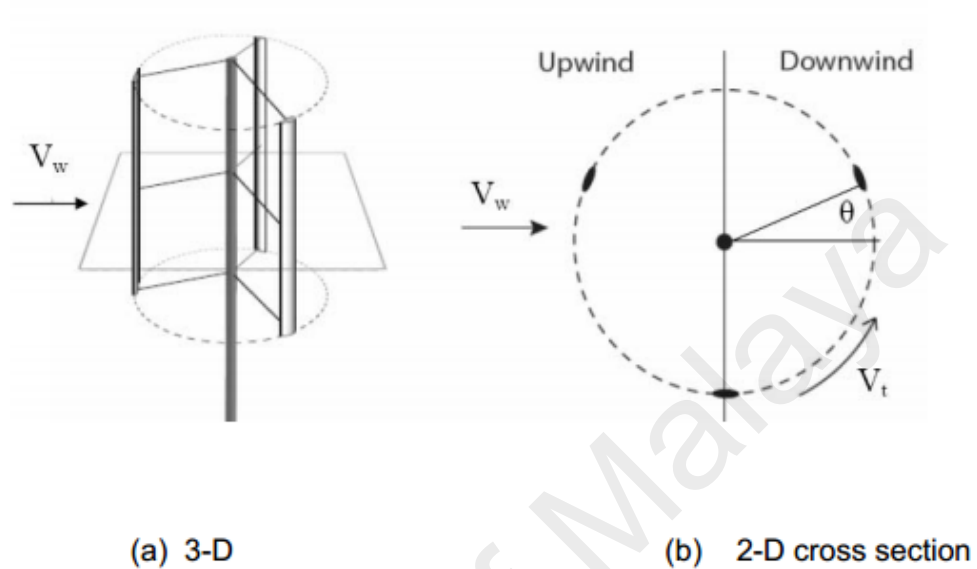


Figure 3.1: VAWT model.(Templin, 1974).

Figure 3.1 shows a typical VAWT model in both, three and two-dimensional orientations.

3.1.1 Lift Force

The lift force, L , is one of the major force components exerted on an airfoil section inserted in a moving fluid and performs normally to the fluid flow direction. This force is a consequence of the uneven pressure distribution between the upper and lower blade surfaces (see Figure 3.1), and this can be expressed as follows:

$$L = 0.5C_l\rho U^2 A \quad (3.1)$$

Where ρ is the air density, C_l is the lift coefficient and A is the blade airfoil area.

3.1.2 Drag Force

The drag force, D acts in the direction of the fluid flow. Drag occurs due to the viscous friction forces on the airfoil surfaces and the unequal pressure on surfaces of the airfoil. Drag is a function of the relative wind velocity at the rotor surface, which is the difference between the wind speed and the speed of the surface this can be expressed as:

$$D = 0.5C_d\rho(U - \omega R_{rotor})^2 A \quad (3.2)$$

Where ωR_{rotor} is the speed of the surface at the blade, C_d is the drag coefficient, and U is the wind speed. The lift and drag coefficient values are usually obtained experimentally and correlated against the Reynolds number.

A section of a blade at radius r is illustrated in Figure 3.2, with the associated velocities, forces and angles shown. The relative wind vector at radius r is denoted by V_{rel} , and the angle of the relative wind speed to the plane of rotation is by ϕ . The resultant lift and drag forces are represented by L and D , which are directly perpendicular and parallel to the relative wind.

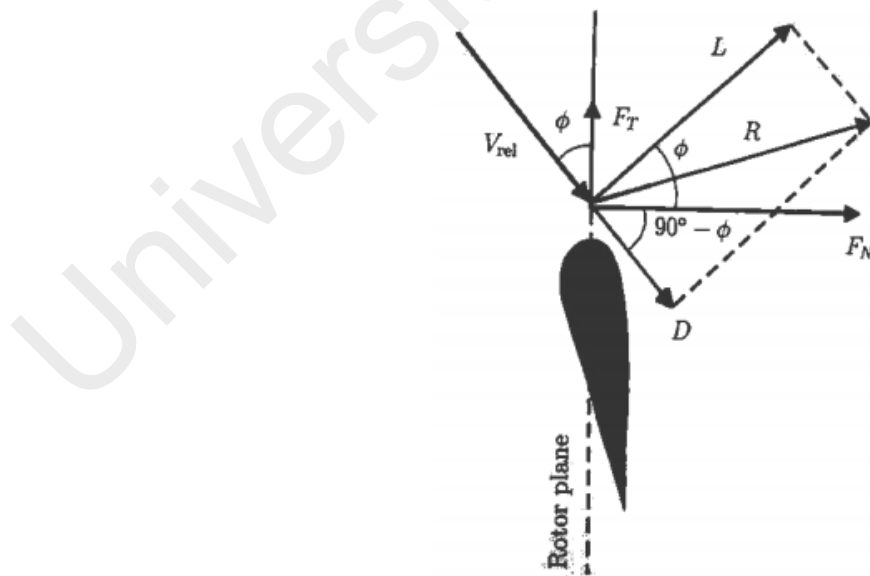


Figure 3.2: Local forces on a blade.

A careful choice of the rotor blades' geometry and shape modification is crucial for maximum efficiency. Wind turbines have typically used airfoils based on the wings of airplanes, although new airfoils are specially designed for use on rotors. Airfoils use the concept of lift, as opposed to drag, to harness the wind's energy. Blades that operate with lift (forces perpendicular to the direction of flow) are more efficient than a drag machine. Certain curved and rounded shapes have resulted to be most efficient in employing lift. Improvements of the lift coefficient for the VAWT turbine depend on geometry to enhance the performance.

When the edge of the airfoil is angled slightly out of the direction of the wind, the air moves more quickly on the downstream (upper) side creating a low pressure. On the upstream side of the airfoil, the pressure is high. Essentially, this pressure differential lifts the airfoil upwards. (See Figure 3.3). In the case of a wind turbine, the lift creates a turning effect. Thus, an operating condition with a low blade angle of attack, α , favors lift force.

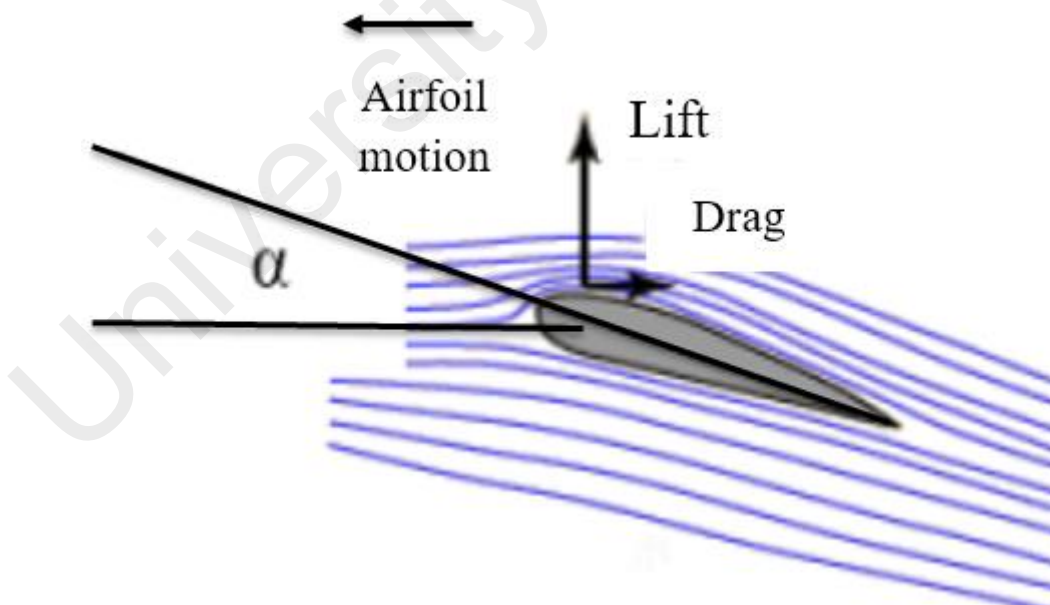


Figure 3.3: Airflow around an airfoil.

Bernoulli's principle indicates how a faster flow implies lower pressure on the airfoil:

$$P + \frac{1}{2} \rho v = \text{const.} \quad (3.3)$$

The first term in equation (3.3) is the static pressure, whereas the second term is the dynamic pressure. An increase in velocity leads to a corresponding decrease in the static pressure to maintain a constant, and vice versa. The equation can be understood through a conservation of energy as pressure work is converted to form kinetic energy in the flow field.

3.1.3 Reynolds number

The Reynolds number, Re is the ratio of the inertia forces to the viscous forces. It is a non-dimensional parameter that defines the characteristics of the fluid flow conditions. It is used when calibrating the lift and drag coefficients of an airfoil. For a high speed rotor,

the Reynolds number is:

$$Re = \frac{cU_{IF}}{\nu} \quad (3.4)$$

Where, c is the airfoil chord, ν represents air kinematic viscosity at 20°C, and U_{IF} is the total velocity at the interface:

$$U_{IF}^2(\theta) = U_{\infty}^2 + \omega^2 R_g^2 + 2\omega R_g U_{\infty} \cos \theta \quad (3.5)$$

R_g is the rotating domain radius and θ is the azimuth angle between $\theta = 0^\circ$ and $\theta = 360^\circ$ in one revolution of the turbine. In all ranges of the assumed TSRs, the Reynolds number is between $Re = 4.55 \times 10^4$ and $Re = 6.78 \times 10^4$, which is identified as a low Reynolds regime.

3.1.4 Blade Solidity

The blade solidity, δ , is the ratio of the blade area compared with the swept area.

For a vertical axis wind turbine, the solidity is defined as:

$$\delta = \frac{Nc}{D} \quad (3.6)$$

N is the number of blades. Changing the number of blades or the blade chord dimensions will alter the VAWT's solidity. An increase in the chord results in a large aerodynamics force and consequently, a high power.

3.1.5 Tip Speed Ratio

The tip speed ratio TSR is defined as the velocity at the tip of the blade to the free stream velocity. The rotational speed can be varied by the turbine controller for a certain wind speed. The rotational speed, ω , is therefore represented by the tip speed ratio, TSR. This parameter gives the tip speed, $R_{rotor}\omega$, as a factor of the free stream velocity, U . It is given by:

$$TSR = \frac{\text{Tip speed}}{\text{wind speed}} = \frac{R_{rotor}\omega}{U} \quad (3.7)$$

3.1.6 Bezt Number

The Bezt number or Bezt limit is a useful performance indicator of wind turbines. Bezt limit is the maximum amount of power that can be extracted by a wind generator from wind kinetic energy that is available. This maximum turbine power is the difference between the upstream and downstream wind powers.

$$P_t = 0.5\left(\frac{dm}{dt}\right)(V^2 - V_0^2) \quad (3.8)$$

Where P_t = turbine output power (watts),

V = upstream wind velocity (m/s) and

V_0 = downstream wind velocity (m/s)

The mass of air flowing through the turbine rotor area is a function of the air density and velocity (upstream and downstream average),

$$\frac{dm}{dt} = 0.5\rho_{air}A(V + V_0) \quad (3.9)$$

Substituting equation (2.8) into equation (2.9), the turbine power becomes

$$P_t = 0.5 \left[\rho_{air} A \left(\frac{V + V_0}{2} \right) \right] (V^2 - V_0^2) \quad (3.10)$$

Equation (3.8) is rearranged to give the following expression:

$$P_t = 0.5\rho_{air}AU^3 \left[\frac{(1 + \frac{V_0}{V})(1 - (\frac{V_0}{V})^2)}{2} \right] \quad (3.11)$$

This power from the turbine rotor can be expressed as a fraction of the upstream wind power, i.e.,

$$P_t = 0.5\rho_{air}AU^3C_p \quad (3.12)$$

Where C_p is the fraction of power captured by the rotor blades also known as the power coefficient or *rotor efficiency*. Re-arranging the previous results, it can be shown that:

$$C_p = \frac{(1 + \frac{V_0}{V})(1 - (\frac{V_0}{V})^2)}{2} \quad (3.13)$$

Figure 3.4 shows the variation of C_p with downstream to upstream wind speed ratio (V_0/V). The theoretical maximum rotor power coefficient is $C_p = 16/27 (= 0.59)$, when the downstream to upstream wind speed ratio is $V_0/V = 0.33$. This is called the *Betz limit*, which was carried out by Betz (1926). However, the practical limits for C_p are typically 0.46 for a high-speed two-blade system, and 0.50 for three-blade turbines.

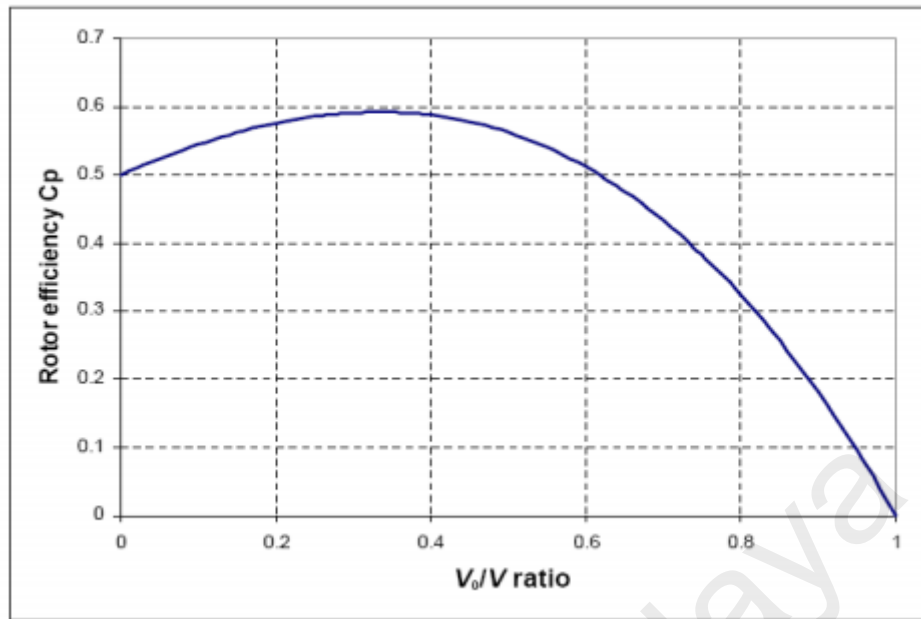


Figure 3.4: Rotor efficiency vs. downstream / upstream wind speed ratio(Patel, 1999).

As with all turbines, only a part of the energy shown in Figure 3.4 can be extracted. If too much kinetic energy was removed, the exiting airflow would stagnate, thus causing a blockage. When the airflow approaches the inlet of the turbine, it meets a blockage imposed by the rotor-stator blades. This causes a decrease in kinetic energy, while the static pressure increases to a maximum at the turbine blade. As the air continues through the turbine, energy in the fluid is transferred to the turbine rotor blades, while the static pressure drops below the atmospheric pressure as the fluid flows away from the rotor. This will eventually further reduce the kinetic energy. Then kinetic energy from the surrounding wind is entrained to bring it back to the original state.

3.1.7 Rotor Performance Parameters

A wind turbine designed for a particular application should have its performance characteristics tested before proceeding to prototype fabrication. A dimensionally similar and scaled down prototype of the design model is normally tested in a wind tunnel for this purpose. The power performance of a wind turbine is normally expressed

in dimensionless form. For a given wind speed, the power coefficient, torque coefficient and the tip speed ratio are good indicators to use as a performance measure. For a particular configuration of the VAWT, these parameters are:

$$C_m = \frac{\text{Torque}}{0.5\rho U_\infty^2 AR_{rotor}} \quad (3.14)$$

$$C_p = \frac{P_t}{0.5\rho U_\infty^3 A} \quad (3.15)$$

$$C_p = (TSR)C_m \quad (3.16)$$

Where $A=HD$, D is the rotor diameter and H is the height of turbine. In addition, C_p and TSR (tip speed ratio) of equation 3.7 are dimensionless values used in predicting the performance of the turbine.

3.2 RESPOND SURFACES METHODOLOGY

RSM is an assortment of statistical techniques and mathematics which are valuable to the analysis and modelling of problems. One or more responses are subjective with several variables and the goal is the optimization of the responses (C Montgomery, 1997). Furthermore, RSM calculates relationships between the vital input factors and one or more measured responses. Results of the RSM are illustrated either by graphical and numerical tools, or with the inspection of the interpretation plots (Noordin, Venkatesh, Sharif, Elting, & Abdullah, 2004).

The *RSM* is important in designing, formulating, developing, and analyzing new scientific studies and products. It is also efficient in the improvement of existing studies and products. The most common applications of *RSM* are in Industrial, Biological and Clinical Science, Social Science, Food Science, and Physical and Engineering Sciences. Since *RSM* has an extensive application in the real world, it is also important to know how and where *Response Surface Methodology* started in the history. According to

Kuri and Mukhopadhyaya (2010), the *RSM* method was introduced by G.E.P. Box and K.B. Wilson in 1951 (Wikipedia 2006). Box and Wilson suggested using a first-degree polynomial model to approximate the response variable.

3.2.1 Response Surface Methods and Designs

Response Surface Methods are designs and models for working with continuous treatments when finding the optima or describing the response is the goal (Oehlert, 2000). The first goal for the Response Surface Method is to find the optimum response. When there is more than one response then it is important to find the compromise optimum that does not optimize only one response (Oehlert, 2000). When there are constraints on the design data, the experimental design has to meet requirements of the constraints. The second goal is to understand how the response changes in a given direction by adjusting the design variables. In general, the response surface can be visualized graphically. The graph is helpful to see the shape of a response surface; hills, valleys, and ridgelines. Hence, the function $f(x_1, x_2)$ can be plotted versus the levels of x_1 and x_2 as shown as Figure 3.5.

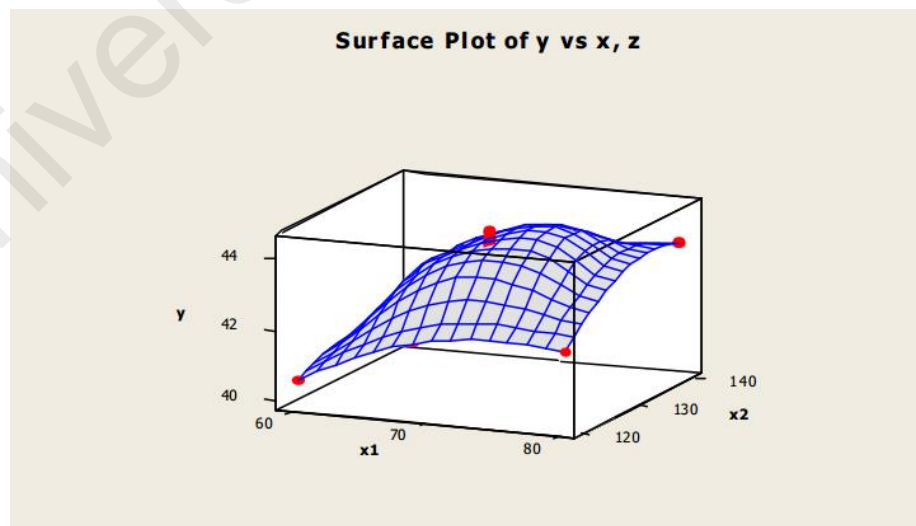


Figure 3.5: Response surface plot $y = f(x_1, x_2) + e$

In this graph, each value of x_1 and x_2 generates a y -value. This three-dimensional graph shows the response surface from the side and this is called a response surface plot. Sometimes, it is less complicated to view the response surface in two-dimensional graphs. The contour plots can show contour lines of x_1 and x_2 pairs that have the same response value for y . An example of a contour plot is shown in Figure 3.6.

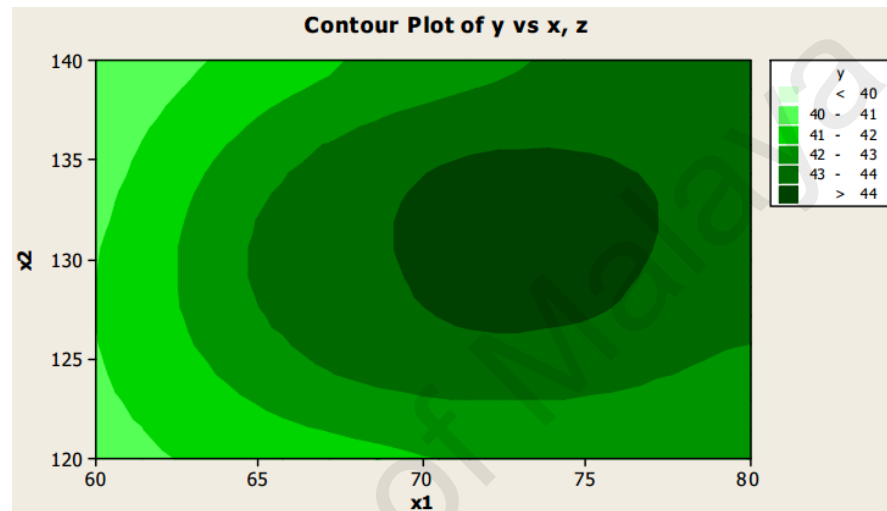


Figure 3.6: Sample of Contour plot in RSM.

In order to understand the surface of a response, graphs are helpful tools. Nevertheless, when there are more than two independent variables, graphs are difficult or almost impossible to use to illustrate the response surface since it is beyond 3-dimension. For this reason, response surface models are essential for analyzing the unknown function f .

3.2.2 Designs for Fitting Second-Order Model

There are many designs available for fitting a second-order model. The most popular one is the *central composite design* (CCD). This design was introduced by Box and Wilson. It consists of factorial points (from a 2_q design and 2_{q-k} *fractional factorial design*), central points, and axial points. The following is the representation of the 2_q axial points:

x_1	x_2	...	x_q
$-a$	0	...	0
a	0	...	0
0	$-a$...	0
0	a	...	0
.
.
.
0	0	...	$-a$
0	0	...	a

CCD was often developed through a *sequential experimentation*. When a first-order model shows an evidence of *lack of fit*, axial points can be added to the quadratic terms with more center points to develop the CCD. The number of center points n_c at the origin and the distance a of the axial runs from the design center are two parameters in the CCD design. The center runs contain information about the curvature of the surface if the curvature is significant. The additional axial points allow the experimenter to obtain an efficient estimation of the quadratic terms. The Figure 3.7 illustrates the graphical view of a central composite design for $q = 2$ factors.

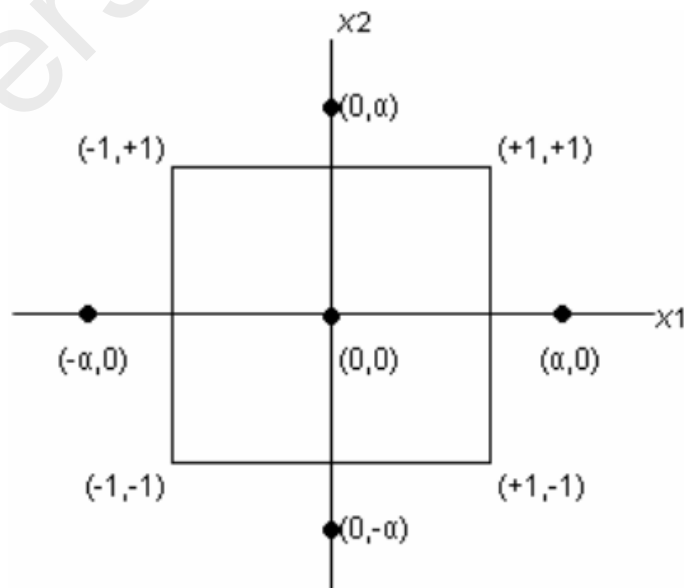


Figure 3.7: Central Composite Design for $q = 2$.

There are a couple of ways of choosing α and n_c . First, the CCD can run in incomplete blocks. A block is a set of relatively homogeneous experimental conditions so that an experimenter divides the observations into groups that are run in each block. An incomplete block design may be conducted when all treatment combinations cannot be run in each block. In order to protect the shape of the response surface, the block effects need to be orthogonal to the treatment effects. This can be done by choosing the correct α and n_c in factorial and axial blocks. Also, α and n_c can be chosen so that the CCD is not blocked. If the precision of the estimated response surface at some point x depends only on the distance from x to the origin and not on the direction, then the design is said to be rotatable (Oehlert, 2000). When the rotatable design is rotated about the center, the variance of \hat{y} will remain same. Since the reason for using the response surface analysis is to locate unknown optimization, it makes sense to use a rotatable design that provides equal precision of estimation of the surface in all directions. The choice of α will make the CCD design rotatable by using either $\alpha = 2^{q/4}$ for the full factorial, or $\alpha = 2^{(q-k)/4}$ for a fractional factorial.

3.3 EXPERIMENTAL TEST ON THE OPTIMIZED ODGV

Augmented VAWT is tested in the lab to find out the performance of this apparatus in the real world. This performance of the augmented VAWT with optimized ODGV is compared against a bare VAWT with 4, 5 and 6 bladed guide vanes. A schematic view of the experimental test is shown in Figure 3.8. Lab test was conducted in the Eco Green lab in University of Malaya. This test consists of three major parts that are the VAWT, ODGV and the blowing fans. ODGV and VAWT are located on top of the stand with a length of 800mm. These two parts were placed 3500mm from the blowing fans. Nine blowing fans produced a flow around the augmented rotor where these fans were placed in three rows with a height of 500mm, 1000mm and 1500mm.

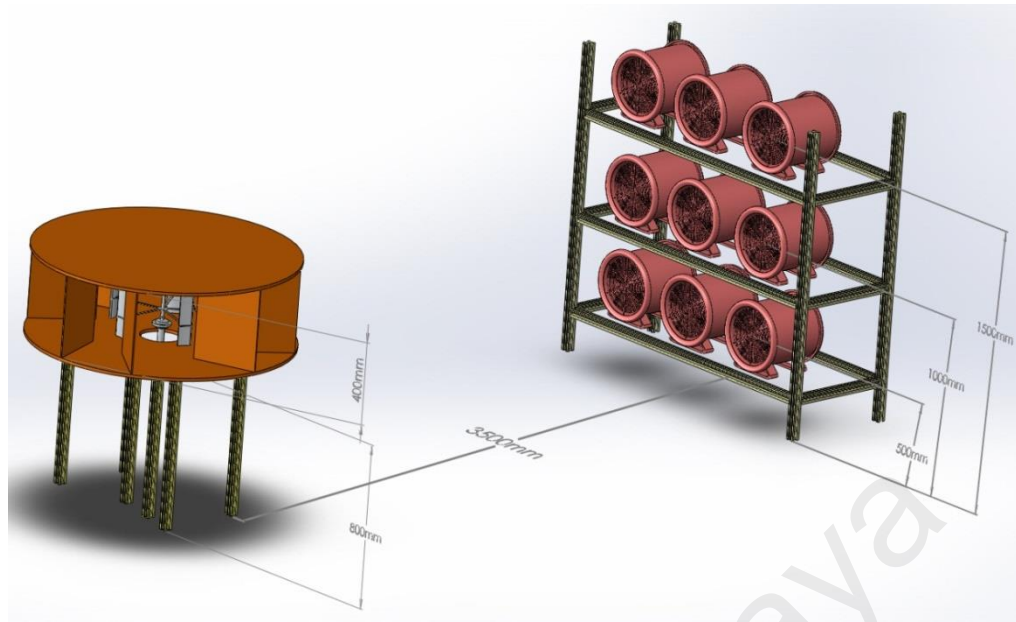


Figure 3.8: Schematic view of the experimental test.

3.3.1 Fabrication of the ODGV

As it can be seen in Figure 3.9, an *optimized ODGV* consists of four sets of the twin guide vanes. Optimization of this ODGV is reported in the next following chapter. These guide vanes are made of acrylic sheets. Using these sheets is easy as it can be cut easily and is not heavy to carry. Therefore, this material was used as the guide vanes.

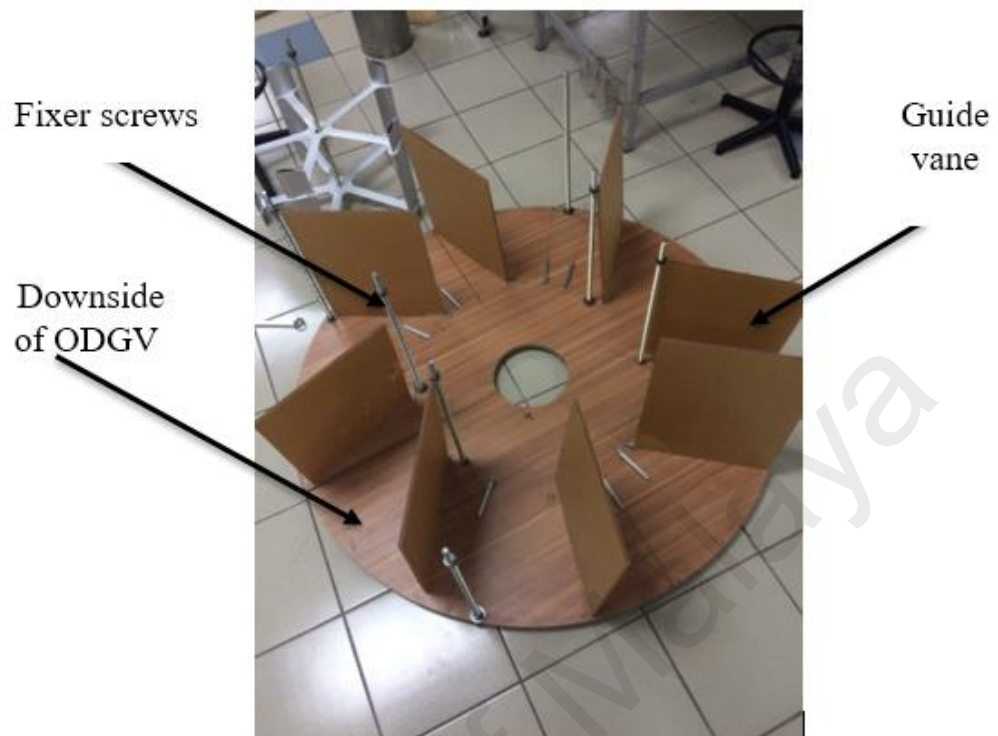


Figure 3.9: Top view of the ODGV.

Eight long screws were cut to fix the upper and bottom side of the ODGV. Sizes of these screws are 410mm. As discussed in the next chapter, the optimum size of the ODGV should be between 1200mm to 1300mm. The optimum case is the ODGV with an outer diameter equal to 1272mm. Therefore, upper and bottom part of the ODGV is cut to the diameter of the same results of the CFD (1272mm). These two sides of the ODGV are made of Medium-density fiberboard (MDF). MDF is used because it is cheap and easy to modify. The size of these boards are very big to carry so these parts are cut in half to make them easy to carry. The bottom side of the ODGV also had a hole ($\Phi=100\text{mm}$) to allow the turbine shaft passing through.

In order to fix the angle of the guide vanes and easier modification of the positions of the guide vanes, aluminum guide rails were mounted on the upper and bottom side of the ODGV. These guide rails were fixed from one side so that changing

the angle of the guide vanes was accessible. As you can see in Figure 3.10 there are some marks on the bottom side of the ODGV. These marks show the position of the ODGVs guide vanes in different configurations.



Figure 3.10: Guide rails.

After assembling the ODGV, it became two completed parts. The left hand side of the ODGV is shown in Figure 3.11. These two parts were also connected together to make one single piece.



Figure 3.11: Assembled ODGV.

3.3.2 Wind Turbine

A vertical axis wind turbine with a diameter of 500mm was used for this experiment (see Figure 3.12). This turbine is made from a company called Saiam Power. This turbine is used in any areas where good wind resources are available such as buildings of roofs in cities, environmentally friendly buildings and dependent small power station in the suburbs.



Figure 3.12: Wind turbine.

As one of the key components in a wind turbines, the rotor blades are responsible for converting the kinetic energy of the wind into mechanical energy first, and then into electricity if needed (Butbul, MacPhee, & Beyene, 2015). The airfoil type in this VAWT is a FX 63-137. The pitch angle of the blades is set as 10° and the pressure center is located in the midsection of the blades at $0.5c$. The characteristics of the wind turbine and its airfoils are listed in Table 3.1.

Table 3.1: Properties of the wind turbine and airfoil.

Geometry of turbine	Dimensions
blade airfoil section	Fx 63-137
Blade chord(c)	78 mm
Radius of the turbine(R)	250mm
Solidity(Nc/D)	0.78
Max camber	5.8% at 56.5% c
Height(H)	520mm
Aspect ratio(H/D)	1.04
Thickness t	13.75 mm

3.3.2.1 Major Components of the Wind Turbine

The whole unit consists of the pillar, wind generator, blades, and flanges. The mill is pushed by wind at a speed of 3 m/s to 20 m/s to rotate and make the generator produce power in an AC form.

3.3.2.2 Installation Process of the Wind Turbine

The first step in installation of the VAWT was connecting the pillar to the generator, as it can be seen in Figure 3.13. These two parts were screwed tight with M10 nuts, washer (Φ 5) and spring washers (Φ 5).



Figure 3.13: Installation of the pillar to the generator.

The bottom part of the pillar was also connected to the test rig with the same screws and washers. (Figure 3.14).



Figure 3.14: Connection between pillar and test rig.

The next step was connecting the nether flange or supporting arms with axis by screwing them tightly with the M10 nuts and washer ($\Phi 10$), and spring washer ($\Phi 10$). In the next step, blades were connected to the supporting arms. Finally, the ($\Phi 6$) washer is put through the top of the axis, where the upper supporting arms is connected to the axis with tightly screwed M6 nuts, washers ($\Phi 6$), spring washers($\Phi 6$) and inserted split cotter pin (Figure 3.15).



Figure 3.15: supporting arms.

3.3.3 Augmented turbine

The vertical axis wind turbine was augmented in an Omni-direction-guide-vane. These two were placed on top of the test rig. This rig is shown in Figure 3.16. To arrange the height of the wind turbine inside the ODGV, the middle part of the rig was designed to be adjustable. Assembled augmented wind turbine is shown in Figure 3.16.



Figure 3.16: Assembled augmented VAWT.

3.3.4 Blowing fans

Nine blowing fans were used to create the flow around the wind turbine. These fans are made at the ICASU Company. By using the 520 w power in these fans, they produce air delivery around $65\text{m}^3/\text{min}$ at the speed of 2800rpm. Other specifications and configurations of the positions of these fans are shown in Figure 3.17 and Table 3.2.



Figure 3.17: Series of the blowing fans.

Table 3.2: blowing fans specification

Specification	
Power	520 W
Speed	Rpm
Air Delivery	65m ³ /min
Diameter	12 inch
Wind pressure	370kpa

3.3.5 Measurements Apparatus

3.3.5.1 Anemometer

To measure the velocity around the field, a device called the anemometer is used. This device has two probes: the Anemometer probe and the Humidity/ Temp probe. Low-friction ball vane wheels makes sure that there is a high accuracy of 182 x 73 x 47.5 mm in high & low velocities. The SD card was taken away from the meter and plugged into the Data Acquisition software, SW-U801-WIN. When the SD card is in the computer, it can download all the Excel Data Acquisition software, SW-E802. Values

can be measured with the time information directly. The users can then make further data or graphic analysis by themselves.

3.3.5.2 Dynamometer

Performance of the VAWT can be extracted by plotting the C_p curve versus tip speed ratio. A device named dynamometer shows the amount of the torque generated in a VAWT. This dynamometer controller allows the user to control in several different modes: Manual, Speed, Torque, Road Load (RPM) and Computer (remote) mode. Use of these modes depends on the specifics of testing. For simple loading of the wind turbine (ie. adding or reducing the load), the mode used will be the Manual Control mode. For constant speed operation (where torques will vary), the Speed Control mode is used. Road Load mode is commonly used to simulate the aerodynamic load a vehicle has when operated on the road. Computer control mode is used for automated testing, often in conjunction with the throttle control, which can also be operated remotely from the computer. The front and backside of the dynamometer controller is shown in Figure 3.18 and Figure 3.19.



Figure 3.18: Dynamometer front view.

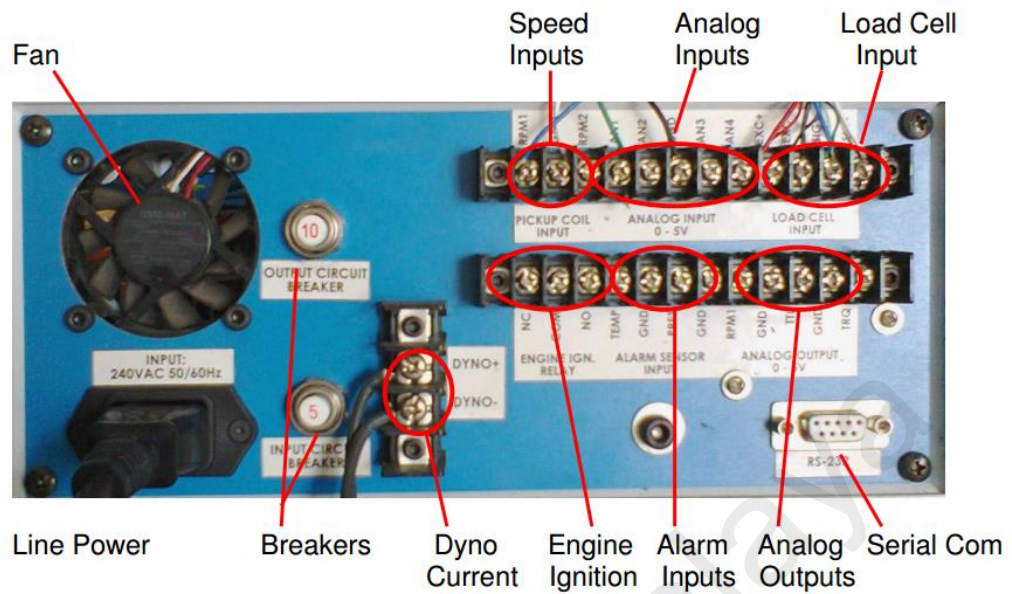


Figure 3.19: Dynamometer back view.

3.3.5.2.1 Computer Communications

A computer can be connected to the dynamometer controller for logging data from the Dynamometer Controller, Fuel Scale and Data Acquisition systems via Serial Ports. If serial ports are unavailable, then a USB-Serial Port converter may be used. Serial port communications are via RS232: 9600 baud. In Verbose mode, the controller automatically sends data out in the format shown below at approximately 4Hz. When the power is on, the controller sends out a “Power On” message with the firmware code. Data can be logged from various serial communications programs including the HyperTerminal. Various controller parameters can be modified from the computer interface where data can be logged by the computer as well. In Verbose mode, the controller will automatically output the data to the serial port every 250ms. When the control is NOT in Verbose mode, sending the character “A” will cause the controller to respond to the data.

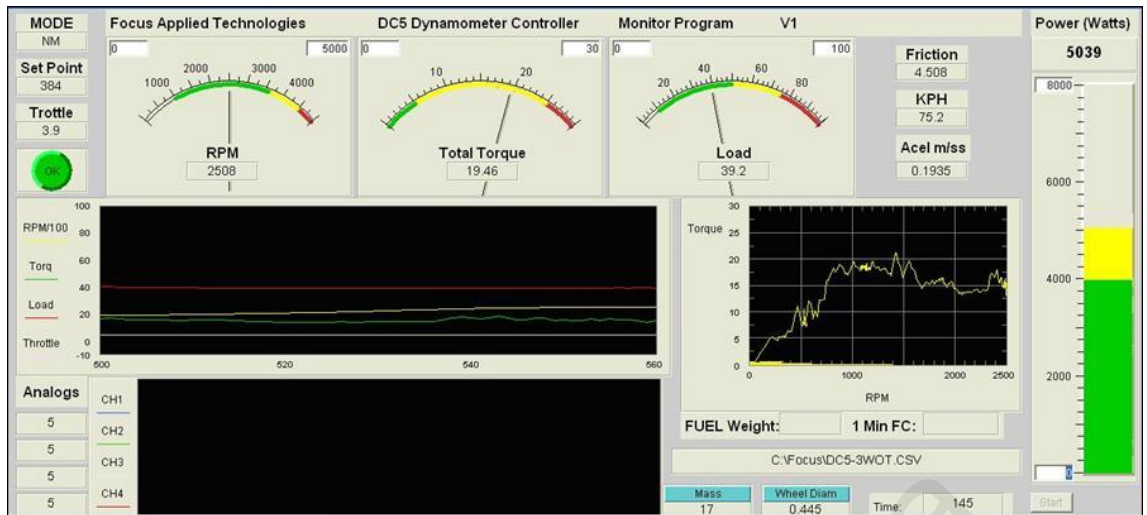


Figure 3.20: Interface of the dynamometer controller in computer.

Figure 3.20 shows the interface of the dynamometer controller in the computer. The interface has three gauges that shows the RPM, torque and percentage of the load. It also monitors the mechanical power that is generated in the VAWT. This interface saves the data every second for current, voltage, time, RPM and torque.

3.3.6 Dynamometer Startup Procedure

- Visually inspect all components of the dynamometer system and wind turbine to make sure that there are no missing or broken components and loose items, which may cause damage.
- Check Dump Load.
- Turn Computer ON.
- Turn Dynamometer Current to the OFF position.
- Switch the Mode selector switch to MANUAL mode.
- Set the Set Point Adjust to 0%.
- Turn the Dynamometer Controller and Power Unit ON.
- Start the blowing fans.
- Let the wind turbine reach highest speed of rotation with free load .

- Start to add the load by 5% each time.
- Wait to stabilize the rotation speed of the VAWT (minimum 5 min).
- Add 100% of load and the test is done.

3.4 NUMERICAL MODELING

3.4.1 GEOMETRY OF VAWT

A 3-D model of the VAWT was generated by using the Solid Works CAD software. It is a straight-bladed Darrieus turbine with a rotor diameter of $D_R = 500$ mm. The rotor consisted of five blades, and each blade was attached to a central shaft by two supporting arms. Figure 3.21 shows a 3D model of the VAWT.

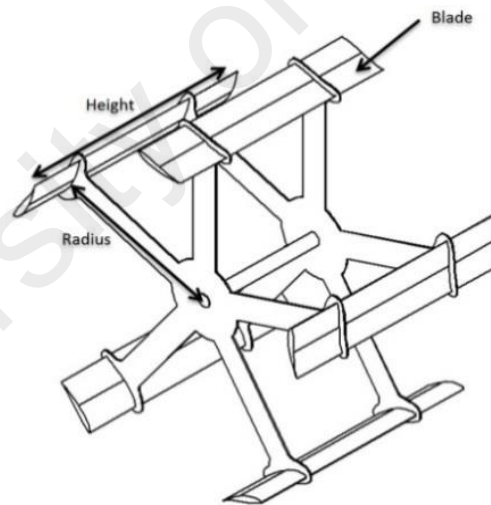


Figure 3.21: 3-D model of the VAWT

Generally, in order to reduce the computational time and understand the effect of the ODGV on the VAWT, a CFD simulation was carried out on a 2-D model. This 2-D model was extracted from the middle section of the 3-D model. Therefore, the effect of the supporting arms and central shaft was not considered.

3.4.2 GEOMETRY OF ODGV

The base design of the ODGV was considered from Chong et al (W. Chong et al., 2013). The ODGV comprised of four sets of twin walls. Figure 3.22 shows the 3-D model of the ODGV.

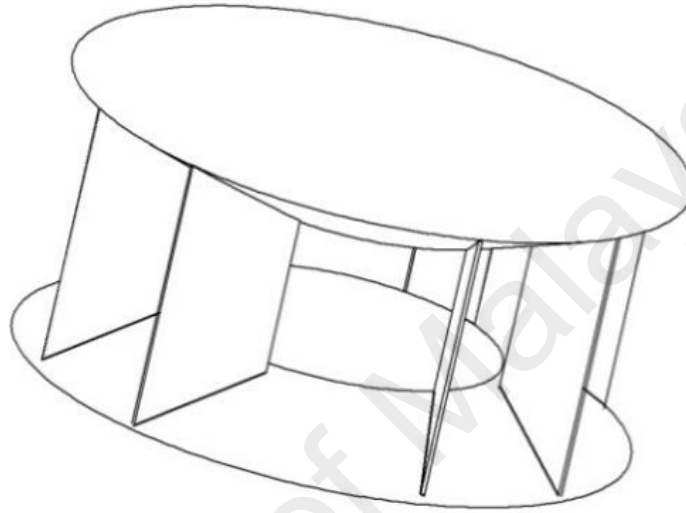


Figure 3.22: Three-dimensional model of the ODGV.

The 2-D model design is generated as:

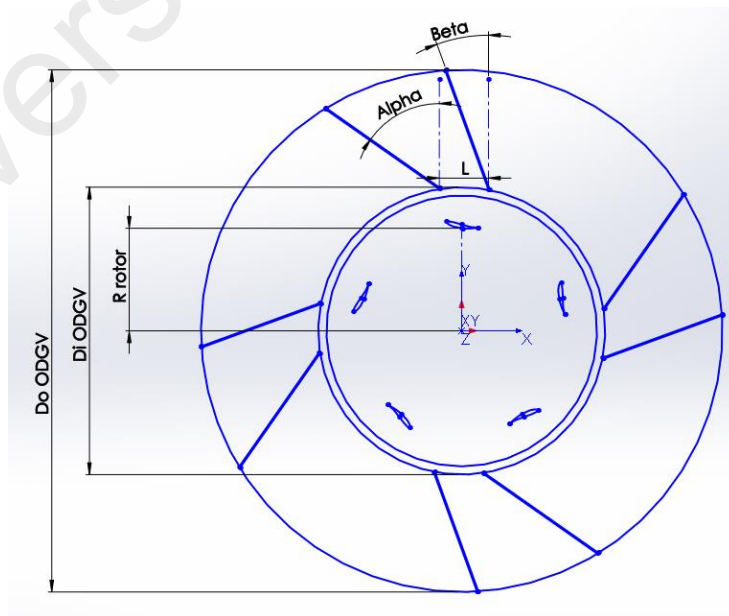


Figure 3.23: Top view of VAWT integrated with ODGV.

The inner diameter of the ODGV is fixed at 700mm, where the rotor diameter is 500-mm. The outer diameter, first angle of guide vane α and second angle β and inner length L factors were investigated.

3.4.3 CFD Solver

The CFD package, ANSYS Fluent 15.0, was used for all the simulations performed in this study. The code uses the finite volume method to solve the governing equations for fluids. More specifically in this thesis, the incompressible, unsteady Reynolds Averaged Navier–Stokes (URANS) equations were solved for the entire flow domain. The coupled pressure–based solver was selected with a second order implicit transient formulation for improved accuracy. All solution variables were solved via the second order upwind discretization scheme since most of the flow can be assumed to be not in line with the mesh (Fluent, 2009).

3.4.4 The wind tunnel numerical domain

A two–dimensional CFD model was used to represent the VAWT and the wind tunnel domain. This was based on the review of relevant literatures (Amet et al., 2009; Castelli et al., 2010; Consul et al., 2009; Danao et al., 2014; J. Edwards et al., 2007; J. M. Edwards et al., 2012; CJ Simao Ferreira et al., 2007; Carlos Simao Ferreira et al., 2007a; Hamada et al., 2008; Howell et al., 2010; K. McLaren et al., 2012; Raciti Castelli et al., 2011; Tullis, Fiedler, McLaren, & Ziada, 2008) that has shown that a 2D model is sufficient in revealing the factors that influence the performance and majority of flow physics that surround the VAWT. The contributions of blade end effects and blade –support arm junction effects were neglected but deemed acceptable since these can be considered as secondary. Two-dimensional VAWT models are essentially VAWTs with infinite aspect ratio blades. The effect of blade aspect ratio (AR) comes in

the form of shifting the C_p curve upwards and to the right as AR increases (Simon Charles McIntosh, 2009), but the general shape is maintained. The complexity, as well as the computational expense for a full three-dimensional model cannot be justified by the additional insight that such a model can offer and it is left for future research.

Mohamed et al. (2015) reported that the size of the wind tunnel affects the variation of the rotor power coefficient. In addition, they recommended that the wind tunnel should be extended by at least 10 times the rotor diameter in each direction. Figure 3.24 indicates the domain of the wind tunnel.

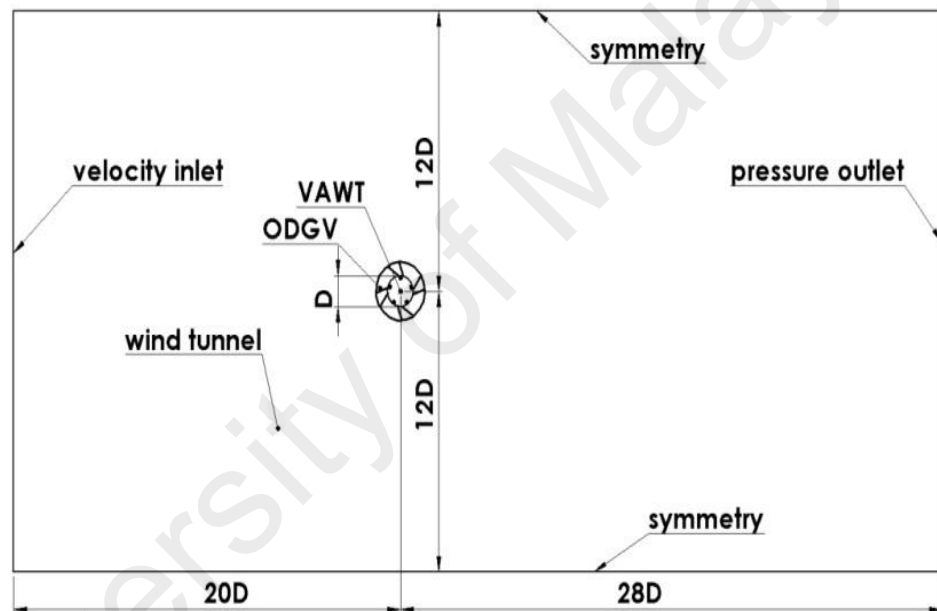


Figure 3.24: Wind tunnel (Domain).

According to Figure 3.24, the domain size is 20D from the inlet, 28D from the outlet and 12D from the sides. For the primary boundary condition, the inlet is set as a velocity inlet with a constant wind velocity profile of 4.5 m/s, while the outlet is set as a pressure outlet ($P_{\text{outlet}} = 0$) with atmospheric pressure value.

The domain mesh was created directly in the grid generation software, the Ansys mesh generator, where the aerofoil coordinates of an Fx-63-137 profile were imported to define the blade shape. The surrounding geometry was defined based

on the studies of the extents of the boundaries that are detailed in later sections. There is an inner circular rotating domain connected to a stationary rectangular domain via a sliding interface boundary condition that conserves both the mass and momentum.

No-slip boundaries are set to represent the wind tunnel walls. The rotation of the inner domain relative to the outer domain is prescribed within the software that implements the algorithm for the sliding mesh technique. Precautions are taken such that tolerance between meshes in the interface region is kept low to avoid excessive numerical diffusion. Each blade surface was meshed with 1595. The unstructured mesh was adapted for the model, where a boundary layer was inflated from the blade surface (Figure 3.27). The first cell height used was such that the y^+ values from the flow solutions did not exceed two. To ensure proper boundary layer modelling, the growth rate of the inflation was set to 1.01 to give a minimum of 10 layers within the boundary layer, after which a larger growth rate of 1.05 was implemented. A control ellipse is used around the blades to minimize the dissipation of the turbulent structures generated by the blades in the upwind region that may interact with the other blades in the downwind region. A smoothing algorithm in the meshing software was used to reduce the angle skewness of the cells such that the maximum was observed to be less than 0.6.

The sidewall distance was set to $d_s = 12D$ from the VAWT axis. A wall distance study was carried out to examine the effects of blockage in the 2D simulations. Time step convergence was monitored for all conserved variables and it was observed that acceptable levels of residuals (less than 1×10^{-6}) were attained after six rotations of the VAWT. This means that periodic convergence was also achieved. After the sixth rotation, the peaks of the upwind torque for cycles 7

through 9 were level and the downwind ripple matched closely. The difference in the average torque between cycle 7 and cycle 9 is around 0.05%.

3.4.5 Mesh generation and boundaries

As shown in Figure 3.24 , the 2-D fluid domain is composed of two distinct domains; a fixed rectangular outer domain with a circular aperture; and a circular inner domain to fit into the aperture. The fixed rectangular outer domain was identified as the numerical wind tunnel domain, and the circular inner domain was identified as the rotational domain resembling the wind turbine. To create an accurate mesh around the rotating zone, the inside of the turbine was divided into sub sections. The control ellipses enclosed around the airfoils are depicted in Figure 3.25.

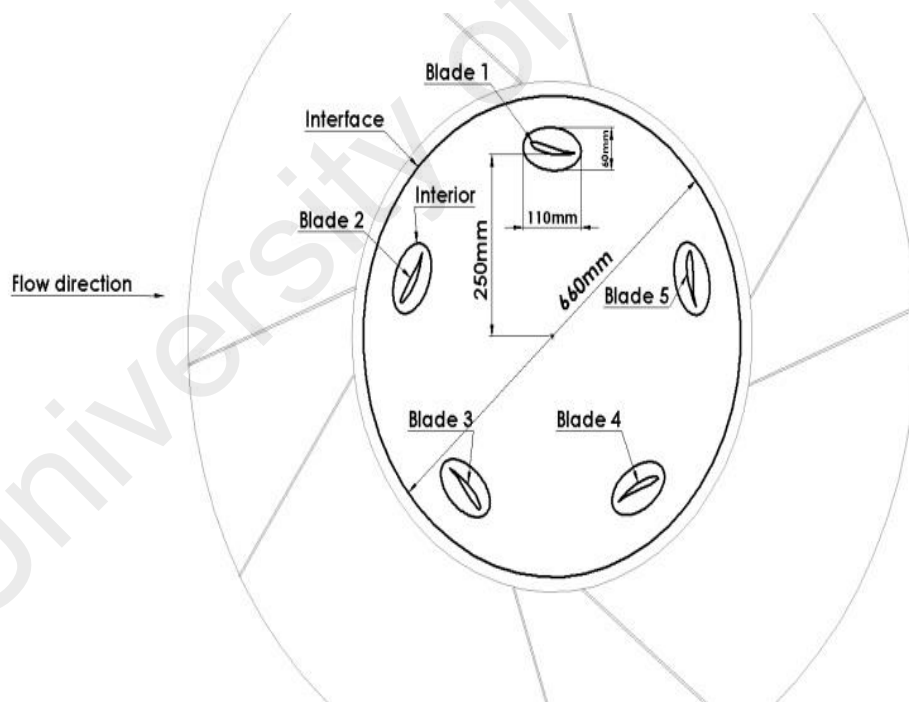


Figure 3.25: Boundary around VAWT.

As seen from Figure 3.25, the moving mesh approach was employed to show the rotating zone and an interface boundary created between the rotating and non-rotating sections. The same density of mesh was selected for both sides of the interface to obtain

a faster convergence (Fluent, 2009). Initial position of the blades is also shown in Figure 3.25. Blade 1 starts from $\theta = 0^\circ$, while the initial positions of the blades number 2, 3, 4 and 5 are $\theta = 72^\circ, 144^\circ, 216^\circ, 288^\circ$ respectively. Considering the complexity of the geometry, an unstructured mesh was chosen. The first and second size functions were employed to generate mesh from blades and control elapse to the rotor interface respectively. The third functions were used to generate mesh for the wind tunnel domain and the fourth size function generated mesh on the ODGV. These four functions are defined in Table 3.3.

The generation of mesh starts from the airfoils, 0.1 mm was considered as the optimum size of mesh around the airfoil after the mesh independency test. The mesh was expanded with the first size function with a ratio of 1.05 from 0.1 mm to 0.5mm, which is indicated by Figure 3.26.

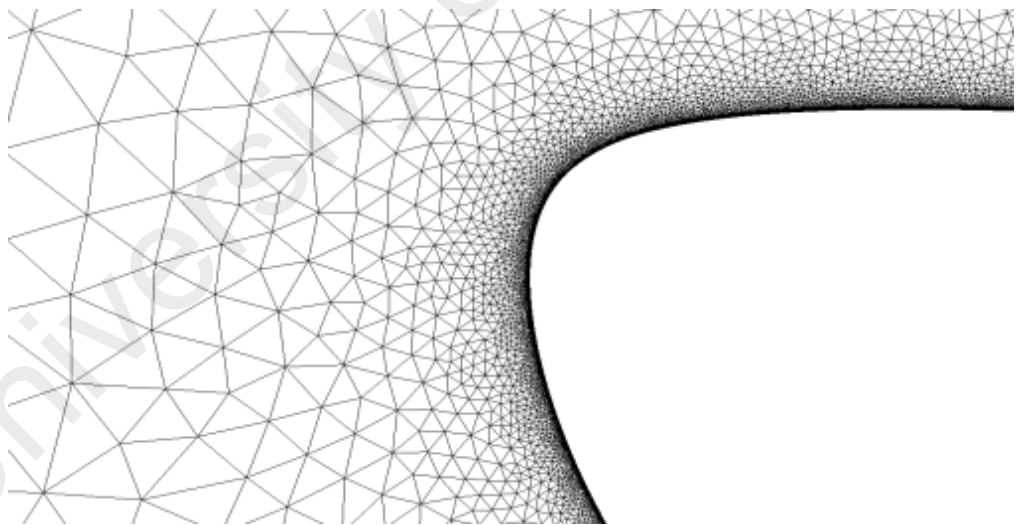


Figure 3.26: Density of the mesh near the blade.

In order to accurately capture the flow behavior and obtain a suitable Y_{plus} range around the blades, ten boundary layers of the structural mesh were generated and illustrated in Figure 3.27.

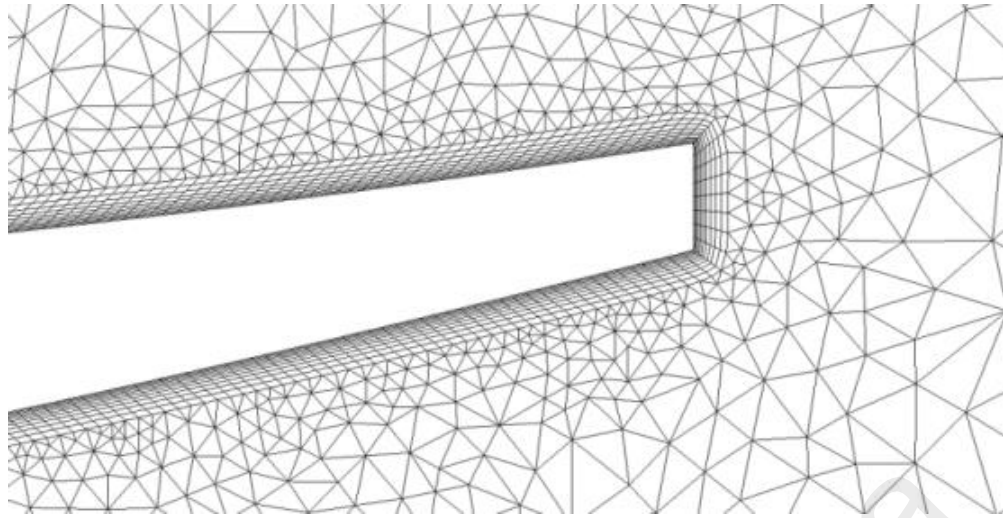


Figure 3.27: Boundary layers mesh around blade.

In order to control the grid elements dimension near the blades, the blades were enclosed in a control ellipse which is shown by Figure 3.28.

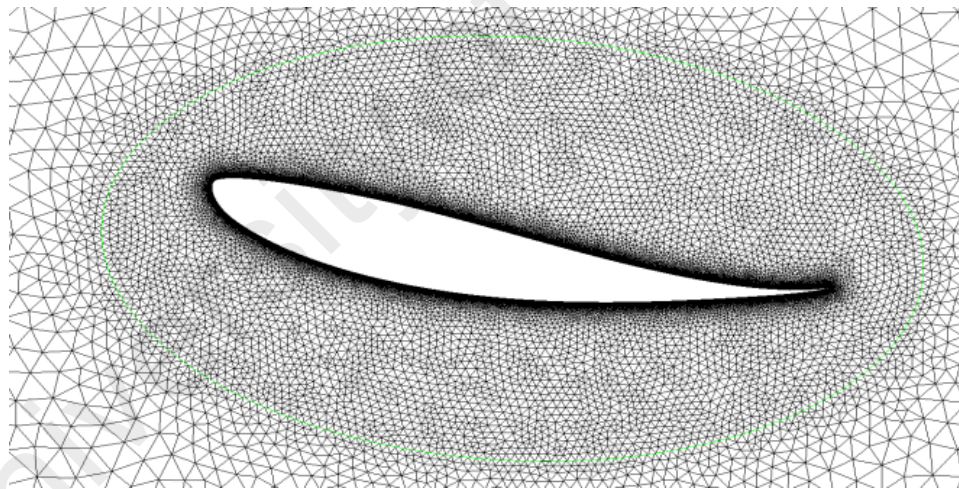


Figure 3.28: Control ellipse.

Control ellipses, unlike the interface, has no physical significance. The second size function with a ratio of 1.05, generates the mesh from the control ellipse with a mesh size of 0.5mm, to the rotational zone with a mesh size of 2mm. The last size function created a mesh from the interface to the wind tunnel domain with a ratio of 1.05. Mesh was expanded from 2 mm to 200 mm in the wind turbine domain. After this, concerning the ODGV geometry, another size function was used to cover the gap

between the ODGV and interface with a ratio of 1.1 from 2 mm to 5 mm. In addition, the size of ODGV mesh in all cases was 5 mm.

3.4.6 Blades Y_{plus}

One important criterion in every CFD simulation is the wall Y_{plus} . It is important in turbulence modeling to determine the proper size of the cells near the domain walls. The turbulence model laws have restrictions on the Y_{plus} value at the wall. This dimensionless wall distance depends on the first cell height. In this study, Y_{plus} values were measured for the various positions of one airfoil between 0 and 1 for 5 different Azimuth angles including 0° , 72° , 144° , 216° and 288° in $TSR=1.6$.

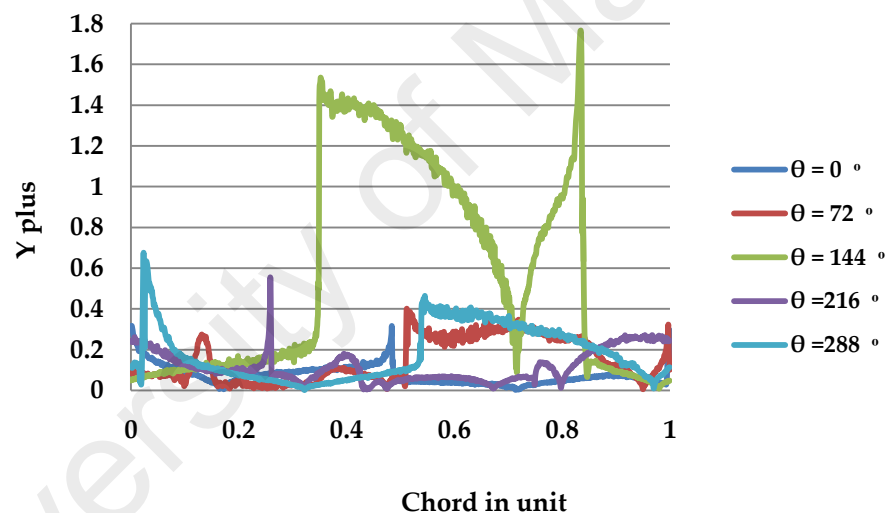


Figure 3.29: Results for Y_{plus} values at $TSR=1.6$.

As it can be seen from Figure 3.29, the maximum value for Y_{plus} is in $\theta = 144^\circ$ which equal to 1.8. For the rest of the airfoil positions, it can be observed that the Y_{plus} range is less than 0.7.

3.4.7 Domain Size

The extent of the stationary domain was dictated by the necessity to properly simulate the wind tunnel configuration within a two-dimension simulation. For both the sidewalls and the outlet boundaries, independent studies were carried out to determine the effects of the distance of the said boundaries to the predicted C_p in a wide range of TSR.

3.4.7.1 Side Wall Distance d_s

The position of the wind tunnel walls in the 2-D domain is the main parameter that influences blockage. Since it is difficult to validate the blockage effects of the 2-D model versus the actual experiments, it was deemed sensible to match only the blockage ratio of the two. However, a one-to-one comparison between 2-D models can be performed to assess the effects of blockage in the predicted performance to give insight on the trend of C_p as a function of blockage. The distance of the sidewall from the VAWT axis was first set to $d_s = 5D$. For the 2-D numerical model, the computed blockage ratio was 0.58. This is double the actual blockage ratio of the wind tunnel at 0.29. The effects were seen to be significant over the prediction of C_p at TSR = 1 up to TSR = 1.6 (Figure 3.30). The maximum C_p during the wind tunnel testing was 0.075, while the predicted C_p in $d_s=5D$ was 0.11.

As d_s is increased to 12D, the predicted maximum C_p drops from 0.11 at TSR = 1.2, to $C_p=0.084$ at TSR=1.2. A $d_s=12D$ gives a blockage ratio equivalent to the actual wind tunnel blockage ratio. A further increasing d_s only slightly reduces the C_p between TSR=1.2 to TSR=1.6 by as much as $\Delta C_p = 0.0095$. As such, the d_s selected for the rest of the numerical work was 12D.

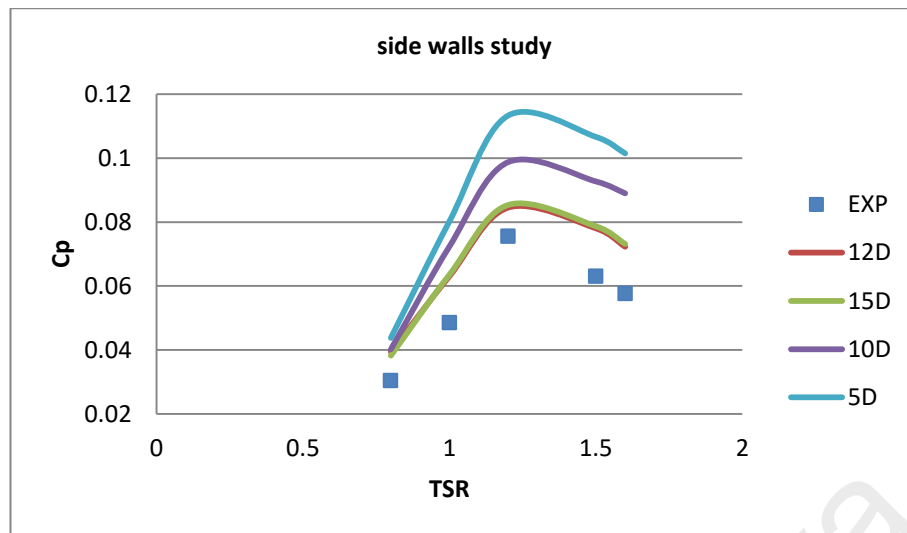


Figure 3.30: Blockage study results.

3.4.7.2 Outlet Distance d_o

The outlet distance d_o was investigated to assess the influence of wake development on the predicted C_p . The shortest d_o was set to 15D, while the longest was 40D. Result of the power coefficient in different TSRs for different domain sizes is shown in Figure 3.31. As it can be seen, domain size of 15D and 20D were not be able to predict the results of the C_p accurately. A very small deviation of the prediction of the C_p was capture between the domain size of 40D and 28D (Figure 3.31). This is deemed very small and therefore negligible. As such, the initial d_o of 28D was chosen for all the remaining numerical runs.

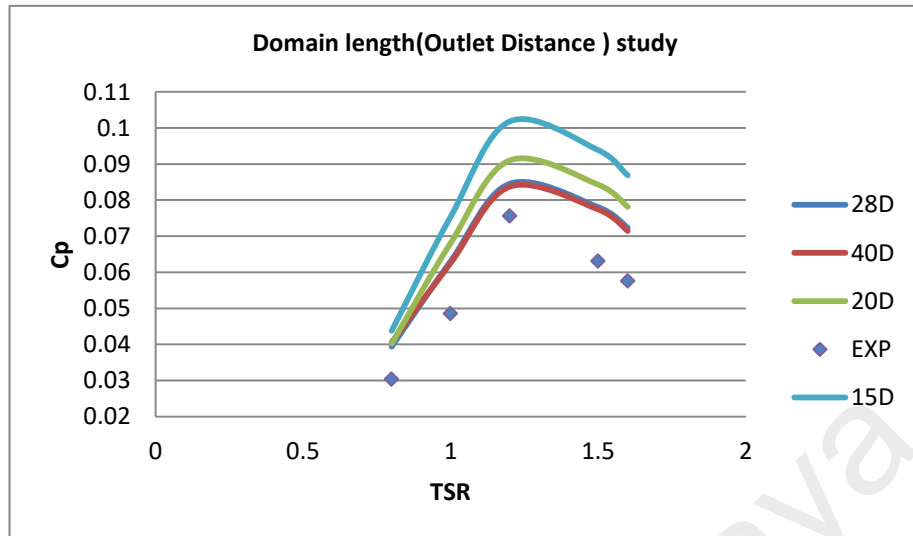


Figure 3.31: Domain length (Outlet Distance) study results for the 2D numerical model.

3.4.8 Mesh Dependency Study

A full 2-D model of a vertical axis wind turbine was widely analysed by a large number of researchers who achieved a mesh independent solution. McLaren et al. (K. McLaren et al., 2012) carried out a mesh independency study with 989 elements on each airfoil and a total mesh count of 485,000 nodes. A systematic refinement of the mesh from 600,000 to 1,000,000 cells was performed by Castelli (Raciti Castelli et al., 2011) to obtain a mesh independent solution. It is important to highlight that coarse meshes in the range of 100,000 to 300,000 cells were employed by some researchers such as (Chen & Kuo, 2013; Dai & Lam, 2009; Guerri, Sakout, & Bouhadeh, 2007; Gupta & Biswas, 2010). In these cases, a non-transitional model was applied for the airfoil when a number of the cells on surface is fixed. Although this model resulted in a smooth solution, it is not required to have a mesh independent solution. Therefore, a further mesh independency analysis was required in this situation. A more detailed mesh independency study was performed by Maître et al. (Maître, Amet, & Pellone, 2013) who systematically employed seven various cases. However, six of these cases

have the same number of cells on the blades, which means that this mesh independent solution was not accurate.

The accuracy of the CFD simulation is highly dependent on the quality of the mesh. To determine this effect, many simulations have been carried out in this study. Table 3.3 shows mesh properties in different situations.

Table 3.3: Mesh properties

Mesh	Ratio Start Size End size	Size Function 1	Size Function 2	Size Function 3	Size Function 4	Mesh size on airfoil (mm)	Number of nodes on airfoil surface	Simulation average time (h)	Number of total cells
M1	Ratio Start Size End size	1.1 0.3 0.5	1.1 0.5 5	1.1 5 200	1 5 5	0.3	532	1	150000
M2	Ratio Start Size End size	1.05 0.25 0.5	1.05 0.5 3	1.05 5 200	1.1 3 5	0.25	638	4	255000
M3	Ratio Start Size End size	1.05 0.2 0.5	1.05 0.5 3	1.05 5 200	1.1 3 5	0.2	798	8	350000
M4	Ratio Start Size End size	1.05 0.1 0.5	1.05 0.5 2	1.05 5 200	1.1 2 5	0.1	1595	12	840000
M5	Ratio Start Size End size	1.05 0.05 0.5	1.05 0.5 2	1.05 5 200	1.1 2 5	0.05	3190	26	1500000

The torque and power coefficients (C_p and C_m) of the VAWT were tested by using five different types of mesh when the TSR was 1.2, with wind speed $U_\infty = 4.5 \text{ m/s}$. Figure 3.32 shows the C_m generation versus the azimuth angle at TSR=1.2 in different types of meshes.

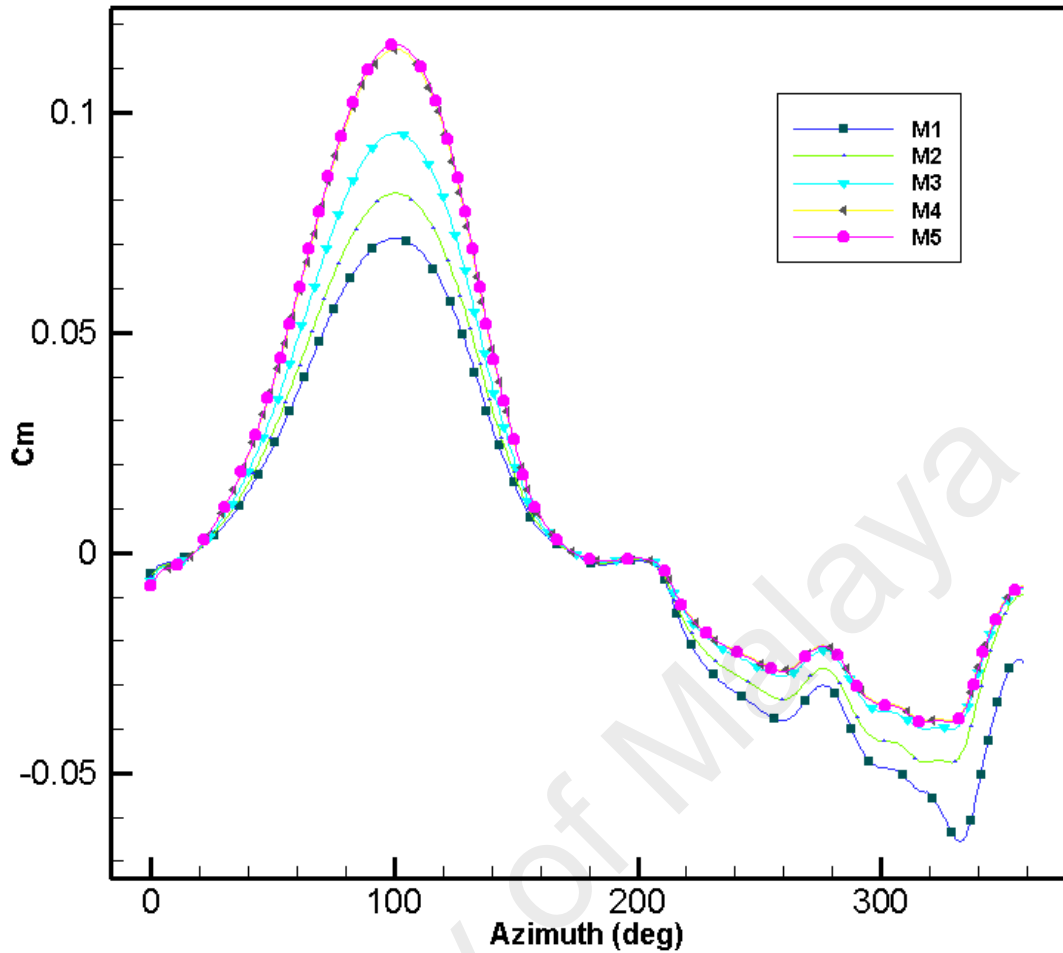


Figure 3.32: Mesh dependency test in TSR=1.2.

As seen from Figure 3.32, M4 and M5 have almost similar results. However, increasing the number of cells led to a significant difference in the C_m between M1 and M3. It can clearly be observed that the maximum generation of energy are in $\theta = 90^\circ$ to $\theta = 100^\circ$ and the negative value for C_m was reported for all cases when the blade was between $\theta = 200^\circ$ and $\theta = 360^\circ$. Figure 3.33, shows the variation of the power coefficient for different types of mesh in TSR= 1.2.

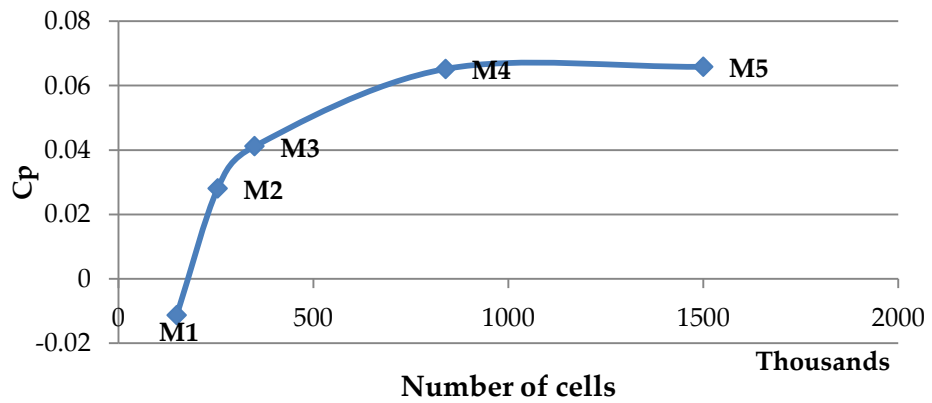


Figure 3.33: Variation of the C_p in different types of mesh in $TSR=1.2$

In addition, Figure 3.33 shows M4 and M5 generating the maximum C_p . Moreover, the difference of the C_p is small in these two meshes. Therefore, the M4 results show the most appropriate results.

3.4.9 Time dependency study

Sufficient temporal resolution is necessary to ensure a proper unsteady simulation of the VAWT. Based on a previous research by Qin et al. (Qin et al., 2011), the convergence of the CFD simulation depends on choosing the right time step (Δt). Therefore, three different time steps based on the rotational speed of the VAWT were examined to achieve a good and reliable result. The largest time step was equal to $2^\circ\omega^{-1}$ (the time equivalent to two degrees of one revolution) which is equal to 180 steps per one rotation. While the second time step was half of the first one ($\Delta t=1^\circ\omega^{-1}$ which means 360 steps per one rotation), and the third one is ($\Delta t=0.5^\circ\omega^{-1}$ which represents 720 step per one rotation) when the TSR was 1.2. Figure 3.34 shows the time dependency which was employed in this study.

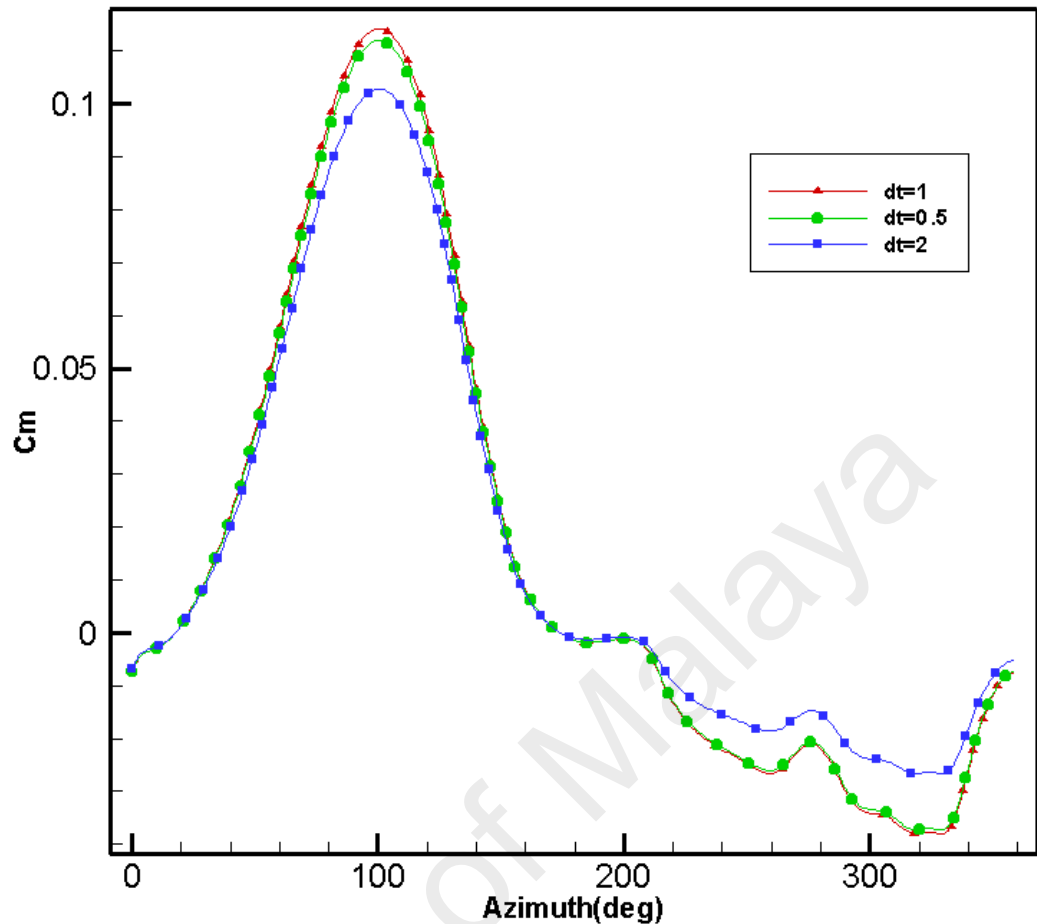


Figure 3.34: Time dependency study.

As shown in Figure 3.34, there is a very small difference in the results of the C_m in the case of $dt = 1^\circ\omega^{-1}$ and $0.5^\circ\omega^{-1}$. Hence, $dt=1^\circ\omega^{-1}$ was selected for the successive numerical simulations in order to reduce the computational time to a minimum.

3.4.10 Turbulence Modelling and Dynamic Stall

Wilcox (1998) proposed the following definition of turbulence: “Turbulence is an irregular motion which, in general, makes its appearance in fluids, gaseous or liquid, when they flow past solid surfaces, or even when neighboring streams of the same fluid flow pass or over one another.” Turbulence is an inherently three dimensional and time dependent problem. Therefore, an enormous amount of information is necessary to completely describe a turbulent flow. In most cases, what an engineer requires is the

prediction of the physically meaningful properties of the flow, not the complete time history of every flow property over all spatial coordinates.

Turbulence consists of random fluctuations of the various flow properties. Hence, a statistical approach to solving it is deemed appropriate. A procedure introduced by Reynolds in 1895 best serves this purpose, where all quantities are expressed as the sum of the mean and fluctuating parts. Then the time average of the continuity and the Navier–Stokes equations are formed. The nonlinearity of the Navier–Stokes equations introduces unknown stresses throughout the flow. Derived equations for the stresses result in additional unknown quantities, which require closure equations, termed as turbulence models.

In this thesis, the problem is well within the incompressible region. The equations for conservation of mass and momentum for incompressible flow are as follow (Schlichting & Gersten, 2003):

$$\frac{\partial u_i}{\partial x_i} = 0 \quad (3.17)$$

$$\rho \frac{\partial u_i}{\partial t} + \rho u_j \frac{\partial u_i}{\partial x_j} = -\frac{\partial P}{\partial x_i} + \frac{\partial t_{ji}}{\partial x_j} \quad (3.18)$$

Where u_i is velocity, x_i is position, t is time, p is pressure, ρ is density and t_{ij} is the viscous stress tensor defined by:

$$t_{ij} = 2\mu s_{ij} \quad (3.19)$$

Where μ is the molecular viscosity and s_{ij} is the strain–rate tensor,

$$s_{ij} = \frac{1}{2} \left(\frac{\partial u_i}{\partial x_j} + \frac{\partial u_j}{\partial x_i} \right) \quad (3.20)$$

Rewriting and simplifying the previous equations yield the Navier–Stokes equation in conservation form.

$$\rho \frac{\partial u_i}{\partial t} + \rho \frac{\partial}{\partial x_i} (u_i u_j) = -\frac{\partial P}{\partial x_i} + \frac{\partial}{\partial x_j} (2\mu s_{ij}) \quad (3.21)$$

Time averaging Eq. 3.17 and 3.21 yields the Reynolds Averaged equations of motion in conservation form,

$$\frac{\partial U_i}{\partial x_i} = 0 \quad (3.22)$$

$$\rho \frac{\partial U_i}{\partial t} + \rho \frac{\partial}{\partial x_j} (U_j U_i + \overline{u'_j u'_i}) = -\frac{\partial P}{\partial x_i} + \frac{\partial}{\partial x_j} (2\mu S_{ji}) \quad (3.23)$$

Rewriting Eq. 3.24 in its reverse yields its most recognizable form.

$$\rho \frac{\partial U_i}{\partial t} + \rho U_j \frac{\partial U_i}{\partial x_j} = -\frac{\partial P}{\partial x_i} + \frac{\partial}{\partial x_j} (2\mu S_{ji} - \overline{\rho u'_j u'_i}) \quad (3.24)$$

Equation 3.24 is usually referred to as the Reynolds-averaged Navier-Stokes equation, where the quantity $-\overline{\rho u'_j u'_i}$ is known as the Reynolds-stress tensor. The averaging process effectively introduces unknowns through the Reynolds-stress components without any additional equations. The closure problem of turbulence is essentially devising approximations for the unknown correlations in terms of flow properties that are known, so that a sufficient number of equations exist.

In CFD simulations of VAWTs, the selection of an appropriate turbulence model is not a simple process. A turbulence model is deemed appropriate if it is validated against experimental data. The accuracy of blade force predictions is a very important component of validation because it directly influences the prediction of the power coefficient of the modelled rotor.

Unfortunately, for a lot of VAWT research work, there is very little or no available experimental data to which the models can be compared. This has serious implications because researchers resort to extensive checks following recommended numerical guidelines but are never able to validate the model as physically correct. The problem is exacerbated by the simplification of the VAWT into a two-dimensional CFD

model without adequate explanation of the limitations of the model and acceptable rationalization of the differences between CFD results and experiments.

Three different RANS turbulence models are analyzed, namely the standard $k-\omega$, the standard $k-\varepsilon$ and $k-\omega$ SST model. These three turbulence models are classified as two-equation turbulence models, as they include two extra transport equations to represent the turbulent properties of the flow. One variable determines the energy in the turbulence, while the other variable is considered the scale of the turbulence.

The exact $k-\varepsilon$ equations contain many unknown and unmeasurable terms. For a much more practical approach, the standard $k-\varepsilon$ turbulence model (Launder & Spalding, 1974) was used which is based on our best understanding of the relevant processes, thus minimizing unknowns and presenting a set of equations which can be applied to a large number of turbulent applications.

For turbulent kinetic energy k (Versteeg & Malalasekera, 2007):

$$\frac{\partial(\rho k)}{\partial t} + \frac{\partial(\rho k u_i)}{\partial x_i} = \frac{\partial}{\partial x_j} \left[\frac{\mu_t}{\sigma_k} \frac{\partial k}{\partial x_j} \right] + 2\mu_t E_{ij} E_{ij} - \rho \varepsilon \quad (3.25)$$

For dissipation ε (Versteeg & Malalasekera, 2007):

$$\frac{\partial(\rho \varepsilon)}{\partial t} + \frac{\partial(\rho \varepsilon u_i)}{\partial x_i} = \frac{\partial}{\partial x_j} \left[\frac{\mu_t}{\sigma_\varepsilon} \frac{\partial \varepsilon}{\partial x_j} \right] + C_{1\varepsilon} \frac{\varepsilon}{k} 2\mu_t E_{ij} E_{ij} - C_{2\varepsilon} \rho \frac{\varepsilon^2}{k} \quad (3.26)$$

In other words, the rate of change of k or ε + Transport of k or ε by convection = Transport of k or ε by diffusion + Rate of production of k or ε - Rate of destruction of k or ε .

Where:

u_i represents velocity component in corresponding direction

E_{ij} represents component of rate of deformation

μ_t represents eddy viscosity

$$\mu_t = \rho C_\mu \frac{k^2}{\varepsilon} \quad (3.27)$$

The equations also consist of some adjustable $\sigma_k, \sigma_\varepsilon, C_{1\varepsilon}, C_{2\varepsilon}$. The values of these constants have been arrived at by numerous iterations of data fitting for a wide range of turbulent flows (Versteeg & Malalasekera, 2007):

$$C_\mu = 0.09, \sigma_k = 1, \sigma_\varepsilon = 1.3, C_{1\varepsilon} = 1.44 \text{ and } C_{2\varepsilon} = 1.92$$

In $k-\omega$ governing equations are (Wilcox, 1988):

Kinematic Eddy Viscosity:

$$\nu_T = \frac{k}{\omega} \quad (3.28)$$

Turbulence Kinetic Energy:

$$\frac{\partial k}{\partial t} + U_j \frac{\partial k}{\partial x_j} = \tau_{ij} \frac{\partial U_i}{\partial x_j} - \beta^* k \omega + \frac{\partial}{\partial x_j} \left[(\nu + \sigma^* \nu_T) \frac{\partial k}{\partial x_j} \right] \quad (3.29)$$

Specific Dissipation Rate:

$$\frac{\partial \omega}{\partial t} + U_j \frac{\partial \omega}{\partial x_j} = \alpha \frac{\omega}{k} \tau_{ij} \frac{\partial U_i}{\partial x_j} - \beta \omega^2 + \frac{\partial}{\partial x_j} \left[(\nu + \sigma \nu_T) \frac{\partial \omega}{\partial x_j} \right] \quad (3.30)$$

Closure Coefficients and Auxilary Relations:

$$\alpha = \frac{5}{9}, \beta = \frac{3}{40}, \beta^* = \frac{9}{100}, \sigma = \frac{1}{2}, \sigma^* = \frac{1}{2}$$

3.4.10.1 $k-\varepsilon$ vs. $k-\omega$ Turbulence modeling

The $k-\varepsilon$ was used in a fully turbulent flow (high Reynolds number). It cannot handle a low Re and the flow separation. The reason why it is used so widely because of the low computaion time and resource requirement in the industries. Based previous litratures, the several reasons for the $k-\varepsilon$ model to become popular in comparision to other eddy viscosity model are:

1- It is mainly devised for high-Re fully developed turbulent flow as such a flow is manifested in the majority of engineering problems.

2- Literature records are crowded with thousands of successful CFD calculations in nearly all industrial and engineering problems using the $k-\varepsilon$ model.

Therefore, fluid dynamicists always “give it a try” with the $k-\varepsilon$ when they tackle a problem for the first time.

3- It converges easily in most commercial FV codes, even with higher order numerical schemes.

4- There are several variants for the $k-\varepsilon$ model, which are fine-tuned and corrected for specific engineering problems. Shih’s reliable $k-\varepsilon$, Richardson number corrected $k-\varepsilon$ are popular examples.

$k-\omega$ is majorly used for near wall problems. Moving away from the wall $k-\omega$ turns out to be same as $k-\varepsilon$. Hence, for the complex boundary layer problems or transition flow, $k-\omega$ works better with fine resolution in mesh at the walls.

The SST $k-\omega$ turbulence model (Menter, 1993) is a two-equation eddy-viscosity model which has become very popular. The shear stress transport (SST) formulation combines the best of two worlds. The use of a $k-\omega$ formulation in the inner parts of the boundary layer makes the model directly usable all the way down to the wall through the viscous sub-layer. Hence, the SST $k-\omega$ model can be used as a Low-Re turbulence model without any extra damping functions. The SST formulation also switches to a $k-\varepsilon$ behaviour in the free-stream and thereby avoids the common $k-\omega$ problem where the model is too sensitive to the inlet free-stream turbulence properties. Authors who use the SST $k-\omega$ model often merit it for its good behaviour in adverse pressure gradients and separating flow. The SST $k-\omega$ model does produce an overly large turbulence levels in regions with a large normal strain like stagnation regions and regions with strong

acceleration. This tendency is much less pronounced than with a normal k-ε model though.

Kinematic Eddy Viscosity:

$$v_T = \frac{\alpha_1 k}{\max(\alpha_1 \omega, SF_2)} \quad (3.31)$$

Turbulence Kinetic Energy:

$$\frac{\partial k}{\partial t} + U_j \frac{\partial k}{\partial x_j} = P_k - \beta^* k \omega + \frac{\partial}{\partial x_j} \left[(v + \sigma_k v_T) \frac{\partial k}{\partial x_j} \right] \quad (3.32)$$

Specific Dissipation Rate:

$$\frac{\partial \omega}{\partial t} + U_j \frac{\partial \omega}{\partial x_j} = \alpha S^2 - \beta \omega^2 + \frac{\partial}{\partial x_j} \left[(v + \sigma_\omega v_T) \frac{\partial \omega}{\partial x_j} \right] + 2(1 - F_1) \sigma_{\omega 2} \frac{1}{\omega} \frac{\partial k}{\partial x_i} \frac{\partial \omega}{\partial x_i} \quad (3.33)$$

Closure Coefficients and Auxiliary Relations:

$$P_k = \min(\tau_{ij} \frac{\partial U_i}{\partial x_j}, 10\beta^* k \omega) \quad (3.10)$$

$$F1 = \tanh \left\{ \left[\min \left[\max \left(\frac{\sqrt{k}}{\beta^* \omega y}, \frac{500\nu}{y^2 \omega} \right), \frac{4\sigma\omega 2k}{CD_{k\omega} y^2} \right] \right]^4 \right\} \quad (3.34)$$

$$F2 = \tanh \left[\left[\max \left(\frac{2\sqrt{k}}{\beta^* \omega y}, \frac{500\nu}{y^2 \omega} \right) \right]^2 \right] \quad (3.35)$$

$$CD_{k\omega} = \max(2\rho\sigma_{\omega 2} \frac{1}{\omega} \frac{\partial k}{\partial x_i} \frac{\partial \omega}{\partial x_i}, 10^{-10}) \quad (3.36)$$

$$\alpha_1 = \frac{5}{9}, \beta^* = \frac{9}{100}, \sigma_{k1} = 0.85, \sigma_{k2} = 1, \sigma_{\omega 1} = 0.5, \sigma_{\omega 2} = 0.856$$

And S is source term.

All simulations in this part were done with the time step equalling to $1^\circ \omega^{-1}$ at TSR=1.2. Figure 3.35 shows the obtained torque coefficient of the VAWT using different turbulence models.

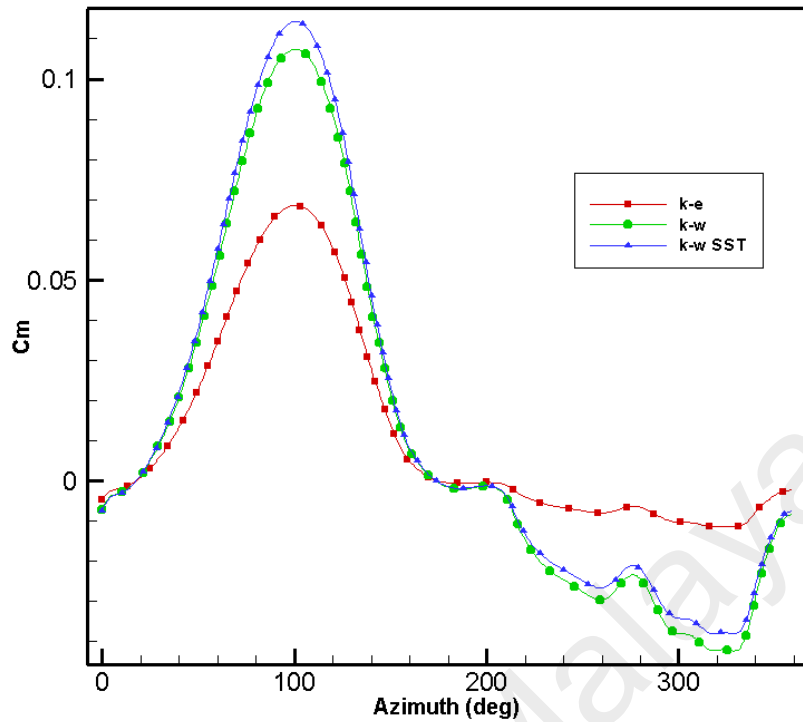


Figure 3.35: Prediction of the C_m using different turbulence models.

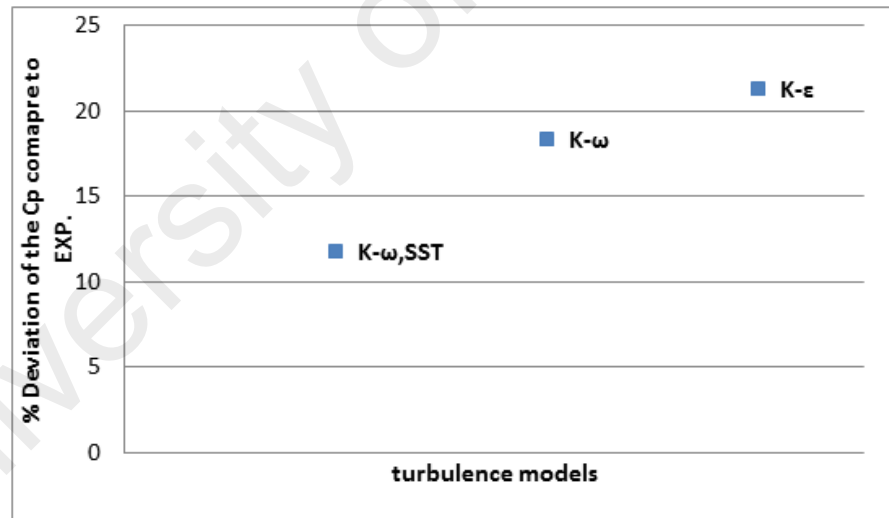


Figure 3.36: Deviation of the C_p results from experiments in different turbulence models.

As it can be seen, there are very small dissimilarities in the downstream flow between the $k-\omega$ and $k-\omega$ SST, and the same results can be observed in the upstream area for both models. The standard $k-\epsilon$ models do not provide good results for the upstream flow when compared to the $k-\omega$ SST model as it can be seen in

Figure 3.36. By using the $k - \varepsilon$ model, results show the 21% differences in predicted C_p compared to the experimental data. However, the best results were achieved by using the $k - \omega$ SST with the lowest deviation of the experiments by 11%. A similar outcome was obtained in other related literatures such as (W. Chong et al., 2013; W. T. Chong et al., 2013; Mohamed, 2012; Rosario Nobile, Vahdati, Barlow, & Mewburn-Crook, 2014).

3.4.11 CFD Validation

The numerical study was validated by the experimental data to verify the accuracy of the CFD results. For this purpose, the CFD simulation was compared with wind tunnel testing which was conducted at the Aeronautics Laboratory in University Technology Malaysia by Chong et al. (2013). Figure 3.37 indicates the configuration of the testing unit in this wind tunnel.

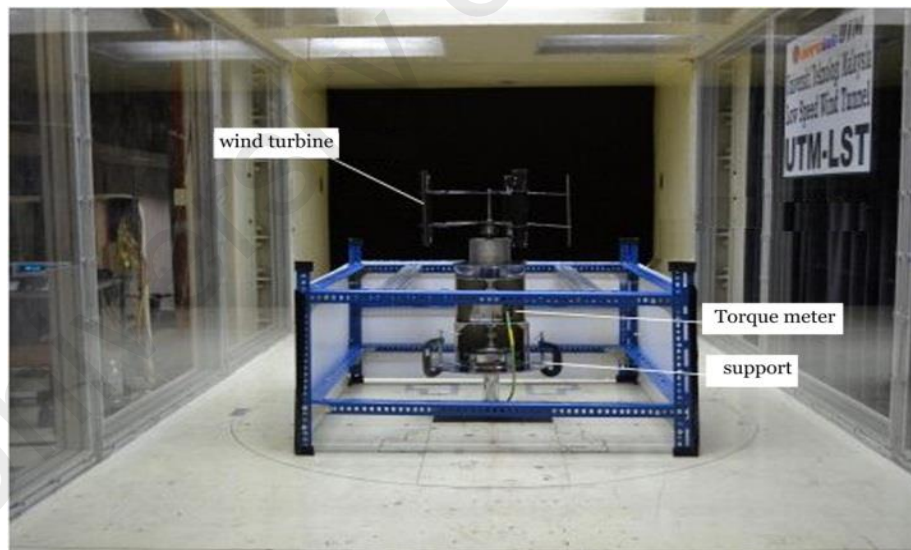


Figure 3.37: Configuration of the testing unit in wind tunnel.

As shown in Figure 3.37, wind tunnel testing was conducted for a turbine consisting of five blades with a section profile of FX63-137. For this test, the blade chord length was designed at 78mm in a H-rotor wind turbine, with a 500mm rotor diameter and a height of 350mm. An identical wind speed, i.e. 4.5 m/s was used in the

following experiment to compare the rotational speed (RPM) and power generated by the wind turbine. The rotational speed, torque and power generation were measured via a transducer, which was connected in-line with the rotor shaft of the wind turbine. The load was applied on the rotor shaft by adjusting the hysteresis brake. The maximum torque experienced by the rotor at the particular wind speed was recorded when the highest load was applied on the rotor in which RPM is stabilized (can maintain the rotor RPM). Two types of bearings were employed in the rotor shaft connection and fitting including a tapered roller bearing and a deep groove ball. The experimental results of wind tunnel testing was compared with CFD simulation results as shown below.

3.4.11.1 Power Coefficient

The first aspect of the model validation is the comparison of the predicted VAWT performance over a wide range of operating speeds. Both, the fully turbulent $k-\omega$ SST and the Transition SST models were tested against the experimentally derived C_p . The steady wind speed chosen was 4.5m/s and the simulations were run at different tip speed ratios from $TSR = 0.8$ up to $TSR = 1.6$. It can be seen from Figure 3.38 that both 2D models over-predict the C_p starting from $TSR = 0.8$, all the way up to $TSR = 1.6$.

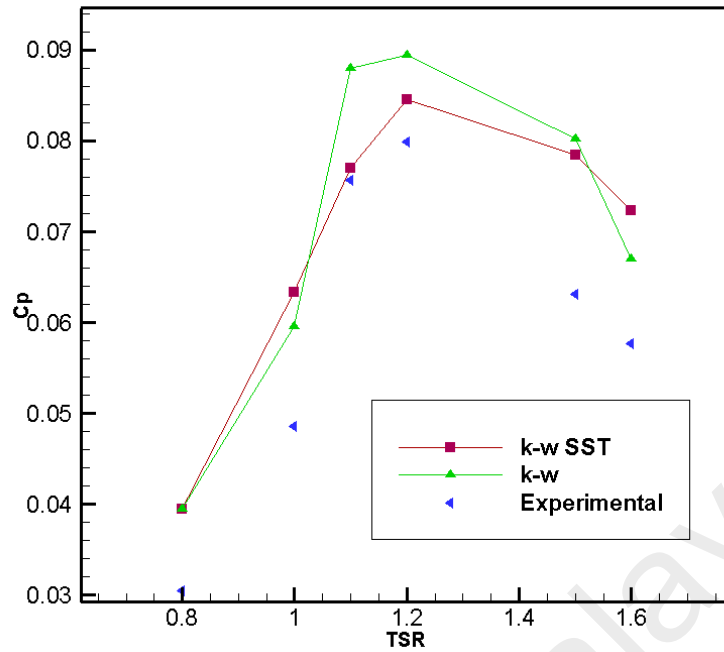
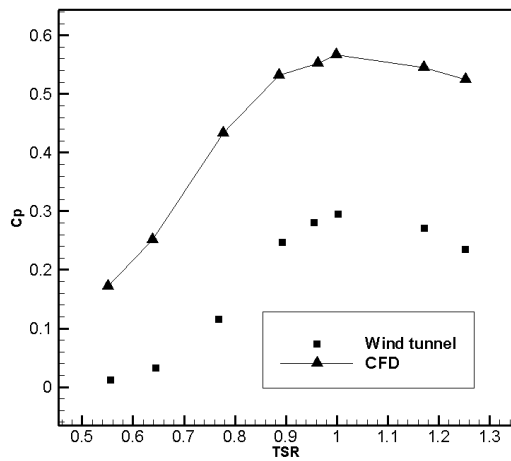


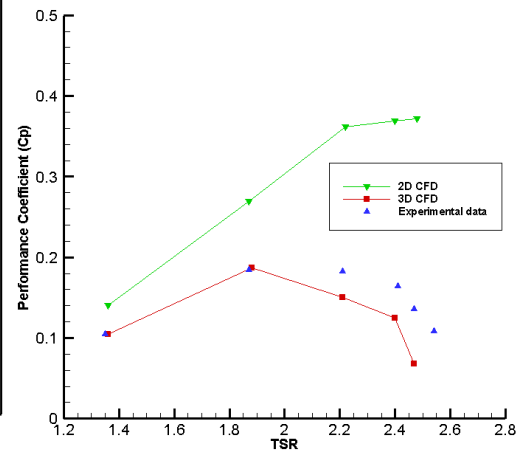
Figure 3.38: Results of the coefficient of the power in wind tunnel experimental test data compared to the CFD simulation.

Maximum C_p for the fully turbulent model was 0.088 at $TSR = 1.1$ while the Transition SST model predicted maximum $C_p = 0.084$ at $TSR = 1.2$. The maximum C_p for the fully turbulent model occurs at the same TSR as that of the experiments.

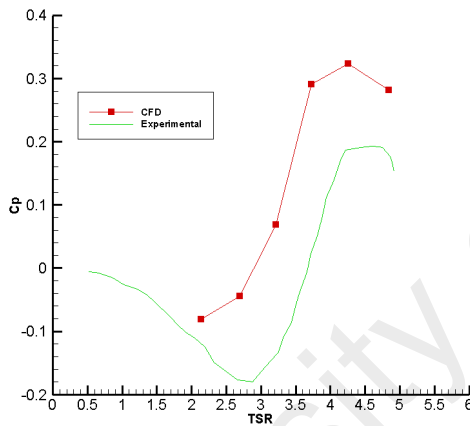
There is a gap in the predicted C_p 's between the two CFD models from $TSR=1.15$ to $TSR=1.5$ where the fully turbulent model over-predicts the C_p much more than the Transition SST model. Higher TSR 's show the greatest over-prediction of the CFD models from experiments. This may be due to the effects of the finite blade span where there is a reduction in aspect ratio as seen by McIntosh et al. (2012), causing a substantial drop in C_p at a high TSR versus the small drop in C_p at a low TSR .



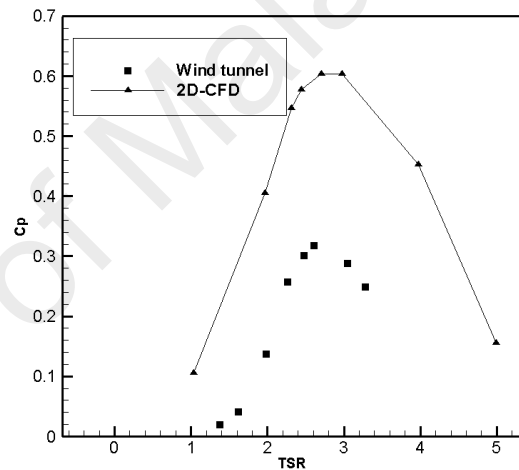
a). Castell et al. (2010).



b). Howell et al (2010).



c).Edwards et al. (2007).



d). Nobile et al. (2014).

Figure 3.39: Published results from other studies showing the difference between 2D and 3D data.

The gap in the predicted C_p was expected since the 2D model does not account for the finite blade span as well as for the blade–support arm junction effects and support arm drag that are present in the actual setup. The results are consistent to the published data by Raciti Castell et al (Castelli et al., 2010; Raciti Castell, Dal Monte, Quaresimin, & Benini, 2013), Howell et al (Howell et al., 2010) and Edwards et al (J. Edwards et al., 2007) and Nobile et al (Rosario Nobile et al., 2014) where a 2D C_p was over–predicted over the entire range of TSR. Raciti Castell et al compared their 2D simulations to wind tunnel experiments (Figure 3.39a) and argued that the difference is

due to blockage effects that increase the flow velocities near the blades to much higher values than the unperturbed flow at the inlet. Howell et al showed an improved match between the 3D CFD and the experiments (Figure 3.39b). Edwards et al attributed the difference (Figure 3.39c) in predicted C_p to the finite blade span and blade–support arm junction effects. Overall, the general trend of the predicted C_p matches well with the experimental data.

3.5 SUMMARY

Based on the results obtained from force validation across a wide range of TSR, the Transition SST model was selected as the best model that most accurately captures the flow physics of the VAWT. The predicted positive performance of the Transition SST model is closer to the experiments values of C_p versus the $k-\omega$ SST model. All simulations conducted for the this study will use the Transition SST model.

CHAPTER 4: RESULTS AND DISCUSSION

This chapter details the numerical and experimental investigations on the performance of the open rotor VAWT and augmented VAWT. In the first step, the open rotor VAWT performance was initially analyzed over the TSR range of $0.8 \leq \text{TSR} \leq 1.6$. In the next step, performance of the VAWT was investigated with different configurations of the ODGV shapes in term of the angle of the ODGV as well as the outer diameter of the ODGV. Comparison of the optimum ODGV with convenient ODGV's was also carried out in this chapter. Finally, results of the lab test were compared with the CFD results to determine the accuracy of the numerical simulation.

4.1 THE PERFORMANCE OF THE TURBINE WITHOUT ODGV

The numerical model developed in Chapter 3 was the basis for all numerical studies carried out in this chapter. The performance of the VAWT was investigated and was validated against experimental data. In following section, the validation is in a closer inspection to give a better understanding of the behavior in VAWT performance across a wide operating range.

4.1.1 Power Coefficient

Important data for the understanding and optimized use of a wind turbine lies in the characteristic power curve (Armstrong, Fiedler, & Tullis, 2012; Iida, Mizuno, & Fukudome, 2004b; Trivellato & Raciti Castelli, 2014). Results of the Variation of C_p versus TSR, is presented in Figure 3.38 and is repeated in Figure 4.1. There is a marked difference between the predicted C_p and the actual C_p , especially in the power producing region ($1.2 < \text{TSR} < 1.6$). The maximum measured C_p is 0.075 at $\text{TSR} = 1.1$, while the maximum predicted C_p is 0.084 at $\text{TSR} = 1.2$. Shift of the power curve

upwards, to the right was explained by the effects of having infinite aspect ratio in the 2-D numerical model. A low AR, as is the case of the actual experimental VAWT, increases the induced drag due to tip effects in proportion to the positive performance of the blades (Simon Charles McIntosh, 2009) .

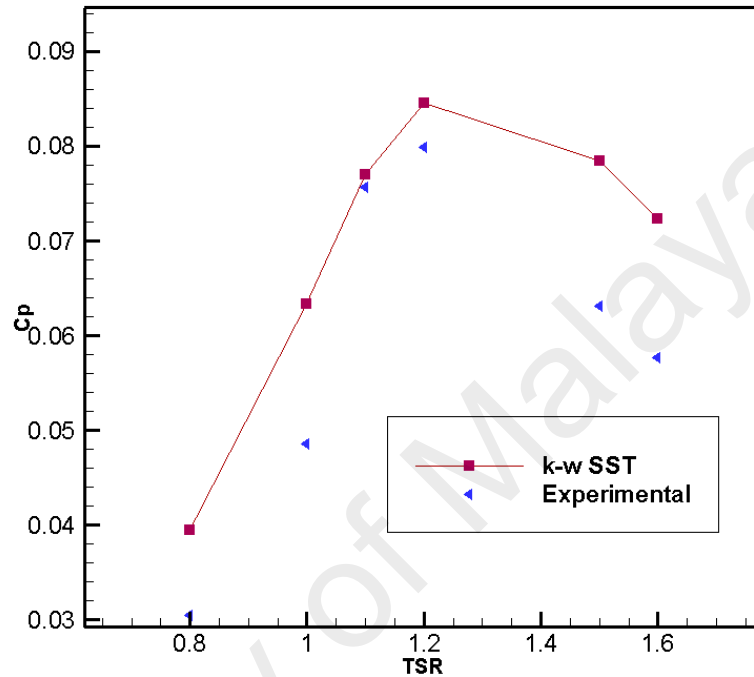


Figure 4.1: Performance of the bare VAWT.

Figure 4.2 shows the variation of the C_m on a single blade at different tip speed ratios during one rotation. These results have been achieved from the simulation of the open rotor (only VAWT) without using ODGV when the wind speed is as much as 4.5m/s. It is apparent from figure generation of the torque can be illustrated in two major sections. The first part stats from azimuth angle $\theta=0^\circ$ to $\theta=180^\circ$ and second part starts from $\theta=180^\circ$ to $\theta=360^\circ$. In the first part blade have positive torque generation and this torque is increases by increasing the TSR so the highest torque generation can be seen in TSR=1.6 in mentioned zone. After $\theta=180^\circ$, negative torque is appeared and this negative torque is in highest amount in TSR=1.6.

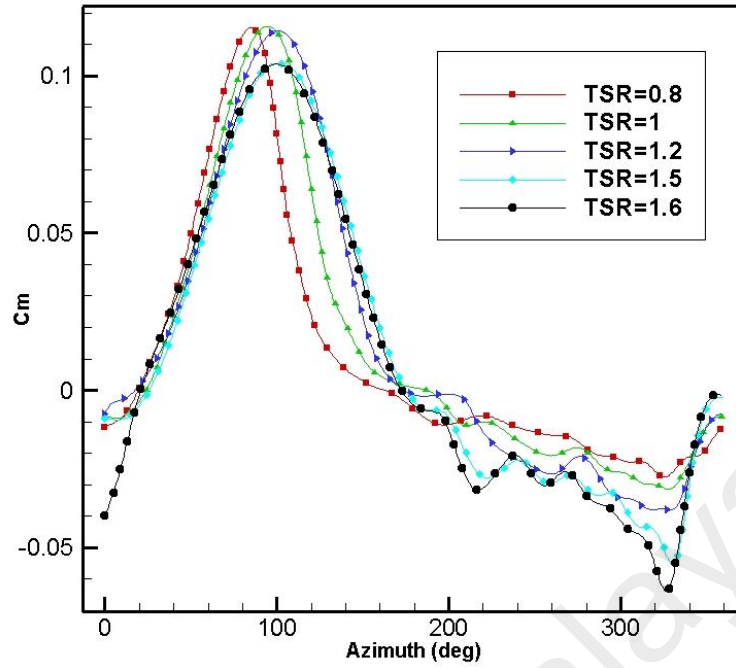


Figure 4.2: Torque coefficient variation at different TSR.

It can be seen from Figure 4.3, the maximum torque for the first blade was achieved at the azimuth angle $\theta = 101^\circ$. For the blades number two to number five, this peak torque generation are achieved at $\theta = 29^\circ, 317^\circ, 254^\circ, 173^\circ$ respectively. After the peak, the drag begins to increase as the blade enters into a dynamic stall, and the drag starts to be dominant until the azimuth angle is at $\theta = 110^\circ$. After $\theta = 200^\circ$, the negative torque was generated by the blade and the drag force is again dominant until up to $\theta = 19^\circ$.

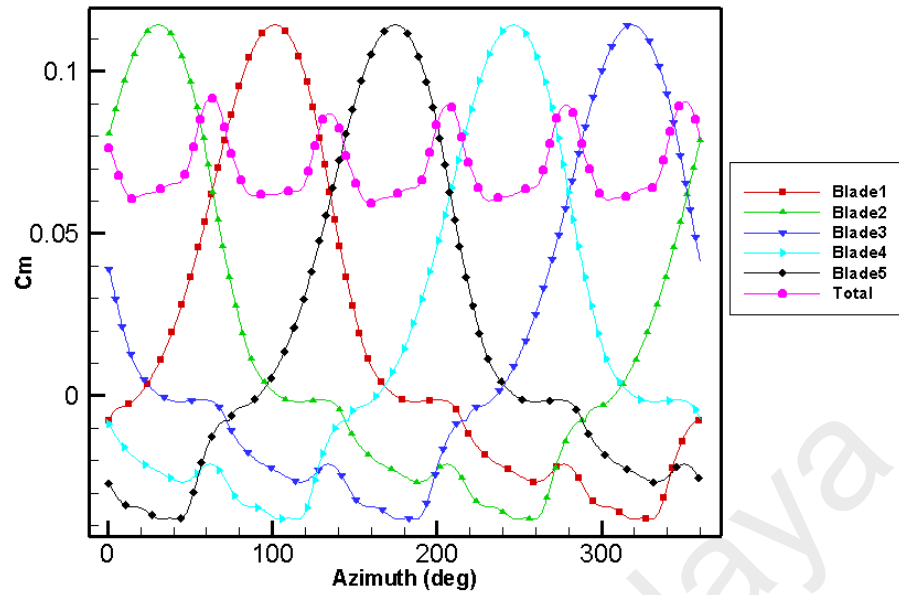


Figure 4.3: Predicted torque coefficient for five individual blades.

According to Figure 4.4, TSR and C_m are in a direct relationship when the TSR is between 0.8 and 1.2. However, TSR and C_m trends are opposite when for TSRs are greater than 1.2. The maximum value of the C_m is achieved when TSR is 1.2.

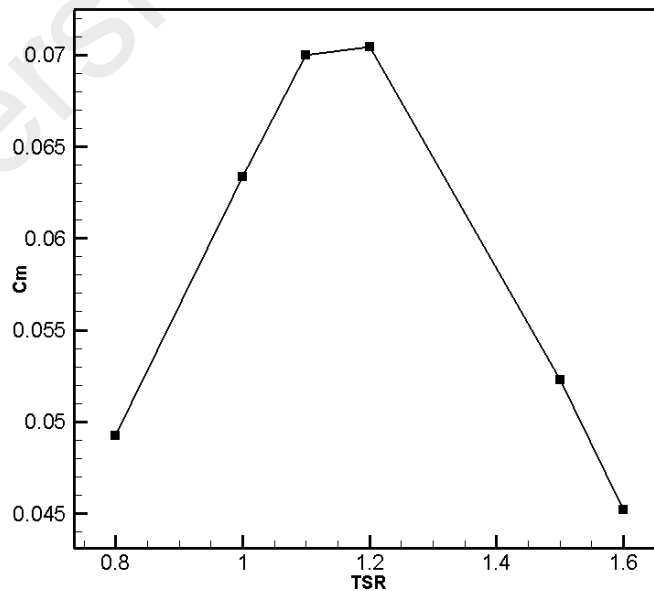


Figure 4.4: Average C_m for different TSRs

4.2 VISUALIZATION

4.2.1 Time-Averaged Flow Patterns

The time-averaged flow patterns are presented in Figure 4.5 and Figure 4.6. The vorticity contours (Figure 4.5) show that the range of vorticity magnitude as a function of tip-speed ratio was increased slightly while the TSR increased. The highest vorticity observed at $TSR = 1.6$. Figure 4.5 also shows a large-scale vortex located at the top side of blade three in $TSR = 0.8$. This vortex is demolished by the increase of TSR.

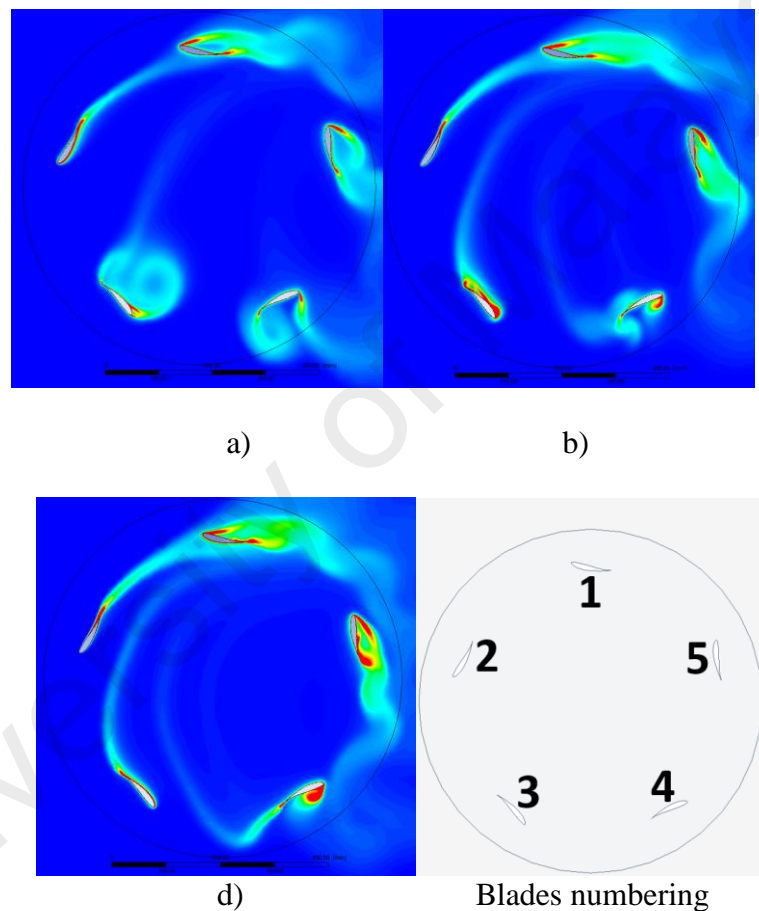


Figure 4.5: vorticity contours a) $TSR=0.8$, b) $TSR=1.2$, c) $TSR=1.6$.

4.2.2 Pressure Contours

Figure 4.6 presents the pressure distribution contour around an open VAWT at three different TSRs. There is a low-pressure zone on top of blade three that was created when the operation TSR is 0.8. By increasing the rotational speed, this low-pressure

zone moved to the leading edge of blade three. A high-pressure zone can also be reported at all three TSRs while the azimuth angles are between 60° and 100° . This zone makes a peak torque on the VAWT. A negative torque generation can be illustrated at high TSRs during the azimuth angle at between 280° and 340° by the help of the pressure contour. As it can be seen in the azimuth angle equal to 288° , a very low-pressure zone takes shape around blade number five.

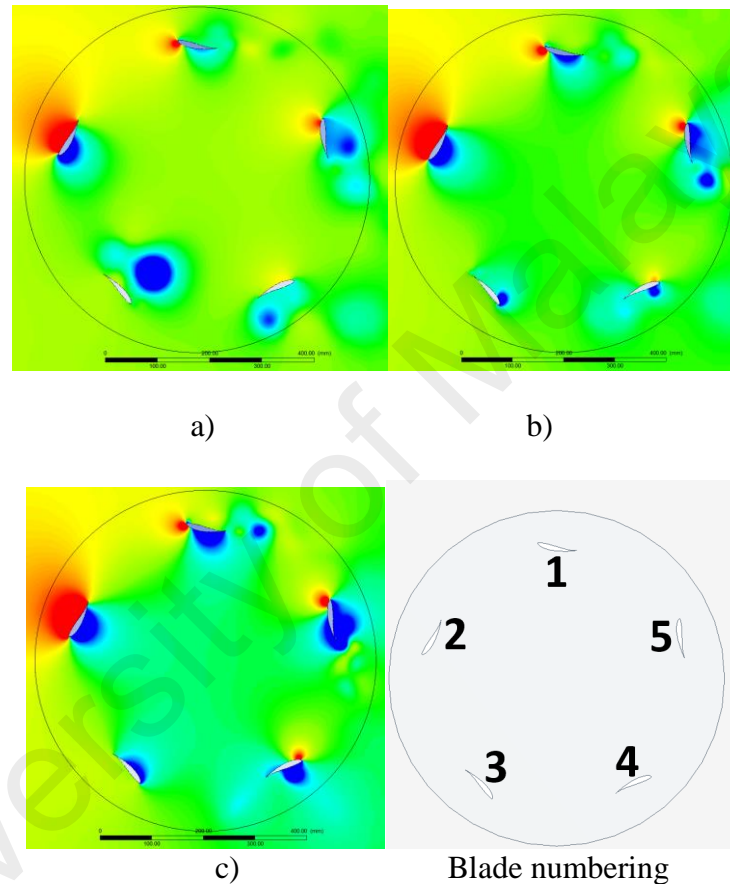


Figure 4.6: pressure contours a) TSR=0.8, b) TSR=1.2, c) TSR=1.6.

4.3 INFLUENCE OF THE ODGV ANGLES

The aim of this part of study is to present the effects of different Omni-direction-guide-vane (ODGV) angles on the performance of the VAWT. For this purpose, 52 design points have been considered to find the best guide vane position to achieve the highest performance of the VAWT. Table 4.1 shows the position and design points of the different ODGV angles. Positions of the angles of the ODGV are presented at

Figure 3.23. As it can be seen, β varies between -20° to 50° and α starts from -20° to 60° . Surface respond methodology in Design Expert 10 software was coupled with the CFD simulation to find out the relation between the two factors α and β with the performance of the VAWT.

Table 4.1: Design points of the different angle of the ODGV.

design point	β	α												
DP1	-20	-20	DP12	-10	0	DP23	0	30	DP34	10	60	DP45	30	60
DP2	-20	-10	DP13	-10	10	DP24	0	40	DP35	20	20	DP46	40	40
DP3	-20	0	DP14	-10	20	DP25	0	50	DP36	20	30	DP47	40	50
DP4	-20	10	DP15	-10	30	DP26	0	55	DP37	20	40	DP48	40	55
DP5	-20	20	DP16	-10	40	DP27	0	60	DP38	20	50	DP49	40	60
DP6	-20	30	DP17	-10	50	DP28	10	10	DP39	20	55	DP50	50	50
DP7	-20	40	DP18	-10	55	DP29	10	20	DP40	20	60	DP51	50	55
DP8	-20	50	DP19	-10	60	DP30	10	30	DP41	30	30	DP52	50	60
DP9	-20	55	DP20	0	0	DP31	10	40	DP42	30	40			
DP10	-20	60	DP21	0	10	DP32	10	50	DP43	30	50			
DP11	-10	-10	DP22	0	20	DP33	10	55	DP44	30	55			

4.4 RESPOND SURFACE METHODOLOGY RESULTS

The ANOVA statistic model shows that the model is significant by the F-value of 379.11. The significant model terms are those with 'Prob. > F' value of less than 0.05 where it implies that the model is significant. Factor B (β) was considered as the more significant factor compared to the factor A (α) with the F value equal to 10.49. The Predicted R-Squared signifies how well the model predicts the response values, and in this case, a value of 0.9735 is certainly desirable. To examine the conformity between the predicted R-Squared and Adjusted R-Squared, the difference between them must be

approximately less than 0.2 (Razavykia, Farahany, & Yusof, 2015), which in this case they are in reasonable agreement with each other by a difference of 0.0175. A desirable ratio for Adequate Precision that shows signal to noise ratio is greater than four which at this study is 62.55.

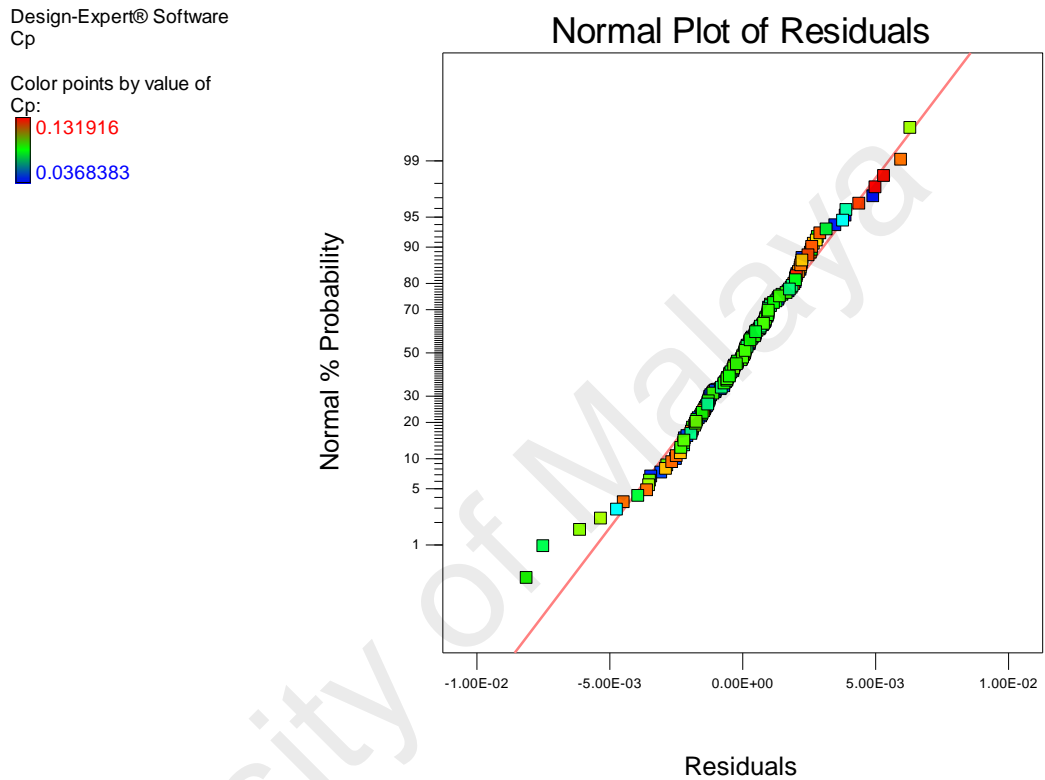


Figure 4.7: Normal probability plot of residuals in angle optimization.

Figure 4.7 shows the normal probability plot of residuals where most of the data lie along a straight line. This indicates that the errors are distributed normally, and the term significant is only specified in the model.

Design-Expert® Software
Cp

Color points by value of
Cp:
0.131916
0.0368383

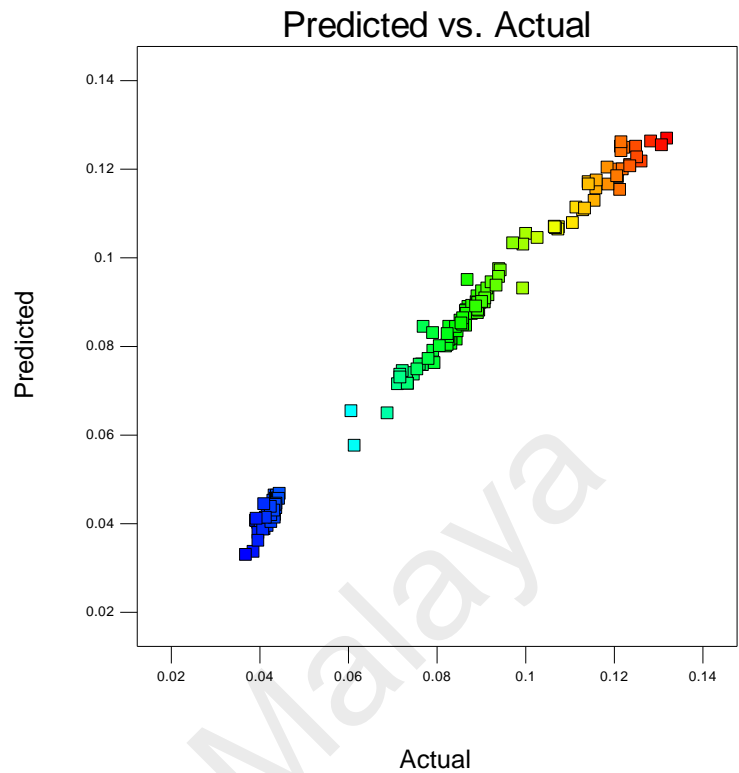


Figure 4.8: Predicted model Vs. actual results in angle optimization.

Figure 4.8 displays the observed values, which were compared with the predicted values from the model. It can be seen that the regression model is well fitted with the observed values.

Design-Expert® Software
Cp

Color points by value of
Cp:
0.131916
0.0368383

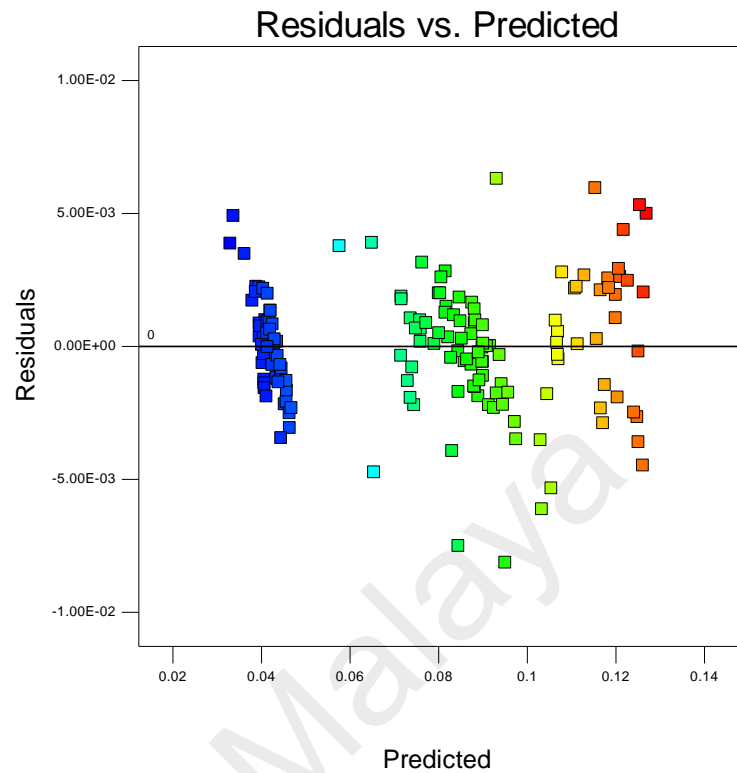


Figure 4.9: Residuals versus predicted for C_p in internally studentized for angle optimization.

Figure 4.9 shows the residual versus the predicted plot for C_p . It can be observed that there is no clear pattern on the data plot, and the data is randomly scattered.

Design-Expert® Software
Cp

Color points by value of
Cp:
0.131916
0.0368383

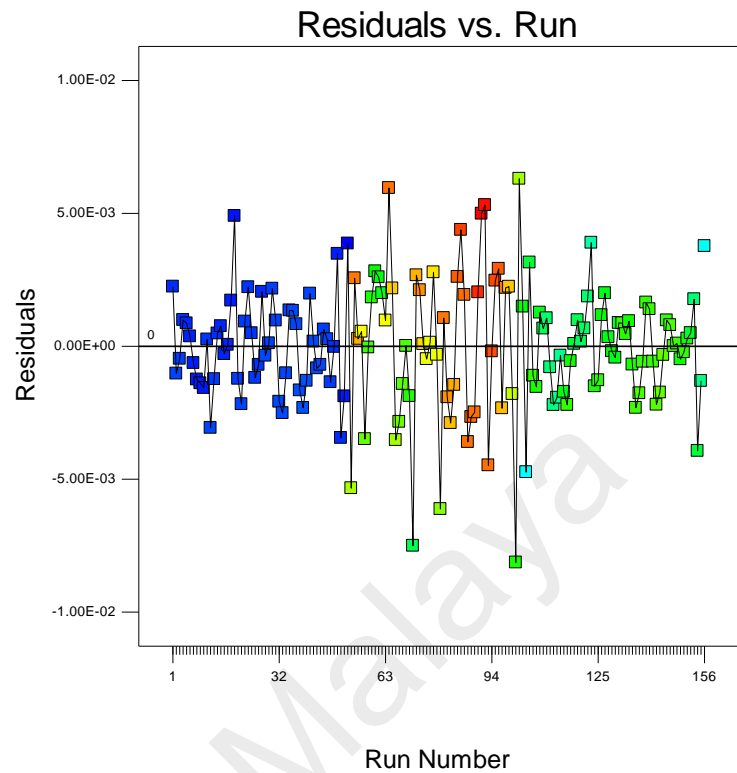


Figure 4.10: Predicted versus runs for C_p for angle optimization.

Internally studentized residuals were plotted against the run for the model of C_p in different ODGV angles shown in Figure 4.10. Residuals were calculated as the difference between the measured and predicted values, while internally studentized residuals were calculated as the ratio of the residual to the estimated standard deviation of the residual. From the plot, it can be stated that the model could be used to predict the response since all the studentized residuals for regression model of surface roughness lie within the limits (± 3 sigma) without any outliers.

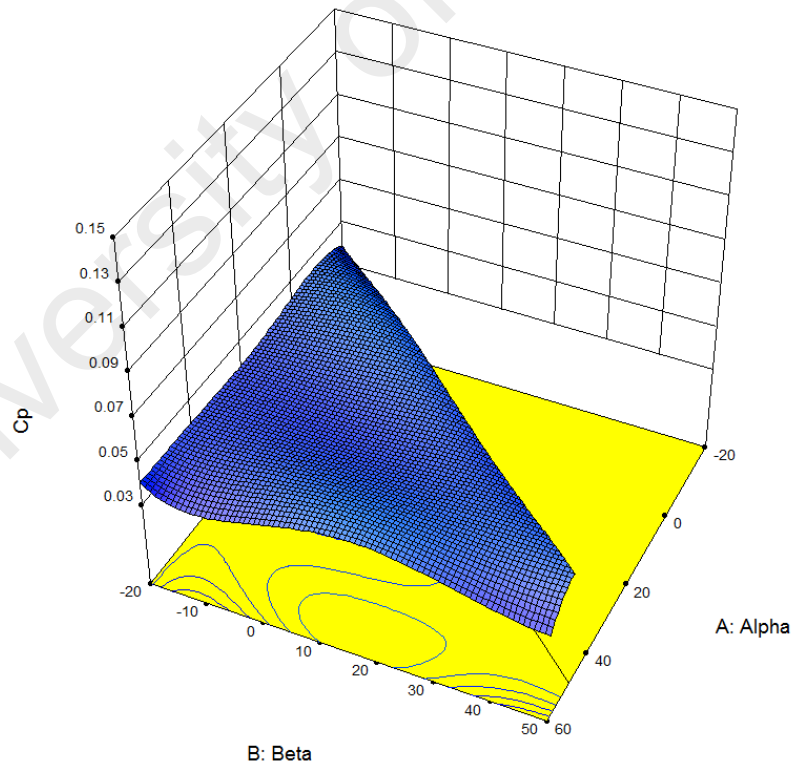
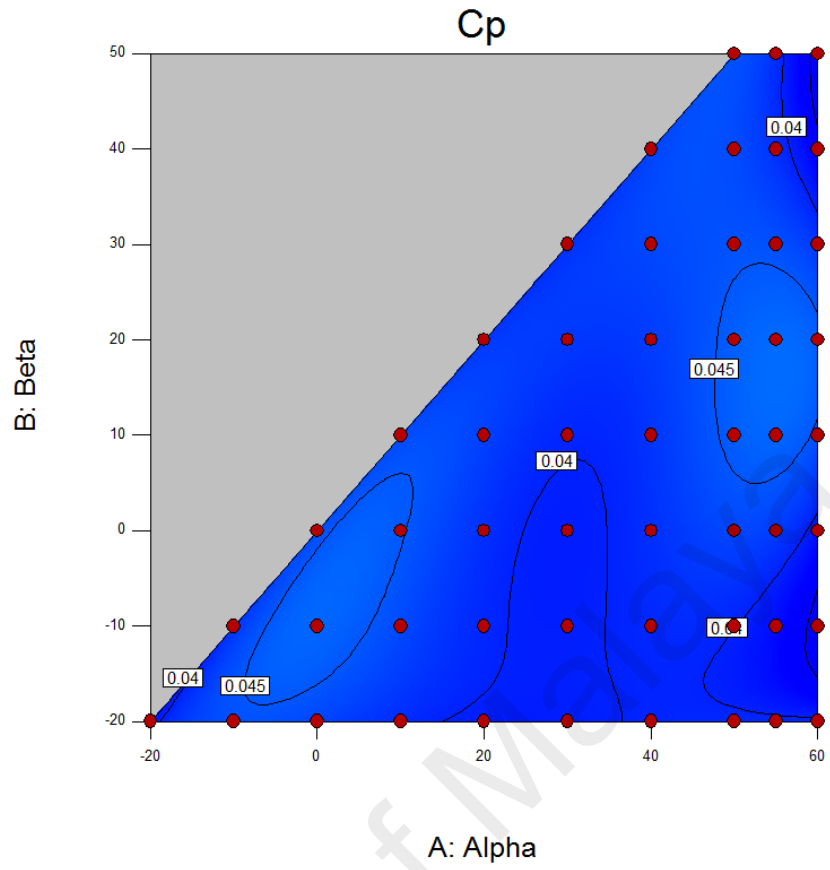


Figure 4.11: Influence of the angles on the VAWT C_p at $TSR=0.8$.

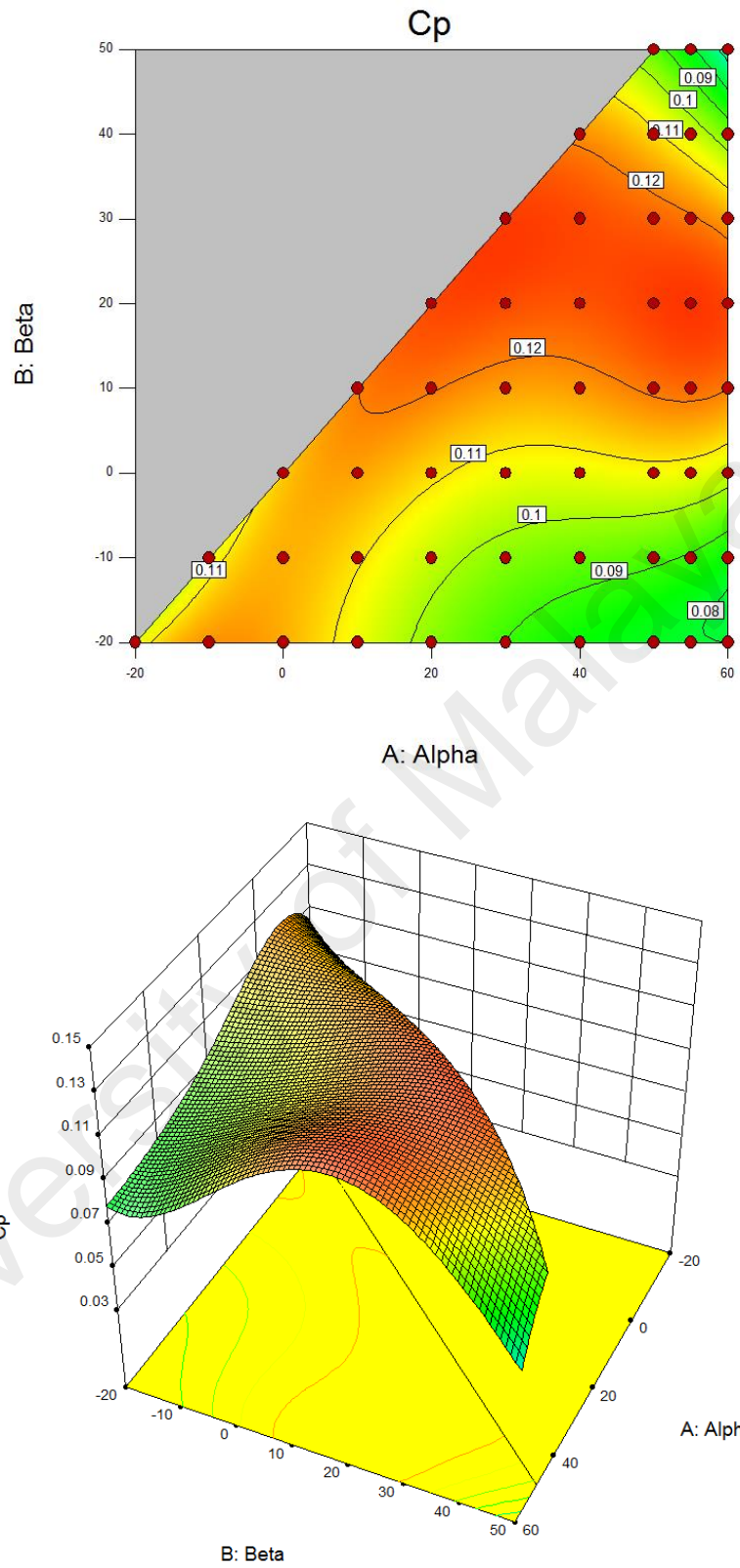


Figure 4.12: Influence of the angles on the VAWT C_p at $TSR=1.2$.

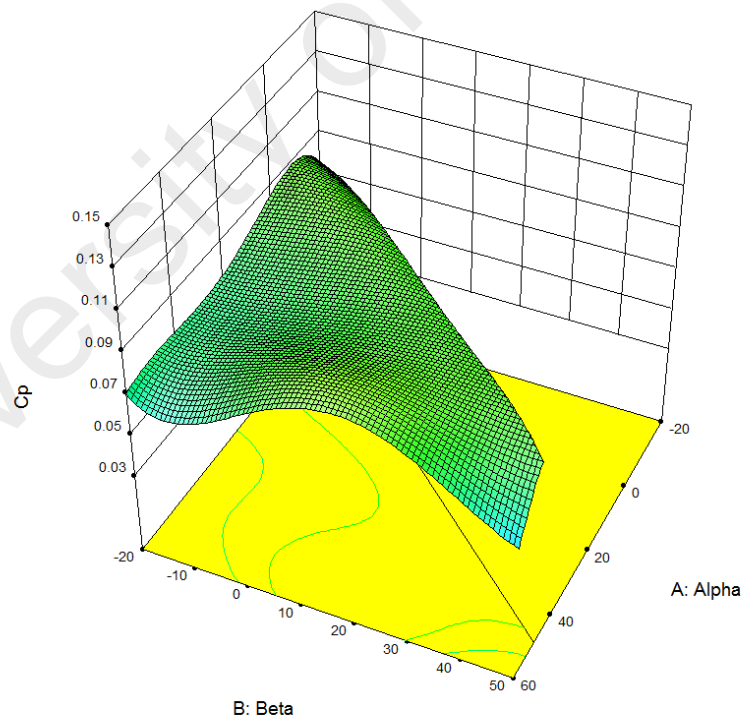
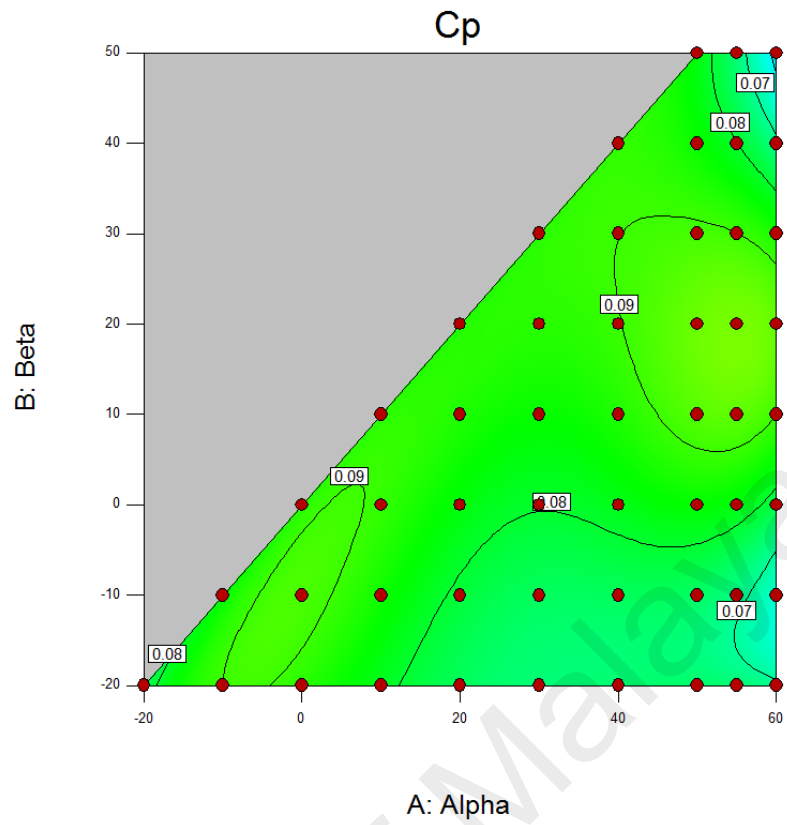


Figure 4.13: influence of the angles on the VAWT C_p at TSR=1.6.

Figure 4.11 Figure 4.12 and Figure 4.13 show the surface and contour plot of the effect of the α and β on the response which is the coefficient of the power in VAWT.

This test was done at TSR=0.8, 1.2 and 1.6. As seen, the highest performance of the VAWT is achieved when β is between 10° to 30° and α is between 40° to 60° when TSR=1.2. A more detailed investigation of the effect of the guide vane angles are shown in Figure 4.14, Figure 4.15 and Figure 4.16.

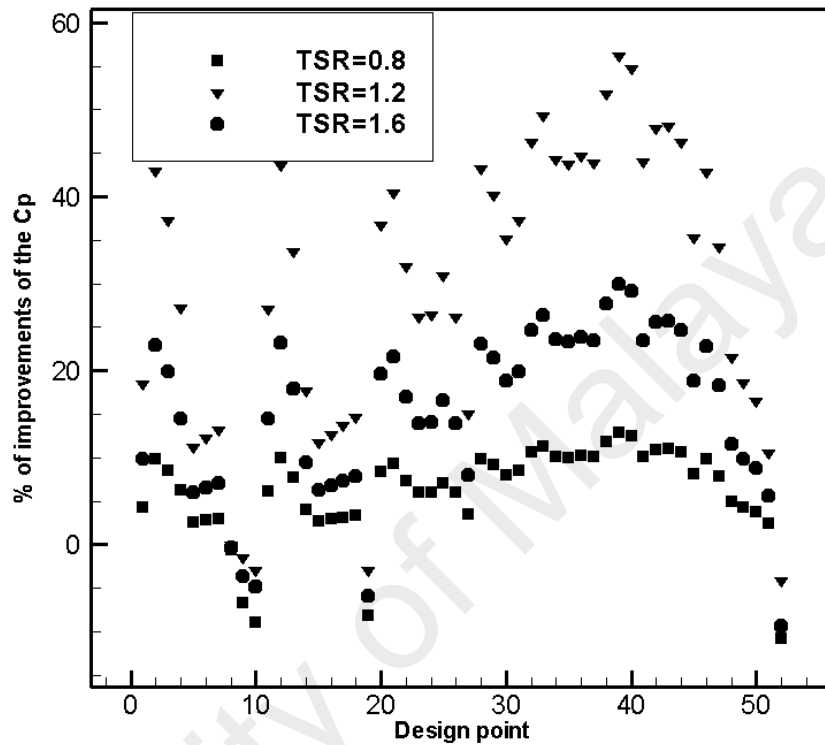


Figure 4.14: percentage of C_p improvements at different design points and TSRs.

Figure 4.14 shows the results of the CFD simulation at different TSRs for effect of the varying the angle of the guide vane on C_p . As it can be seen, in higher TSRs, the ODGV shows better improvements in the performance of the VAWT. Highest performance of the VAWT obtained in design point number 39, the angle of the ODGV in this design point are 55 and 20 for α and β respectively. At this design, point C_p is improved by approximately 12.8%, 56.10 % and 29.97 % at TSR= 0.8, 1.2 and 1.6 respectably. The negative impact of the ODGV can be observed at design points 8, 9, 10, 19 and 52 with -0.1269%, -1.544%, -2.96% and -4.12 % at the C_p improvement respectively at TSR=1.2.

The maximum amount of the C_p is reported at $TSR=1.2$, where this TSR is more illustrated at Figure 4.15 and Figure 4.16.

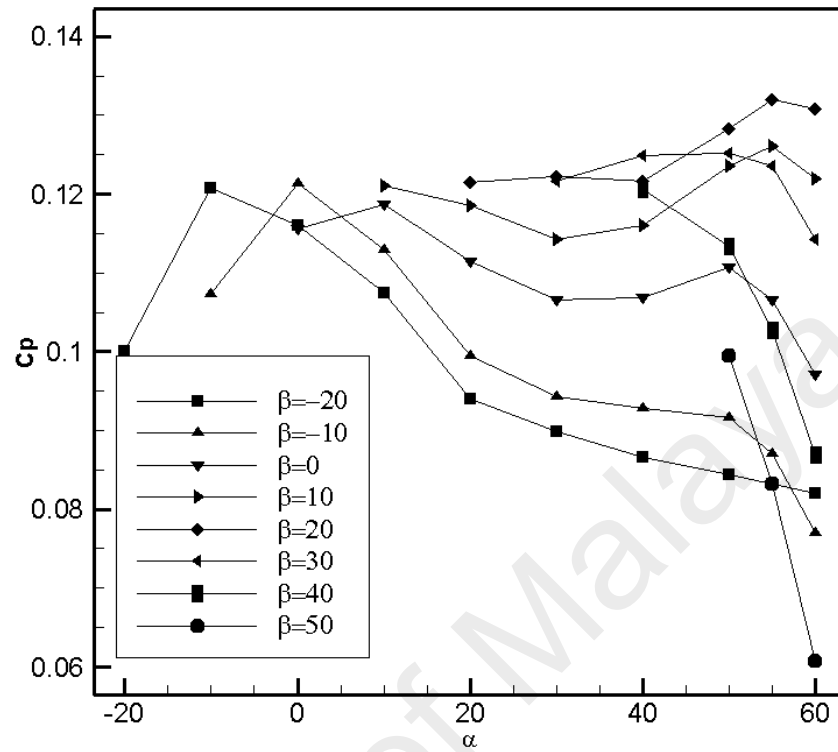


Figure 4.15: C_p variations based on different angle (β and α) of the ODGV walls.

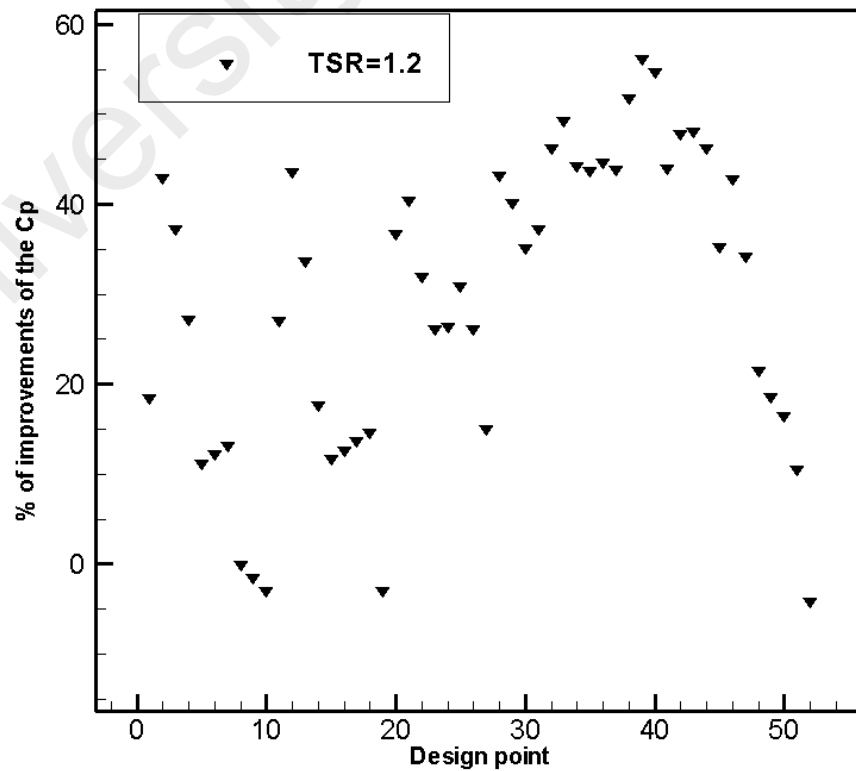


Figure 4.16: Percentage improvements of the C_p at different ODGV angles at TSR=1.2.

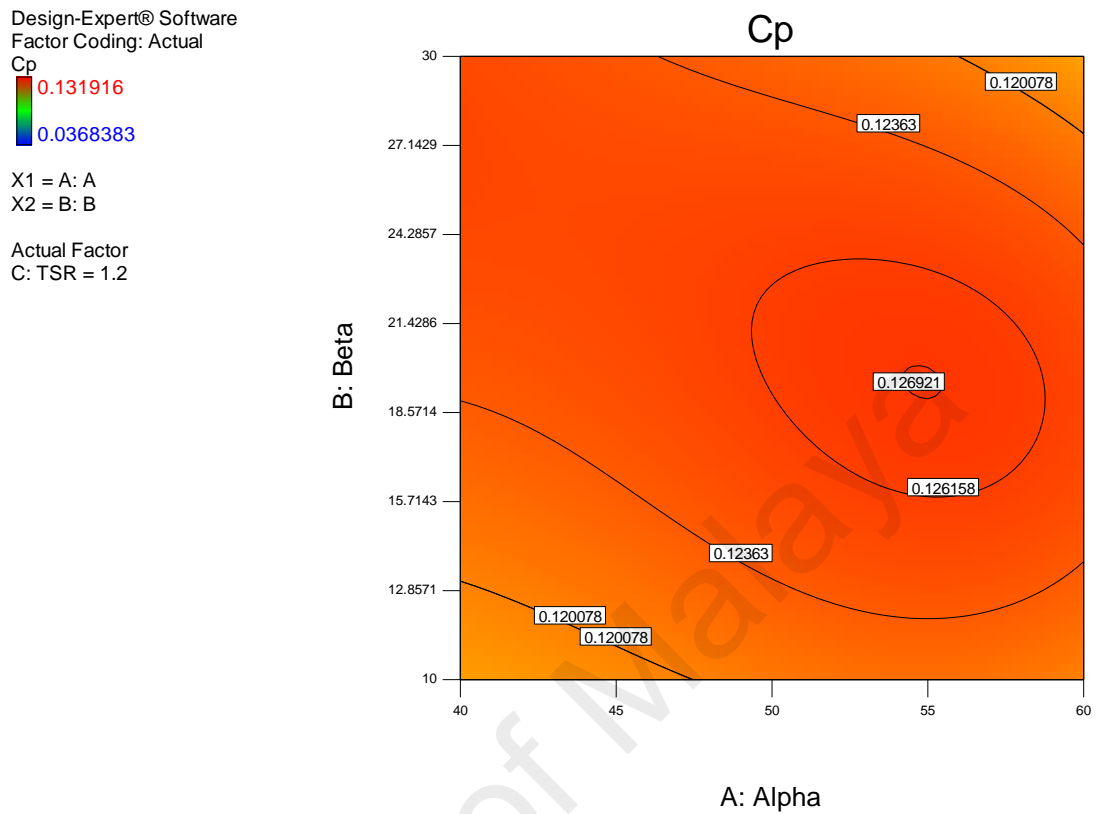


Figure 4.17: Maximum C_p at ranges of different α and β

As seen from Figure 4.17, C_p has been significantly changed by using various ODGV wall angles (β and α). Accordingly, the main improvement of the C_p occurred when the β and α ranges were between (10° and 25°) and (50° and 60°) respectively at all ranges of TSR. As a result, the highest enhancement through the simulation was achieved when β and α were 20° and 55° .

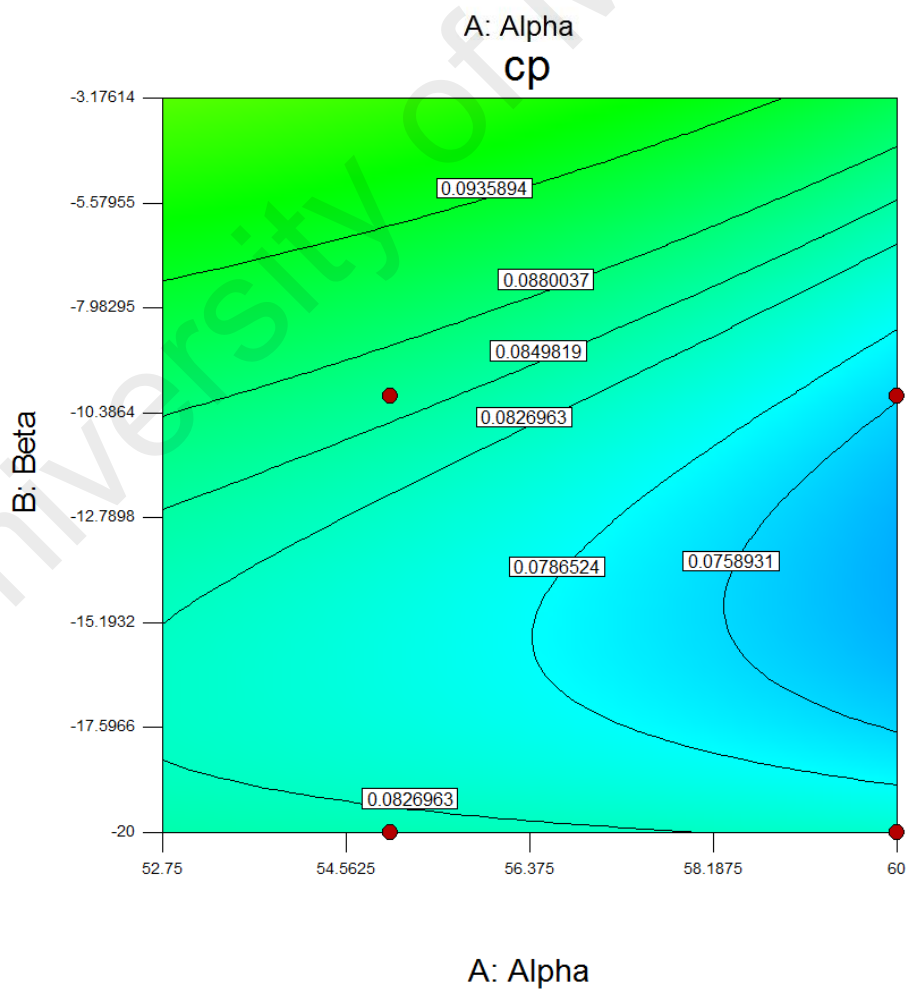
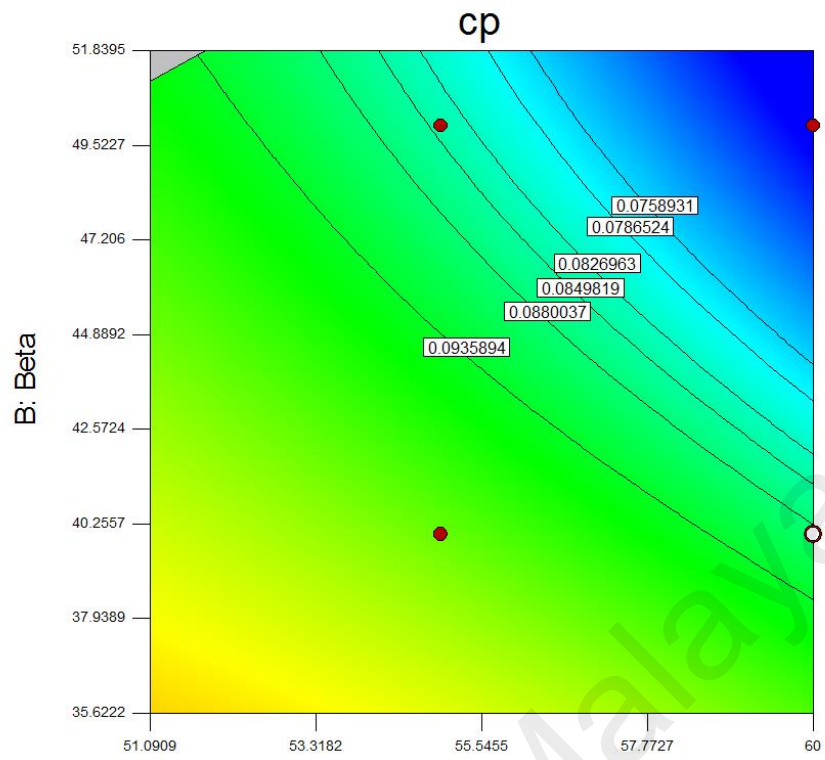


Figure 4.18: Minimum C_p in different ranges of α and β .

Conversely, the minimum effects occurred when β was between (35° and 50°), (-20° and -3°) and α was between (50 and 60) respectively (Figure 4.18).

Briefly, based on previous figures, the maximum output of the VAWT was captured when the ODGV was in an optimum position ($\beta=20^\circ$ and $\alpha=55^\circ$). Hence, comparison of the C_p with and without ODGV in three considered TSRs are illustrated by Figure 4.19.

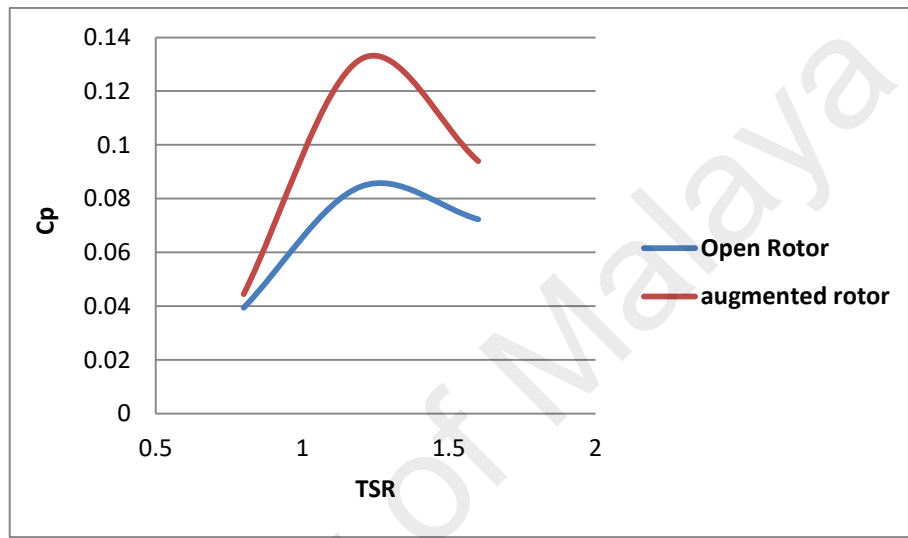


Figure 4.19: Comparison of the C_p with and without ODGV at three tested TSR.

As seen from Figure 4.19, the maximum C_p of the open and augmented rotor were 0.084 and 0.131 respectively at $TSR=1.2$. The simulated results also indicated that the ODGV can improve the C_p more than 12.8%, 56.10 % and 29.97 % at $TSR= 0.8$, 1.2 and 1.6 respectively when $\beta=20^\circ$ and $\alpha=55^\circ$.

In terms of C_m , prediction of the C_m through one rotation of the VAWT and comparison between one and the five bladed VAWT simulation results for open and augmented rotor are presented in Figure 4.20 (for optimum ODGV angle and constant TSR) at $TSR=1.2$.

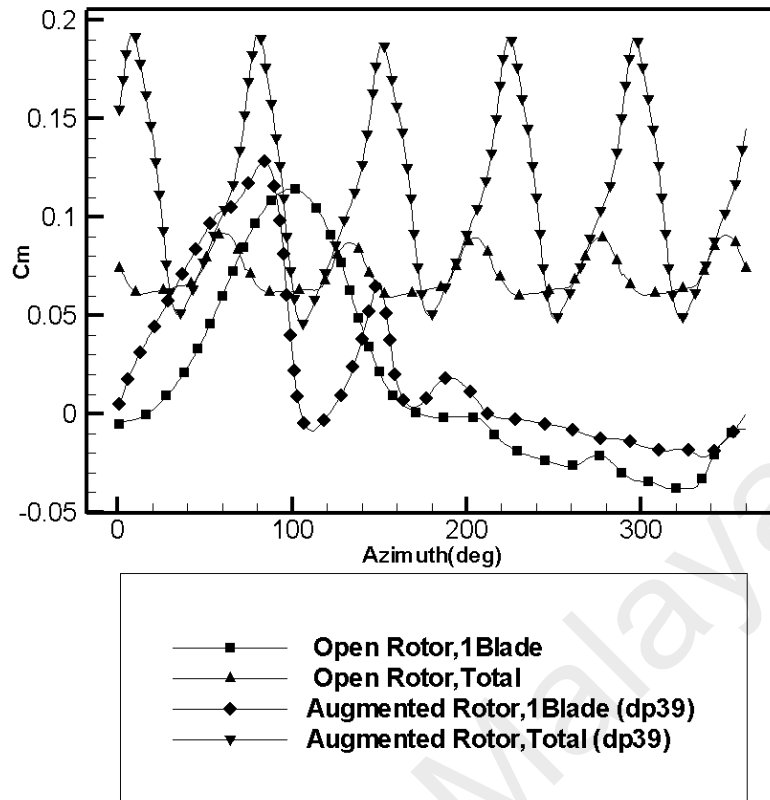


Figure 4.20: ODGV impact on C_m of the VAWT in various azimuth angles at $TSR=1.2$.

As seen from Figure 4.20, averages of the C_m for the open rotor and augmented rotor were 0.070 and 0.109 respectively (55% improvement in the C_m). The maximum C_m of a one blade open rotor is reported in the azimuth angle $110(\theta=110^\circ)$, while the maximum C_m for augmented rotor happened in two different C_m peaks. Once in $\theta=90^\circ$, and a second time in $\theta=140^\circ$. A significant improvement in C_m was achieved when $\beta=20^\circ$ and $\alpha=55^\circ$ within $\theta=120-360^\circ$. Furthermore, C_m variations based on the different azimuth (θ) and ODGV (β and α) angles in one rotation and constant TSR are indicated by Figure 4.21.

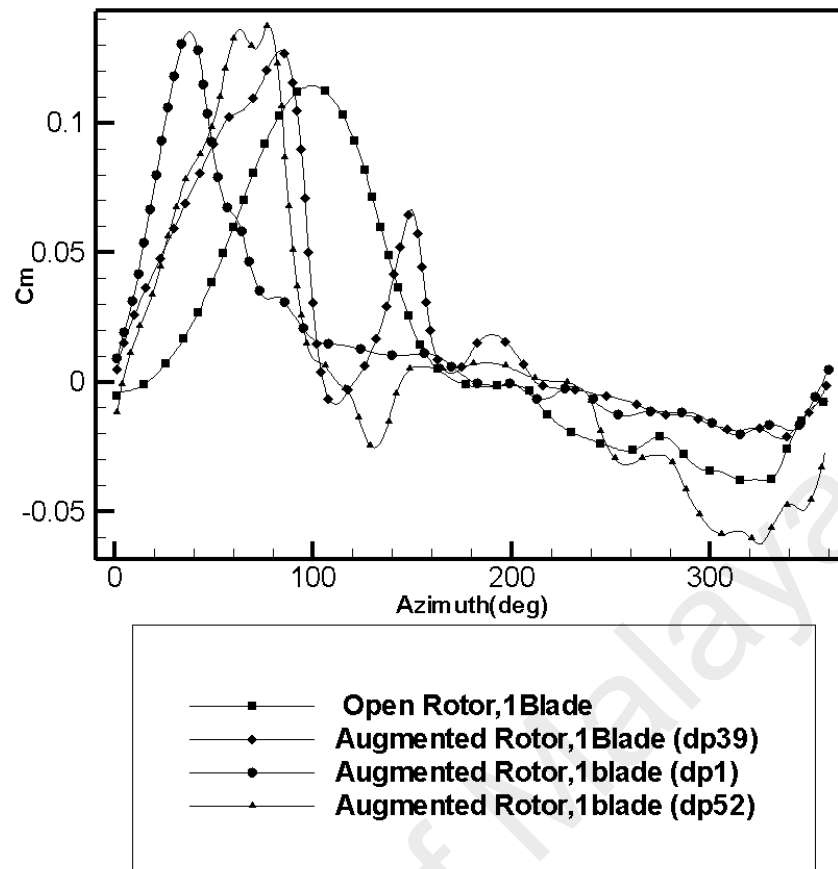


Figure 4.21: Torque coefficient (C_m) variation in one rotation with different ODGV angles at $TSR=1.2$.

Figure 4.21 shows the effect of the ODGV angle on the C_m . by considering the huge number of the design points and simulation. In this graph, only three-design points are illustrated. The design points are 1, 39 and 52 with improvements of the 18%, 56%, -4% in C_p . Positive improvements in terms of the C_m is achieved in the azimuth angle between (160° and 360°) in design points 1 and 39. However, for design point number 52, a negative effect on the C_m reported during the azimuth angle between (100° and 360°). This effect can be discussed based on the vector contours, which are done in next section. In conclusion, the ODGV with ($\beta=20^\circ$ and $\alpha=55^\circ$) is the best option to improve the torque generation in the VAWT. These results can also be validated by velocity vectors, which are explained in the following section.

4.4.1 Velocity Vectors

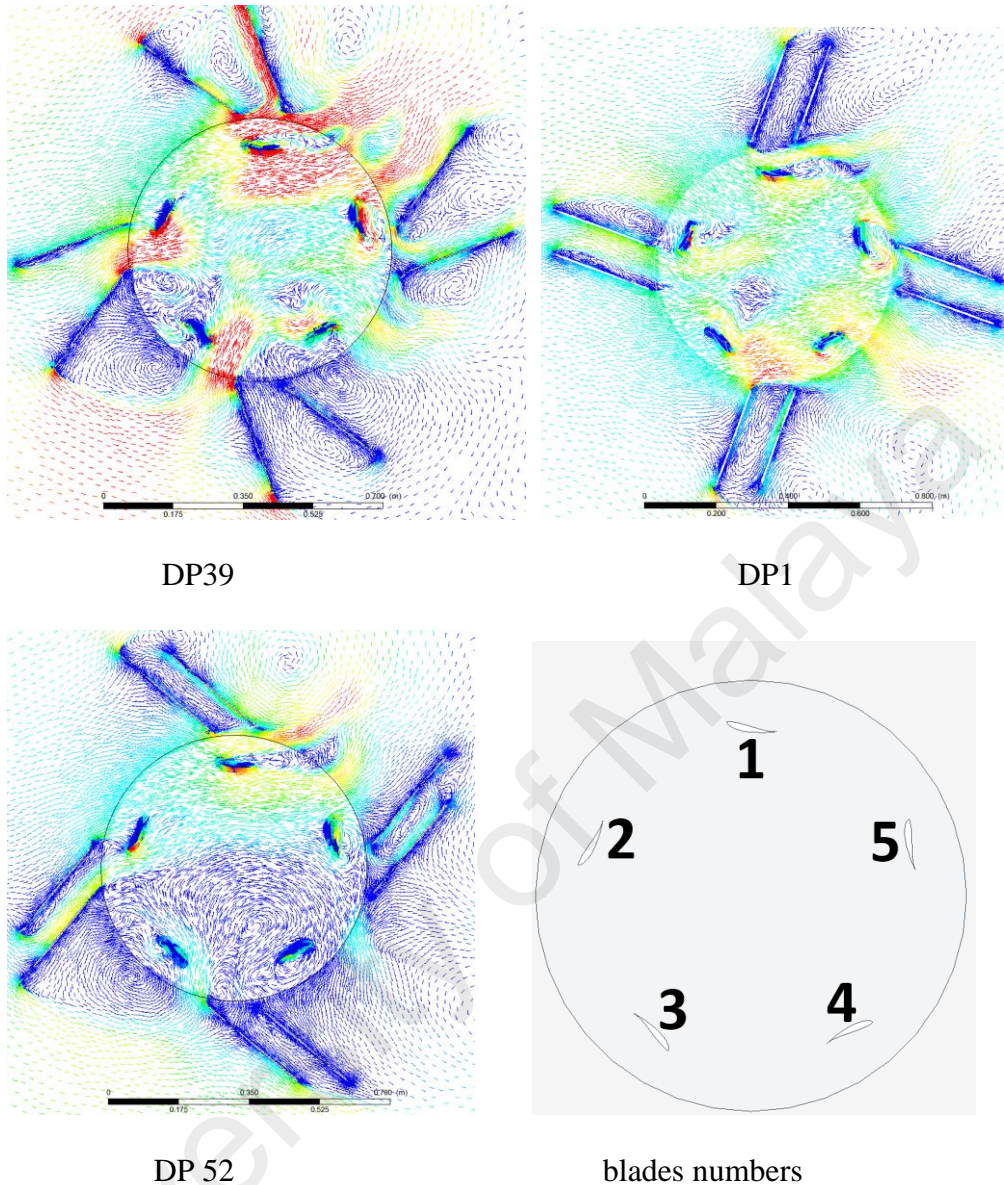


Figure 4.22: Vectors around the domain in different guide vane angles.

Figure 4.22 shows the vector plot in three different guide vane angles. Using the correct angle on the ODGV can improve the velocity profile around the VAWT significantly. These improvements can be seen in its highest level in dp39. In this design point, red vectors show the higher velocity profile which helps to improve the torque generation in the VAWT. Three high velocity profiles can be reported in this design point. The first one is in ($\theta=70^\circ$ to $\theta=90^\circ$), the second improvement is in ($\theta=170^\circ$ to $\theta=190^\circ$), and the last improvement is in ($\theta=230^\circ$ to $\theta=360^\circ$).

At the design point number 52, the ODGV has a negative impact on the VAWT performance. Using this configuration for the ODGV angles reduces the torque generation, especially between the azimuth angle ($\theta= 100^\circ$ and $\theta= 130^\circ$) and ($\theta= 230^\circ$ and $\theta=260^\circ$).

At design point 1, the ODGV improved the C_p of the VAWT by 18%. The configuration of the angles helps to improve the torque generation but not significantly. A few high velocity regions can be reported in this design point, which is reported also in Figure 4.22.

4.5 INFLUENCE OF THE ODGV SHAPE RATIO

In the next step of the optimization on ODGV, the outer diameter of the Omni-direction-guide-vane is investigated. As mentioned in the previous section, the RSM method is also coupled with the CFD simulation to achieve a better solution, not only in specific configurations but also in all ranges of the variables.

Five identical outer diameters were selected as a first investigation factor. These outer diameters are shown in **Table 4.2**.

Table 4.2: Shape ratio of the ODGV.

$D_{O\ ODGV}(\text{mm})$	$D_{i\ ODGV}(\text{mm})$	$R_{\text{shape ratio}}$
1400	700	0.5
1272	700	0.55
1166	700	0.6
1076	700	0.65
1000	700	0.7

Where the Rshape ratio is:

$$R_{\text{shape ratio}} = D_{i\ ODGV} \setminus D_{o\ ODGV} \quad (4.1)$$

Internal length of the guide vane (L) was also selected as a second factor. This length varies between 100mm to 300 mm. The three different tip speed ratios $TSR = 0.8, 1.2$ and 1.6 were the next investigated factors. The three different flow angles (ψ) were ($0^\circ, 22.5^\circ, 45^\circ$) the last factor of the investigation. The schematic of the factors and flow angles are shown in Figure 4.23.

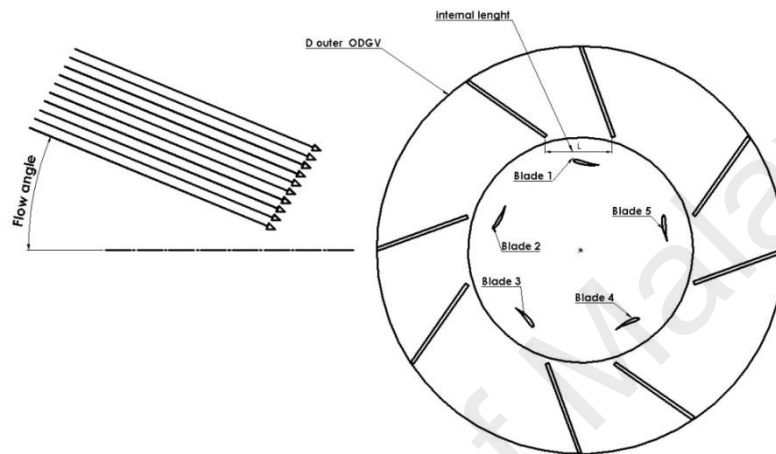


Figure 4.23: Schematic view of the investigating factors.

Based on the mentioned factors, the RSM and CFD simulation were carried out to determine the best shape of the ODGV to achieve the highest performance in VAWT.

The ANOVA statistic analysis shows that the simulation of the ODGV shape ratio model is significant by F value equal to 63.37. The significant model terms are those with 'Prob. > F' value of less than 0.05. This implies that the flow angle is the most effective factor in this model.

The "Pred R-Squared" of 0.9897 is in reasonable agreement with the "Adj R-Squared" of 0.9998; i.e. the difference is less than 0.2. The "Adeq Precision" measures the signal to noise ratio.

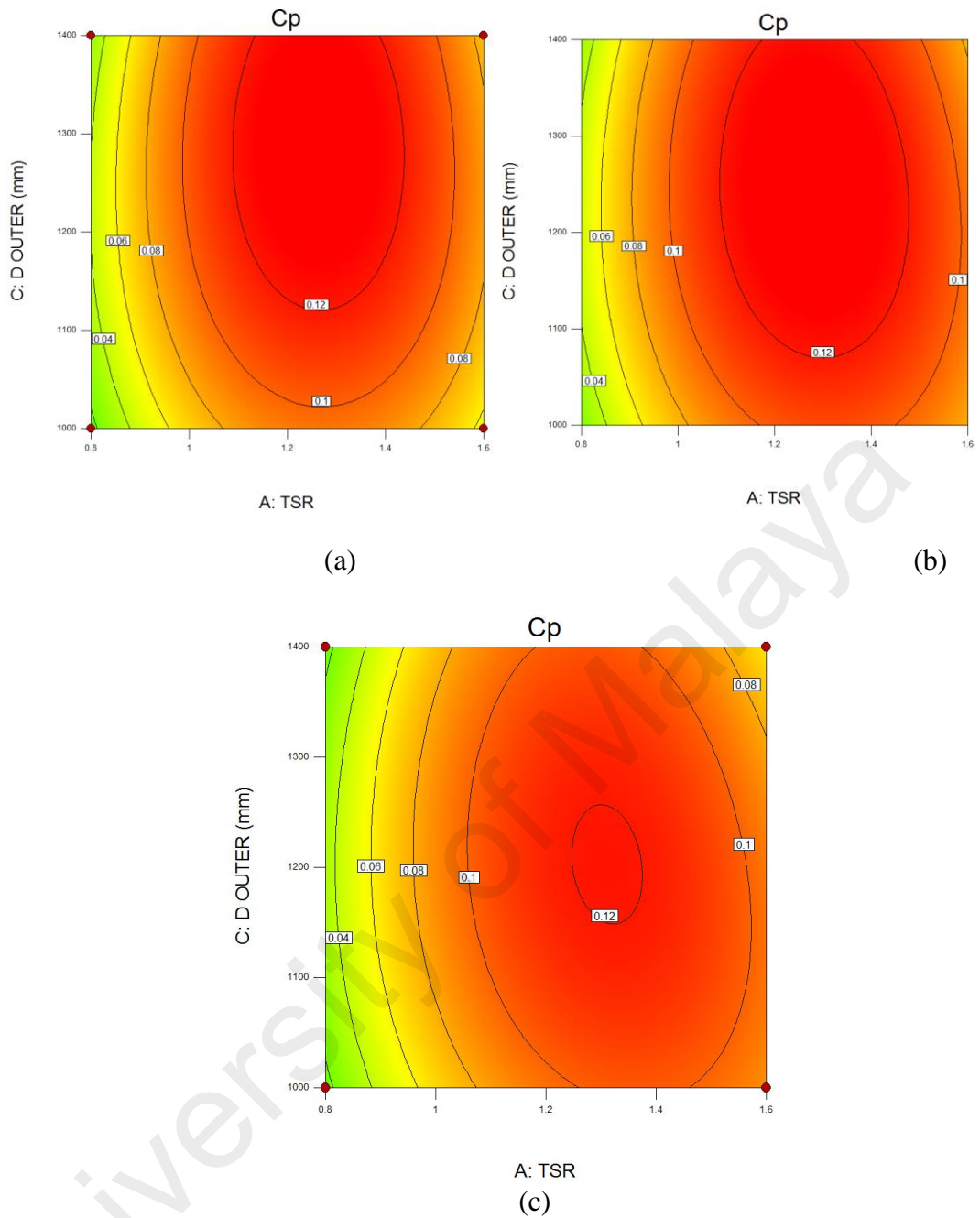


Figure 4.24: Influence of the variation of the outer diameter at $\psi=0^\circ$ and $L=100$ (a), $L=200$ (b), $L=300$ (c).

Figure 4.24 shows the variation of the C_p of the VAWT during different internal lengths when the flow angle is zero. As seen, between these three internal lengths, $L=200$ has the highest positive effect on the performance of the VAWT. The best outer diameter range in this configuration is $R=0.55$ ($D_{ODGV} = 1272\text{mm}$).

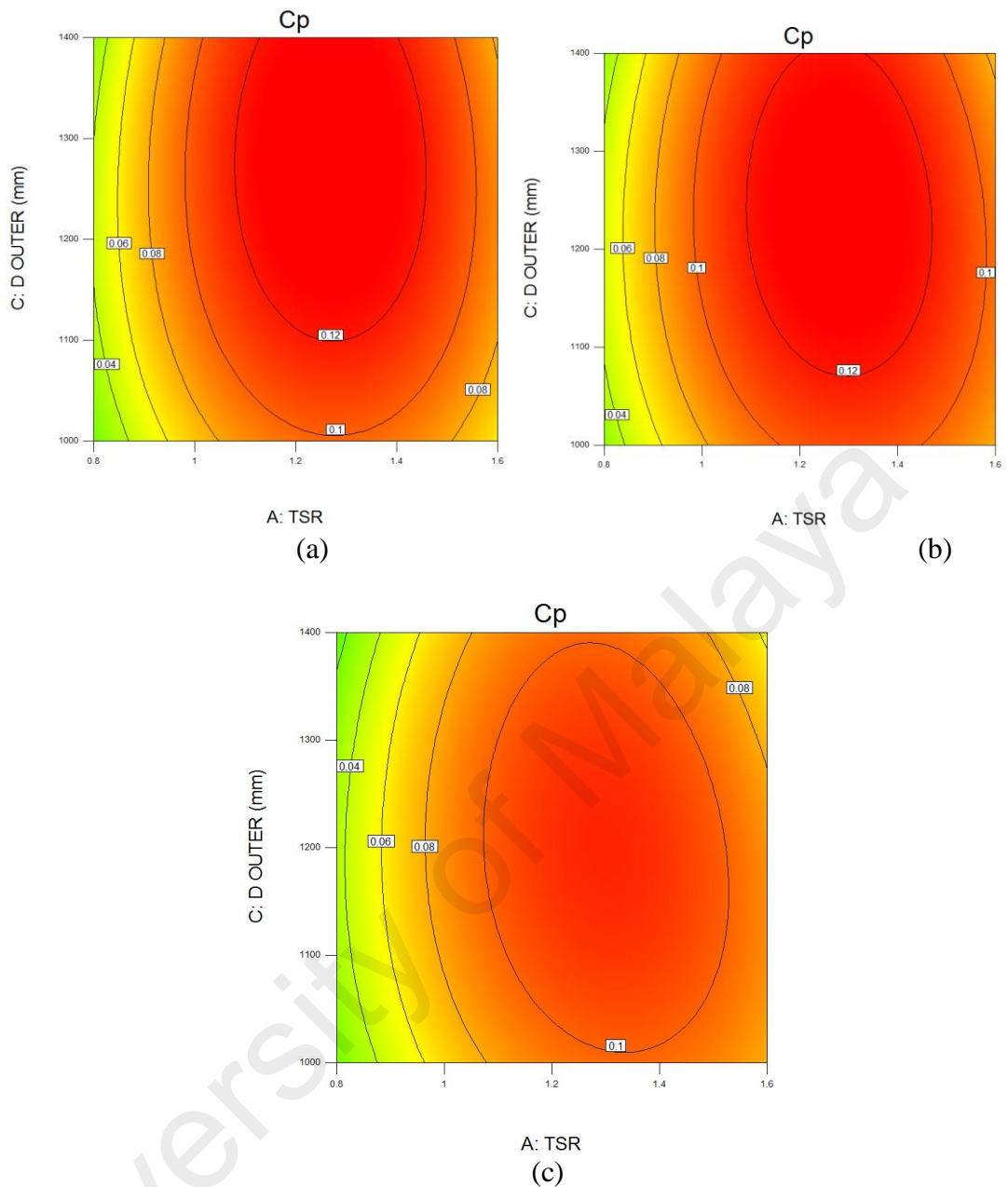


Figure 4.25: Influence of the variation of the outer diameter at $\psi=22.5^\circ$ and $L=100$ (a), $L=200$ (b), $L=300$ (c).

According to Figure 4.25, increasing the flow angle up to 22.5 degrees decreases the performance of the VAWT. The internal length, $L=200$ also cause the highest C_p among the other lengths.

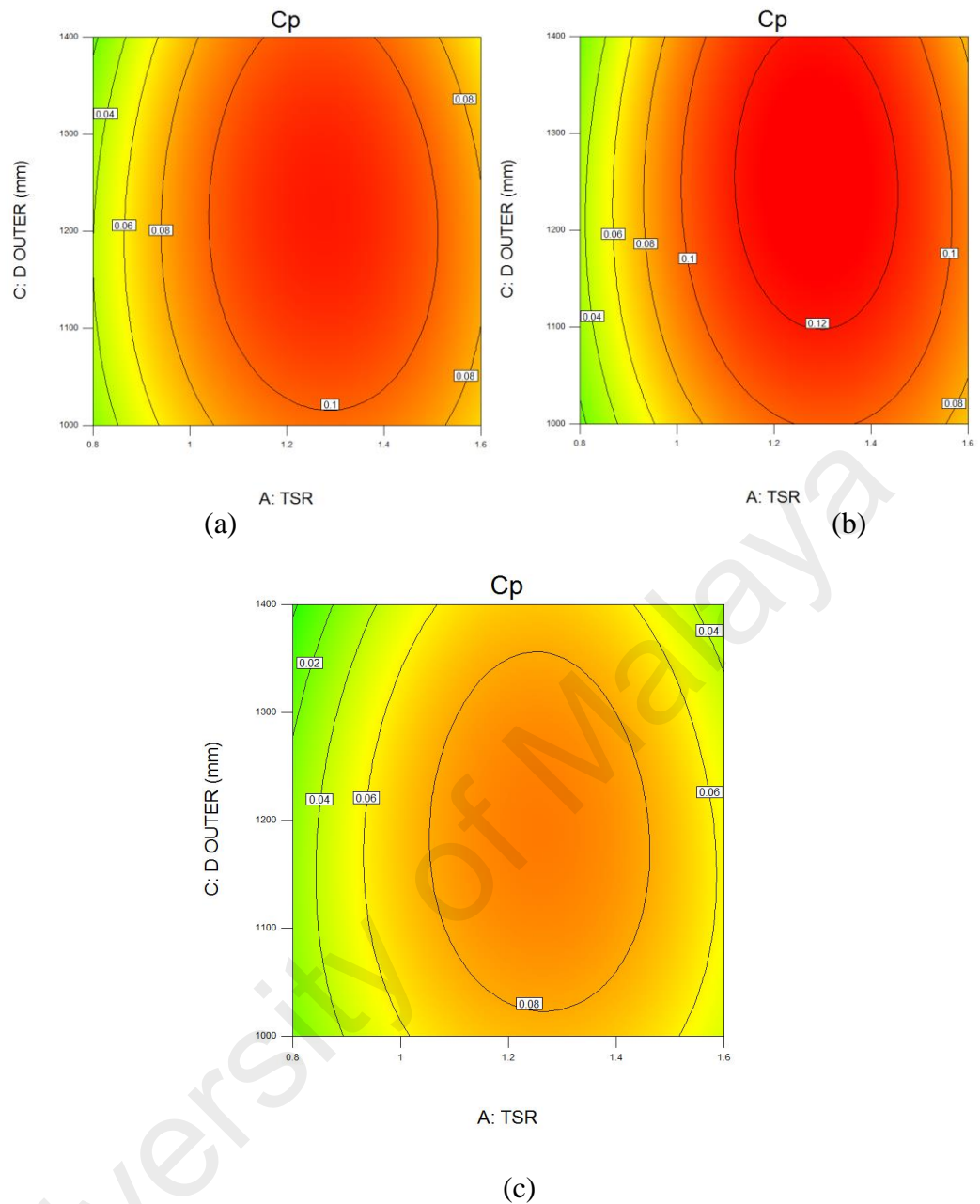


Figure 4.26: Influence of the variation of the outer diameter at $\psi=45^\circ$ and $L=100$ (a), $L=200$ (b), $L=300$ (c).

As it can be seen in Figure 4.26, $L=300$ has the lowest effect on the performance of the VAWT, especially when in a higher flow angle. At this flow angle, $L=200$ again has the highest positive effect on the C_p .

The effect of the shape ratio of the ODGV on the VAWT was investigated in this part of the thesis . Five different shape ratios between 0.5 and 0.7 were tested. The biggest shape ratio is 0.5 with a diameter of 1400mm, with the smallest one having a shape ratio of 0.7 with an outer diameter for the ODGV of 1000mm. The torque

coefficient, power coefficient and velocity contour in different shape ratios were calculated in this step. Overall, 30 simulations were conducted and among these simulations, five different shape ratios in three different TSRs were simulated. Each simulation for the augmented rotor takes around 18 hours and every simulation stabilizes and converges after a six rotor rotation. Figure 4.27 shows the C_m versus the azimuth angle for both, the open and the augmented rotor with different shape ratios.

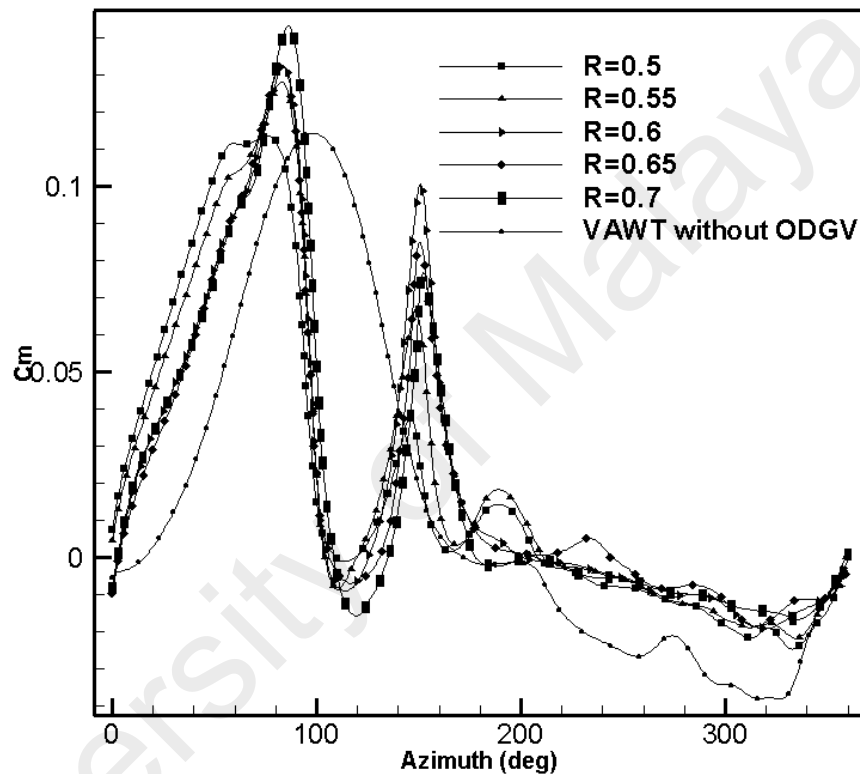


Figure 4.27: Torque coefficient versus azimuth angle at different shape ratios of the ODGV including the open rotor case at TSR=1.2.

As shown in Figure 4.27, the highest C_m is generated between the azimuth angles of $\theta = 0^\circ$ to $\theta = 105^\circ$. Between the azimuth angles $\theta = 105^\circ$ and $\theta = 205^\circ$ for the shape ratios of 0.7 to 0.5, the peak for C_m is higher than the open rotor. From the azimuth angles between $\theta = 205^\circ$ and $\theta = 360^\circ$, a positive effect on C_m can be reported for all shape ratios. In addition, the torque coefficient variations were observed for different shape ratios (R) based on the TSR between 0.8 and 1.6. These results are illustrated by Figure 4.28.

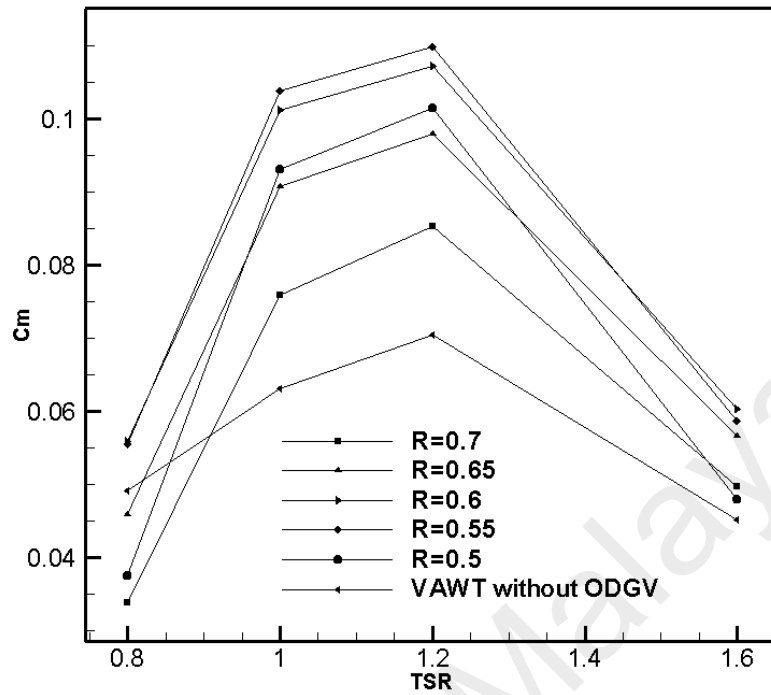


Figure 4.28: Average torque coefficient versus TSR for different shape ratios of the ODGV.

The best performance was achieved by using the ODGV with the shape ratio of 0.55 by a 55% overall enhancement in an averaged C_m . However, negative effect on the C_m observed in shape ratio 0.7, 0.65 and 0.5 when the tip speed ratio is less than 0.9. At the high TSR (TSR=1.6), almost all shape ratios had the same impact on the torque coefficient, except the $R_{\text{shape ratio}}=0.5$ and 0.7.

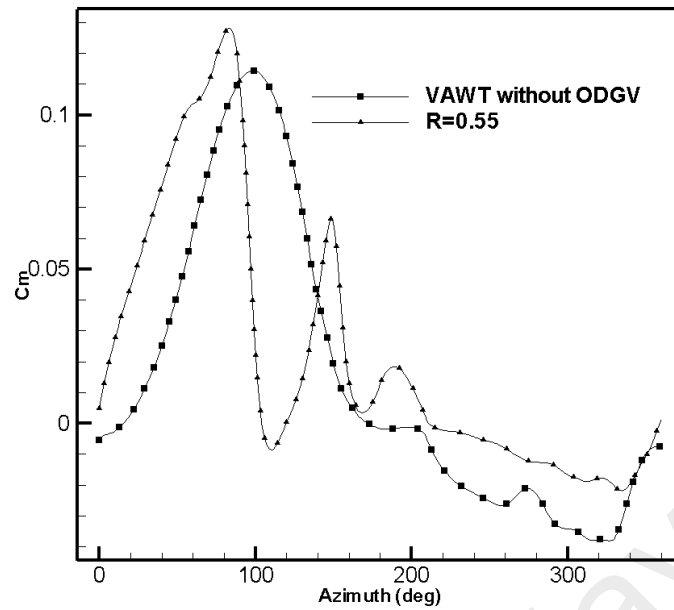


Figure 4.29: Torque coefficient versus Azimuth angle for open and augmented rotor at $TSR=1.2$, $R=0.55$.

The highest effect of the ODGV shape ratio was achieved when the outer diameter of the ODGV is 1272mm and the internal length is 200mm during the flow angle zero at $TSR=1.2$. This configuration is more discussed in this section. Figure 4.29 shows the variation of the torque generation with and without ODGV in one complete rotation. The solid line shows the augmented rotor, while the dashed line shows the open rotor. Using the shape ratio of 0.55 helps to improve the torque generation, especially during the azimuth angle between (200° and 360°). A three peak position of torque generation can be reported at the azimuth angle of 80° , 145° and 190° .

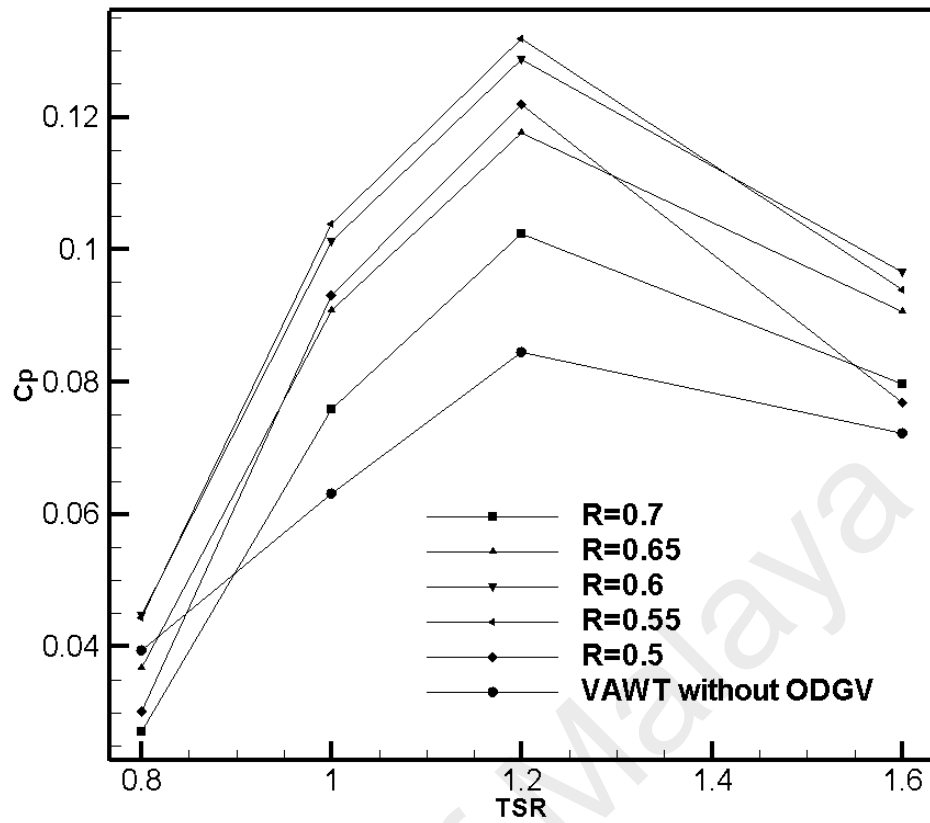


Figure 4.30: Power coefficient versus TSR for open and augmented rotors.

Trends of Figure 4.28 and Figure 4.30 are identical at different rates. The highest C_p for both, the augmented and open rotor was reported at TSRs between 1 and 1.4. The maximum C_p value is 0.1317 for the augmented rotor when the shape ratio is 0.55. The shape ratios of 0.55, 0.6 have almost the same effect on the C_p at TSRs lower than 1.

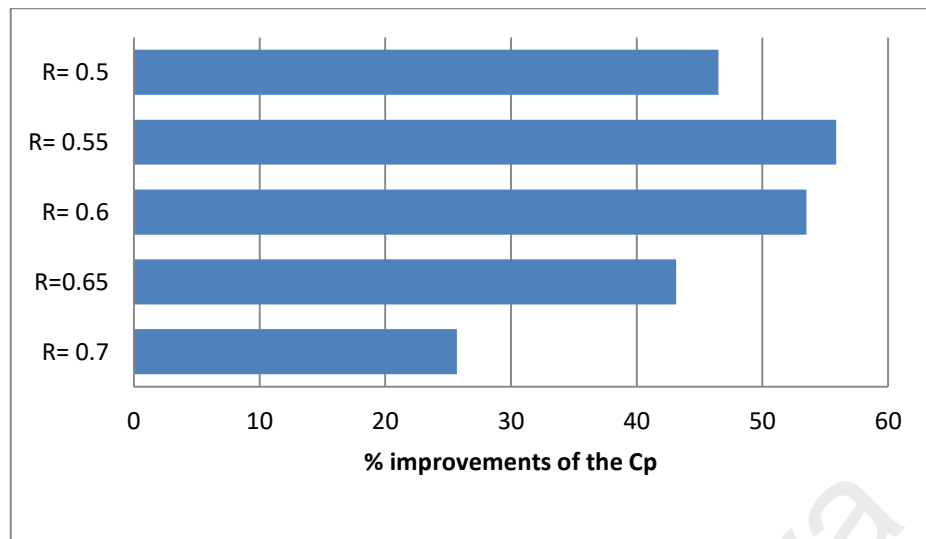


Figure 4.31: Percentage of the improvement of C_p using different $R_{\text{shape ratio}}$.

Figure 4.31 shows percentage of improvement of this generation compared to the open rotor. 56% of improvement in the C_p was achieved by using the shape ratio of 0.55. The lowest improvement happened at shape ratio 0.7 with a 26% improvement in C_p . After shape ratio 0.55, the shape ratio 0.6 has the highest impact on the increasing the performance of the VAWT with a 53% improvement.

4.6 THE EFFECT OF THE NUMBER OF GUIDE VANES

In this part, effect of the number of the guide vanes on the performance of the VAWT is investigated. Three different types of guide vanes that consist of the four, five, six bladed ODGV (Figure 4.32) was compared with the optimized guide vane at different working conditions and flow angles.

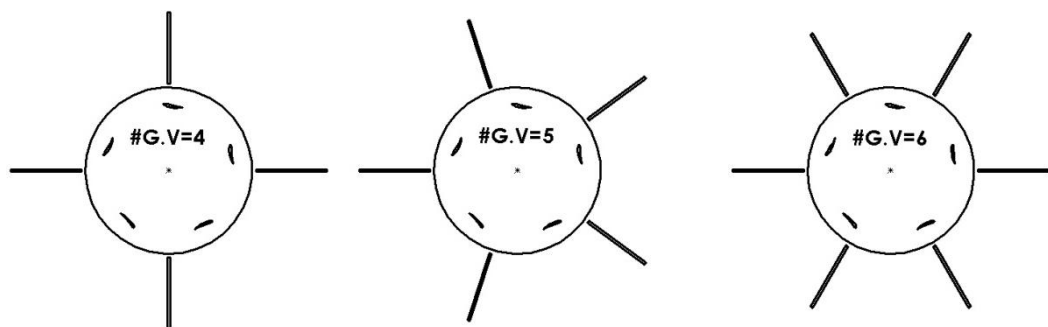


Figure 4.32: Schematic view of the number of the guide vanes.

4.6.1 ODGV with Four Bladed Guide Vane

4.6.1.1 Power Coefficient of the Augmented VAWT with Four Bladed ODGV

Variation of the coefficient of the power versus the tip speed ratio at different flow angles for #G.V=4 are shown at Figure 4.33 and Figure 4.34. At this figure, the O.R represents the open rotor VAWT. Two different phenomenon are observed in this configuration of the ODGV. Firstly, between the TSR (0.8 and 1) and secondly, between TSR (1 to 1.6). A positive effect of the ODGV can be reported at TSR=0.8 to TSR=1. The best performance of the ODGV was achieved at the lowest TSR with the highest flow angle. The flow angle =45 at TSR=0.8 showed a 93% improvement for C_p . At the range of the TSR=1 to TSR =1.6, the ODGV showed the negative impact on the turbine performance when the ODGV has only four guide vanes. At this range, by increasing the TSR, performance of the VAWT was decreased. The least performing was at flow angle=45 degree at TSR=1.6. In this mentioned angle and TSR results showed that by comparison between two cases open rotor and augmented rotor with four bladed ODGV, performance of the turbine drop 73%.

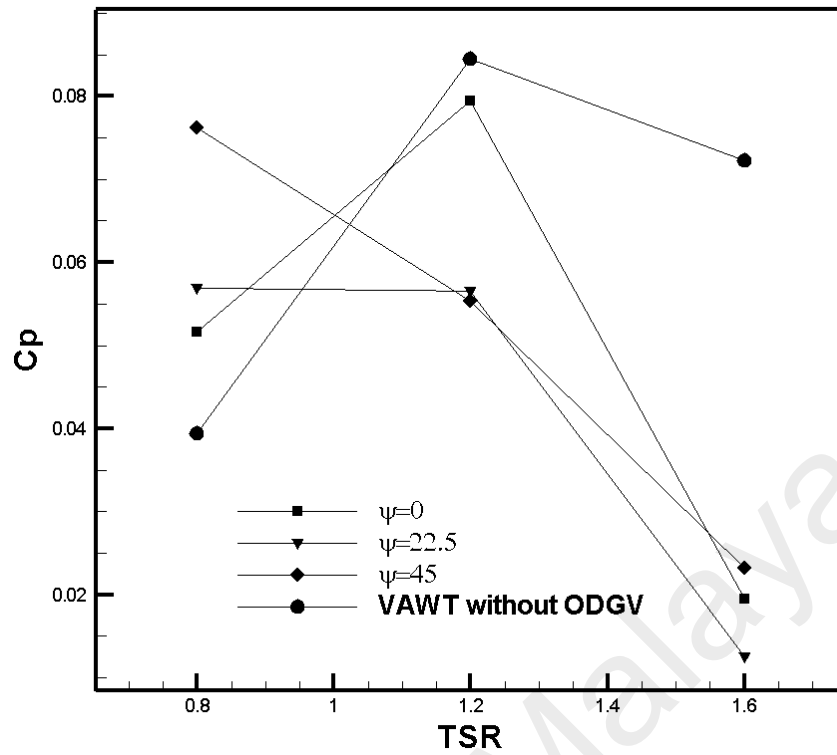


Figure 4.33: C_p vs. TSR at #G.V=4 at different flow angles.

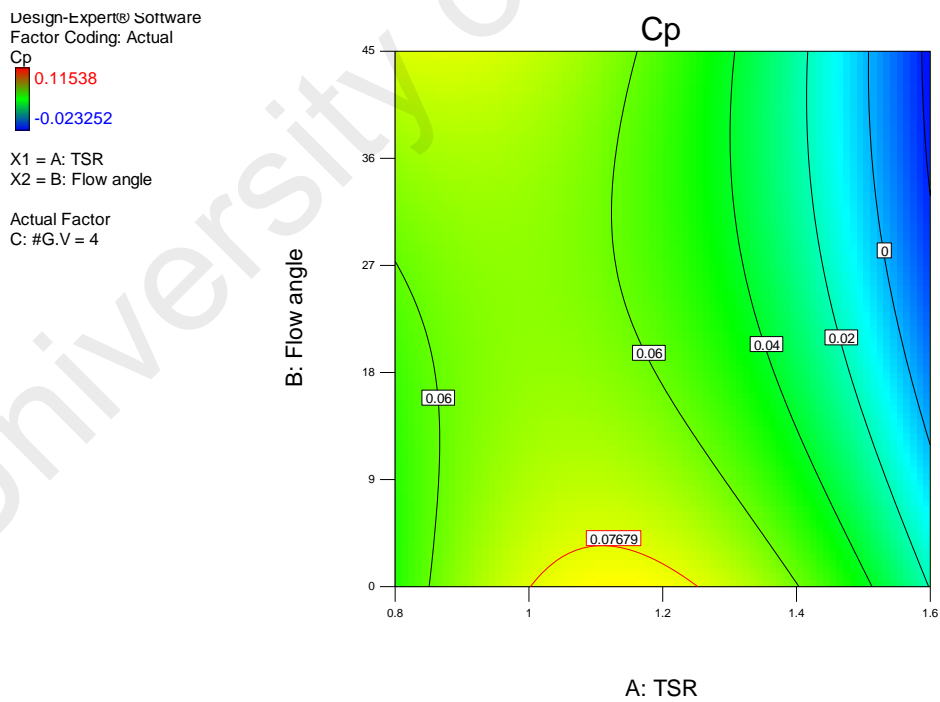


Figure 4.34: Variation of the C_p at different TSRs and flow angles in #G.V=4.

4.6.1.2 Torque Coefficient of the Augmented VAWT with Four Bladed ODGV

The C_p is highly dependent on the variation of the coefficient of the torque in the turbine. Therefore, in Figure 4.35, Figure 4.36 and Figure 4.37 variation of the C_m at different flow angles at three specific TSRs are reported.

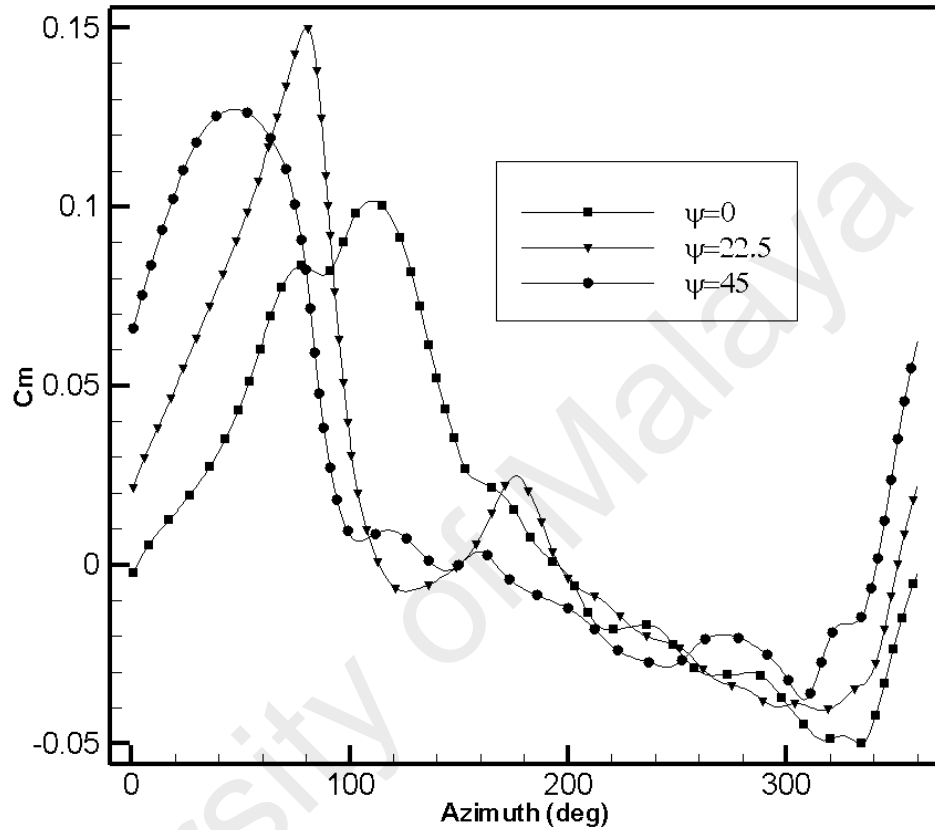


Figure 4.35: C_m Vs. azimuth in #G.V=4 at different flow angles, TSR=0.8.

Coefficient of torque in one rotation at three different flow angles when the TSR=0.8 is shown for #G.V=4 in Figure 4.35. At this TSR, (TSR=0.8) a positive effect on the turbine performance is reported when the VAWT was augmented with a four bladed ODGV. During the $\psi=22.5$, a very sharp peak of the torque generation can be seen in the azimuth angle of 70°. While for $\psi=0^\circ$ and $\psi=45^\circ$, a very smooth increase in C_m was detected. Overall, at this TSR, using the ODGV with four bladed guide vanes gives a better performance at higher flow angles.

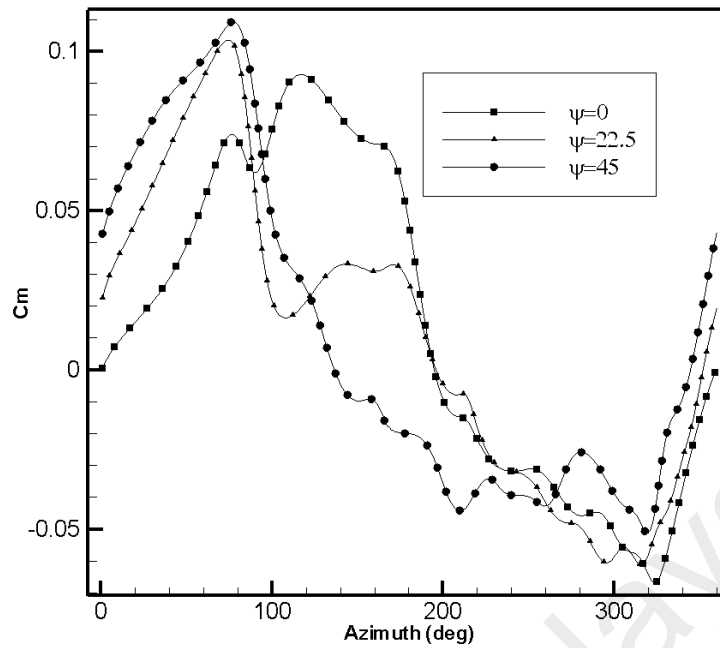


Figure 4.36: C_m vs. azimuth in #G.V=4 at different flow angles, TSR=1.2.

Negative impact in C_m by using the #G.V=4 was detected when TSR=1.2. For $\psi=22.5^\circ$ and $\psi=45^\circ$, it shows the same trend at the range of the azimuth angle between 0° and 100° . However, after the azimuth angle reaches 100° degrees, the C_m at the flow angle $=45^\circ$ shows a lower amount compared to the other two flow angles. At this TSR, increasing the flow angle will cause a reduction in the performance of the turbine.

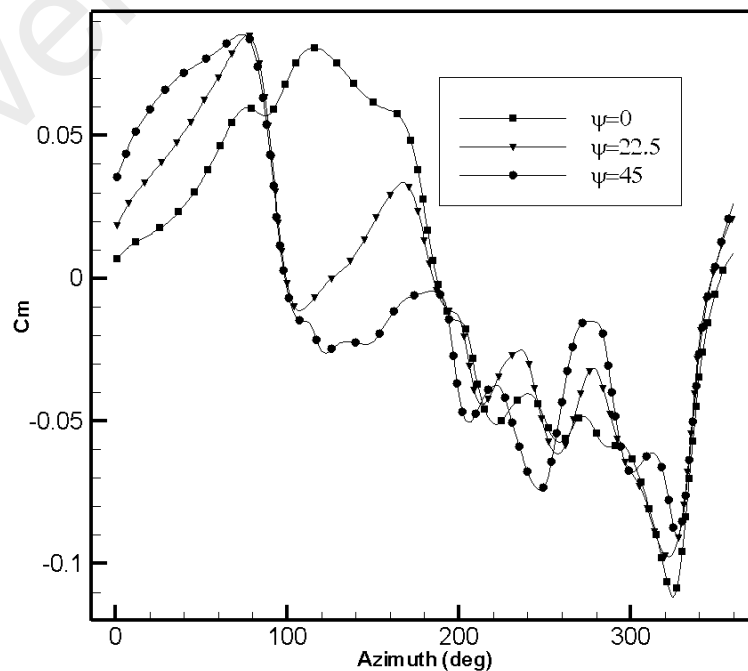


Figure 4.37: C_m vs. azimuth in #G.V=4 at different flow angles, TSR=1.6.

A similar trend of the C_m when $TSR=1.2$ was observed at $TSR=1.6$. However, after the azimuth angle of 200 degrees, the coefficient of the torque fluctuated further compared to the lower TSRs. At this TSR, the lowest performance of turbine occurred in the flow angle $=45^\circ$ with a 73% decrease on the C_p compared to the open rotor case.

4.6.1.3 Visualization of the Augmented VAWT with Four Bladed ODGV

The vorticity contour of the augmented turbine with the four bladed ODGV is presented in Figure 4.38. As it can be concluded from this contour, a lower vorticity helps to improve the torque generation in blades. In this direction, comparison between Figure 4.33 and Figure 4.35 shows that at $TSR=0.8$, the best performance of the VAWT was achieved at $\psi=45^\circ$. While at this TSR, the worst results took place at $\psi=0^\circ$. by looking at the vorticity contour at the azimuth angle 144° where the high vorticity region is shown at the top of blade number three at $\psi=0^\circ$. This vorticity region was demolished by increasing the TSR. The negative impact of the use of a four bladed ODGV at $TSR=1.6$ was mentioned previously. In this regard, in $\psi=45^\circ$ and $TSR=1.6$, shows the high vorticity zone in the lower surface of blade number three. This vorticity zone was decreased by decreasing the flow angle.

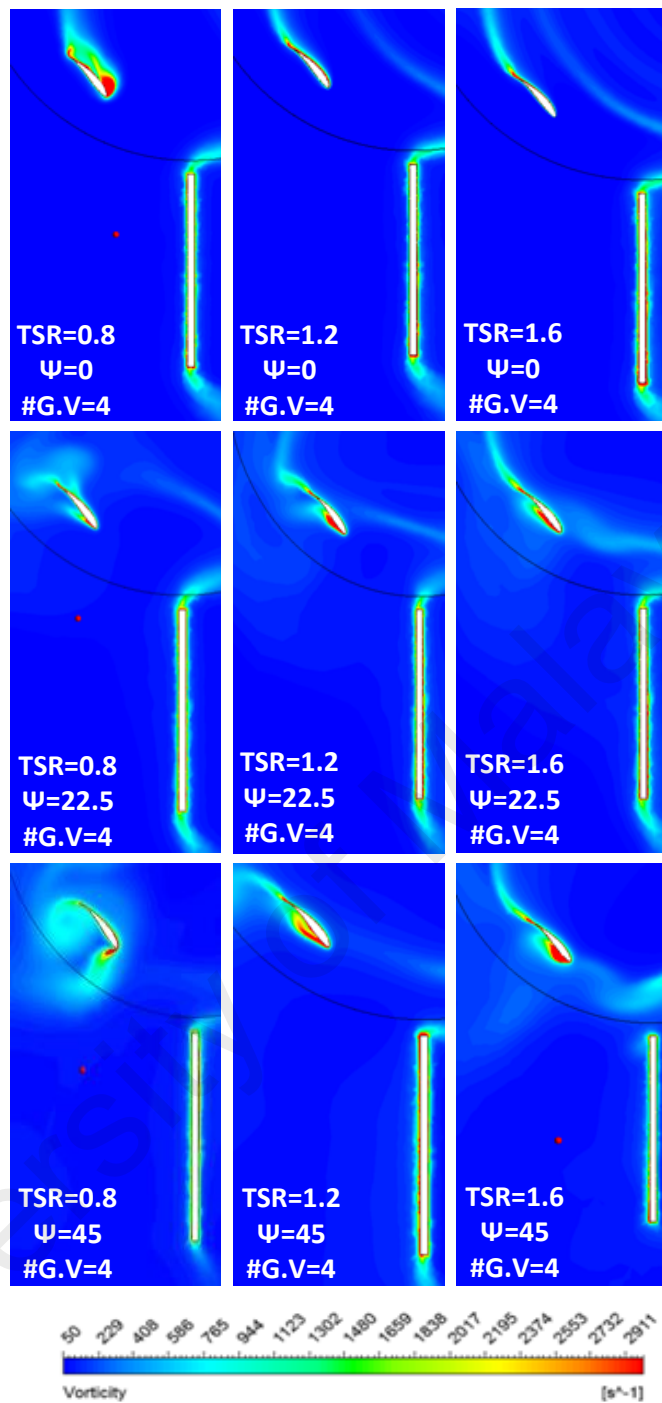


Figure 4.38: Vorticity contour in #G.V=4 around blade number3.

4.6.2 ODGV with Five Bladed Guide Vane

4.6.2.1 Power Coefficient of the Augmented VAWT with Five Bladed ODGV

Comparison between C_p of the VAWT at different flow angles when #G.V=5 is shown in Figure 4.39 and Figure 4.40. In this configuration, the ODGV has better results of improvements in terms of the coefficient of the power in VAWT compared to

the four bladed ODGV. However, the negative impact of using this type of ODGV at a higher flow angle is undeniable. The five bladed ODGV at high flow angle ($\psi = 45^\circ$) has a negative impact on the performance of the VAWT in all ranges of TSR's. This negative impact is more at lower TSR's. For example, at TSR=0.8, the negative impact of using five bladed guide vane shows 74% of reduction in performance compare to the open rotor case, while at TSR = 1.6, it shows a 17% decrease in the C_p in an augmented VAWT compared to the open rotor. The best performance of the ODGV with a five bladed guide vane was achieved at $\psi = 0^\circ$. At this flow angle, by increasing the TSR, the ODGV performance is also increased. 26% and 30% improvement of the C_p was detected at TSR= 1.2, and 1.6 respectively. In TSR=0.8, 45% reduction in C_p can be reported by comparing the performance before and after augmentation.

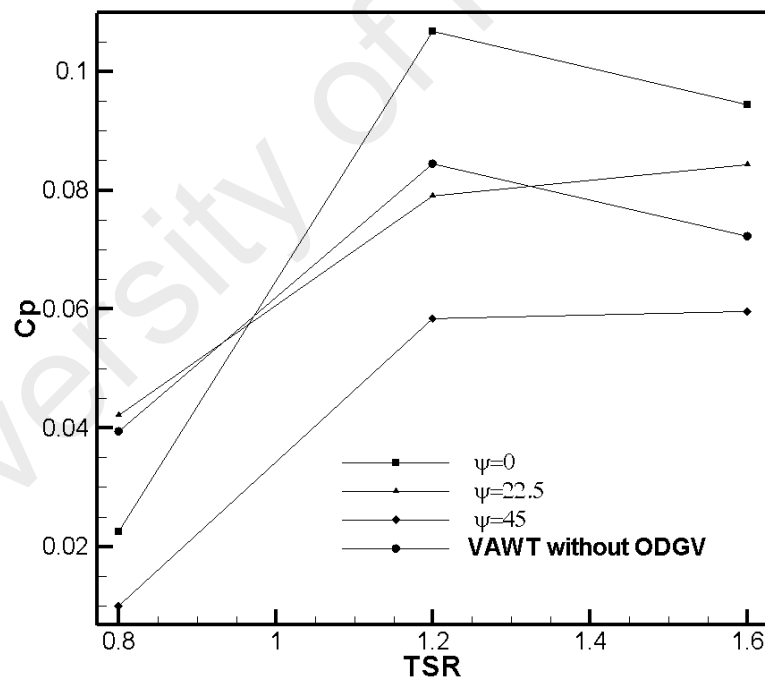


Figure 4.39: C_p Vs. TSR in #G.V=5 at different flow angles.

Design-Expert Software
 Factor Coding: Actual
 Cp
 0.11538
 -0.023252
 X1 = A: TSR
 X2 = B: Flow angle
 Actual Factor
 C: #G.V = 5

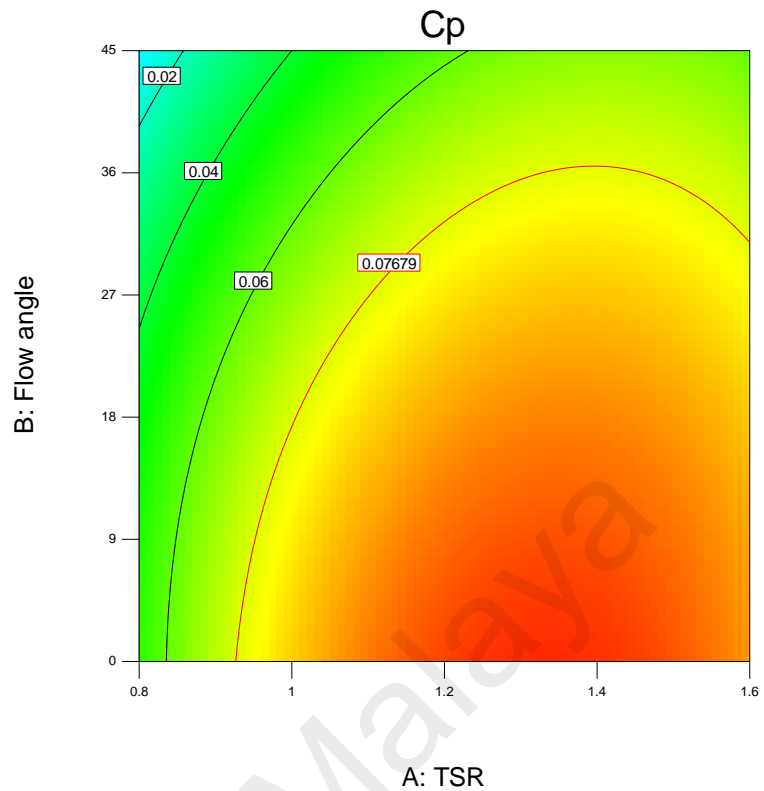


Figure 4.40: Variation of the C_p at different TSR and flow angles in #GV=5.

In the following three figures (Figure 4.41, Figure 4.42 and Figure 4.43), variations of the C_m versus the Azimuth angle illustrated during different flow angles for the five bladed ODGV.

4.6.2.2 Torque Coefficient of the Augmented VAWT with Five Bladed ODGV

As mentioned previously, at TSR=0.8, using the ODGV with five blades makes a negative impact on the performance of the VAWT in all ranges of the TSRs. The worst scenario is at flow angle = 45°. At this flow angle, a very low C_m peak takes place in the azimuth angle = 30°. At this TSR, $\psi = 0^\circ$ has the lowest negative impact on the C_m . Two peak generations of the torque occurred at $\theta = 30^\circ$ and $\theta = 90^\circ$ at $\psi = 0^\circ$. The best performance of the five bladed ODGV was captured during the TSR = 0.8 at $\psi = 22.5^\circ$. At this flow angle, the C_m showed the highest peak at $\theta = 65^\circ$ and the second peak of the C_m is at $\theta = 160^\circ$.

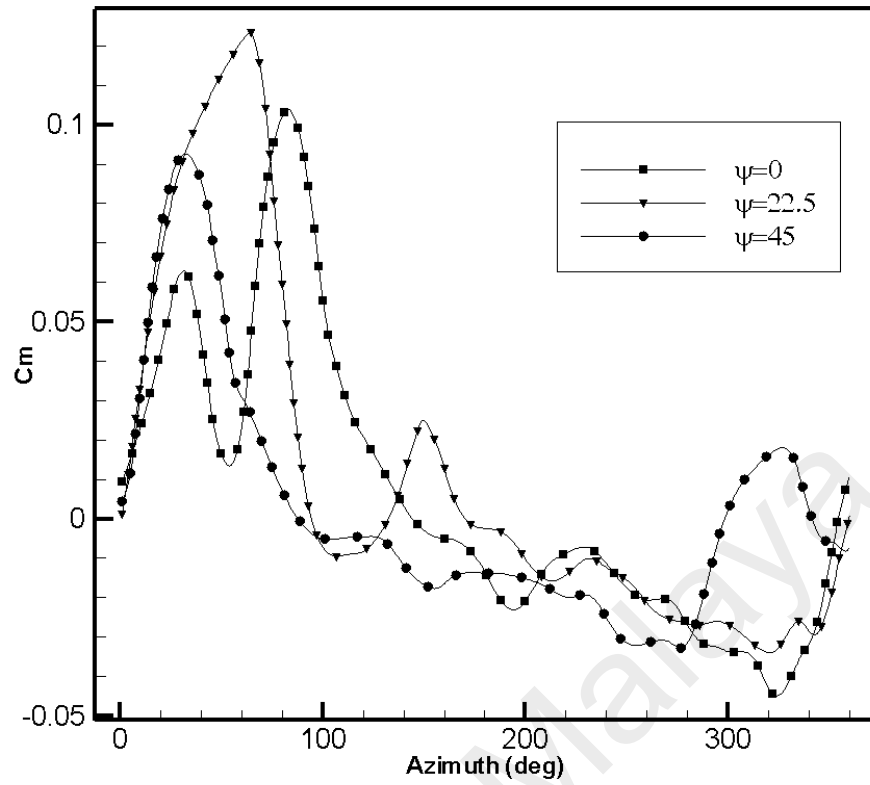


Figure 4.41: C_m vs. azimuth in #G.V=5 at different flow angles, TSR=0.8.

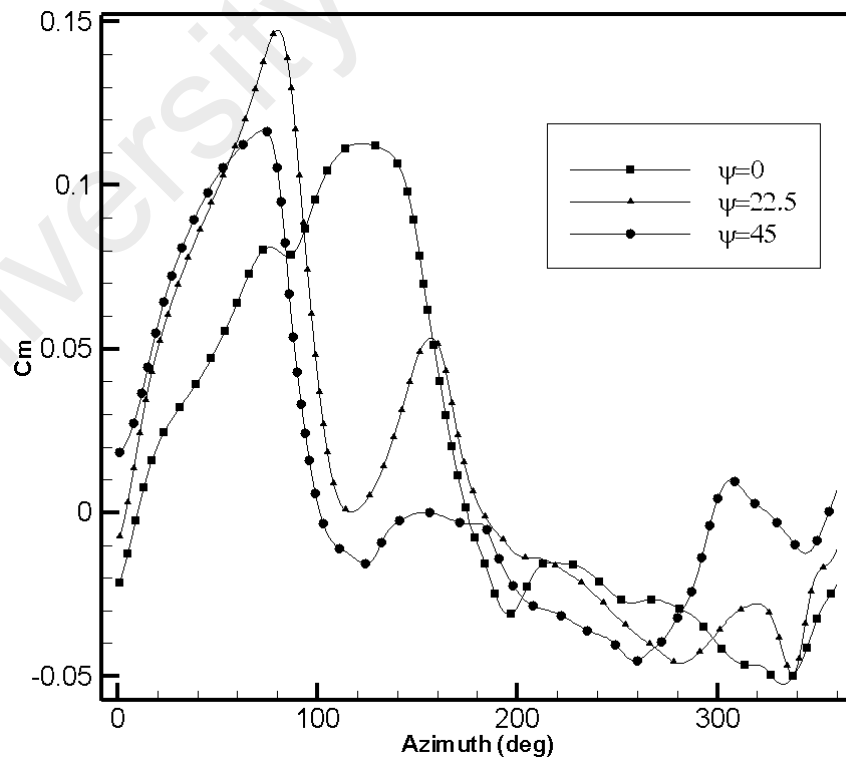


Figure 4.42: C_m vs. azimuth in #G.V=5 at different flow angles, TSR=1.2.

At TSR= 1.2, the same trend of the C_m is noted at the azimuth angle in the range of 0° to 100° at $\psi = 22.5$ and $\psi = 45^\circ$. At the azimuth angle between 120° and 180° , at flow angle = 22.5° higher C_m can be reported compared to $\psi = 45$. 26% of positive improvement of the C_p using the five bladed ODGV was detected at $\psi = 0$. Overall, the five bladed ODGV can only help to improve the performance on the VAWT in a directional flow angle or when the flow angle is zero.

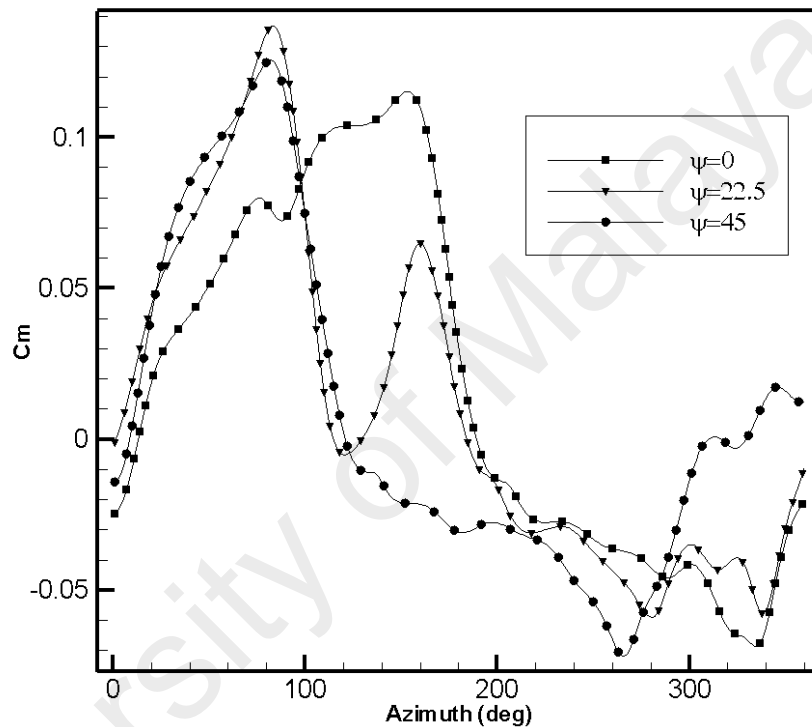


Figure 4.43: C_m vs. azimuth in #G.V=5 at different flow angles, TSR=1.6.

The highest performance of five bladed ODGV at TSR=1.6 is captured at the lowest flow angle. At this TSR, using the five bladed ODGV showed a 30% improvement in C_p compared to the open rotor. In addition, a negative effect of this kind of ODGV was noticed at $\psi = 45^\circ$ with a 17% reduction on the C_p compared to the open rotor.

4.6.2.3 Visualization of the Augmented VAWT with Four Bladed ODGV

The vorticity contour in the shrouded VAWT with a five bladed ODGV was presented in Figure 4.44. A negative impact of using ODGV occurred at $TSR = 0.8$. However, this negative impact had the lowest amount during $\psi = 22.5^\circ$. As it seen in the vorticity region, it is uniform and very small in this flow angle. At $TSR = 1.2$, $\psi = 0^\circ$ has the lowest vorticity compared to the $\psi = 22.5^\circ$ and $\psi = 45^\circ$. At $TSR = 1.2$ when the flow angle is zero, the VAWT achieved its highest performance. Negative impact of using five bladed ODGV can be reported at $\psi = 45^\circ$ at the same TSR . At this TSR , a very high vorticity zone was captured on the upper surface of blade three.

University of Malaysia

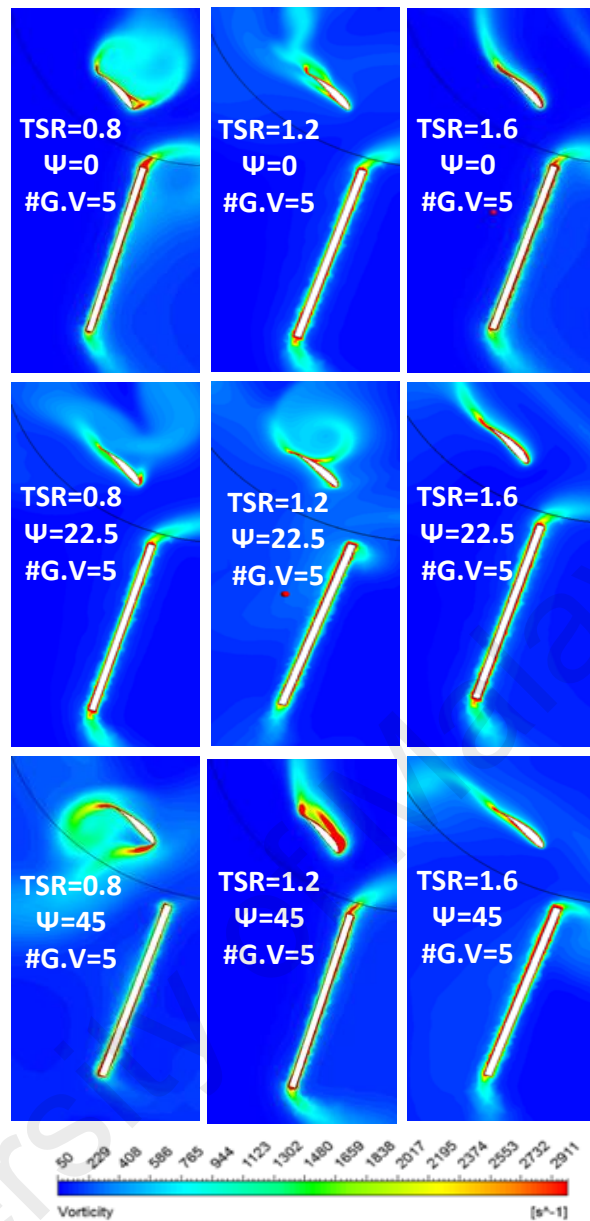


Figure 4.44: Vorticity contour in #G.V=5 around blade number3.

4.6.3 ODGV with Six Bladed Guide Vanes

4.6.3.1 Power Coefficient of the Augmented VAWT with Six Bladed ODGV

Between the three types of the ODGV's (with 4, 5 and 6 bladed guide vanes), the six bladed ODGV has the best performance at almost all flow angles as seen in Figure 4.45 and Figure 4.46 except four bladed guide vane performance at TSR=0.8. In this type of ODGV except at $\psi = 22.5^\circ$, the TSR = 0.8 where there is the six bladed ODGV has a very good improvement in C_p . Considering the symmetrical shape of the six bladed ODGV, differences of the predicted C_p between $\psi = 0^\circ$ and $\psi = 45^\circ$ are very

low. However, the highest amount of the C_p was 0.1153 by using this ODGV at $TSR = 1.2$ at $\psi = 0^\circ$. In this configuration, the six bladed ODGV showed a 36% improvement compare to the open rotor. The highest performance of this ODGV is at $TSR=1.6$ when $\psi = 0^\circ$ or $\psi = 45^\circ$ with a 40% improvement of the C_p .

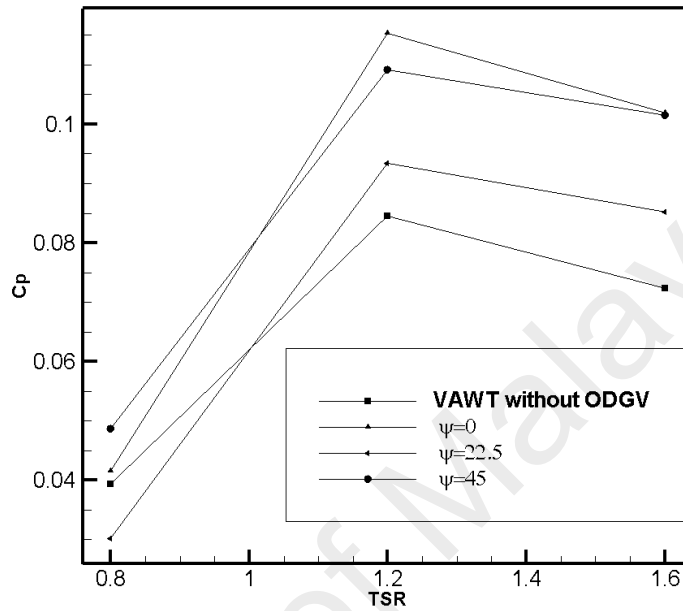


Figure 4.45: C_p vs. TSR in #G.V=6 at different flow angles.

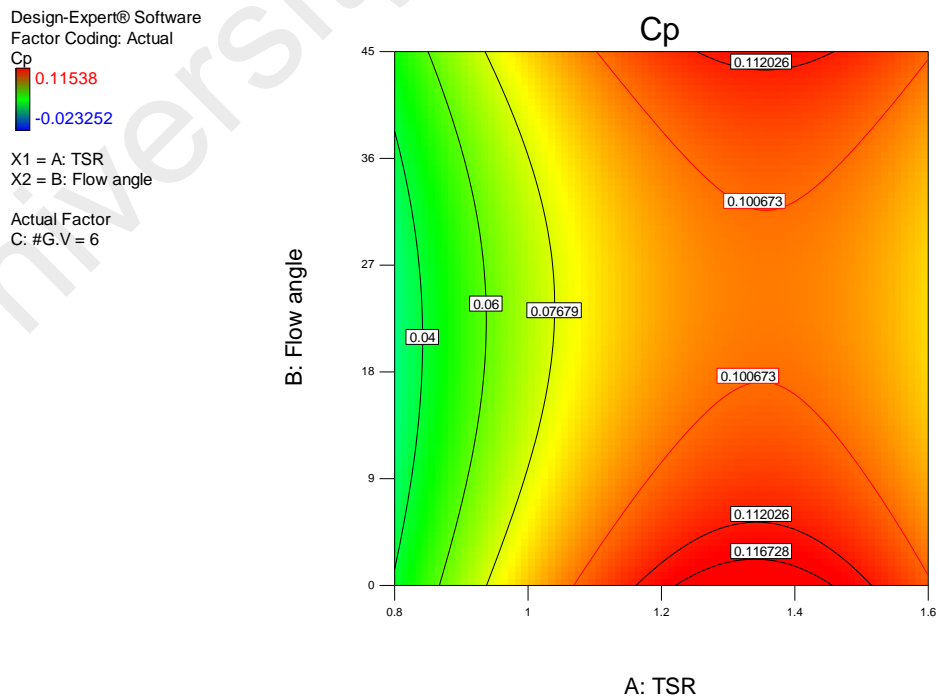


Figure 4.46: Variation of the C_p at different TSR and flow angles in #GV=6.

Same as the previous guide vanes, the coefficient of the torque of the VAWT with the integration of the six bladed guide vane is shown in following three figures.

4.6.3.2 Torque Coefficient of the Augmented VAWT with Six Bladed ODGV

Figure 4.47 shows the C_m generation in one rotation of the augmented VAWT with six-blade ODGV when $TSR=0.8$ at different flow angles. At this TSR , using this type of ODGV has a positive effect on the generation of the C_m at all ranges of the flow angles except when $\psi = 22.5^\circ$. At the flow angle, a 22.5° negative effect of using the six bladed guide vane was noticed with a 23% decrease in the C_p compared to the open rotor turbine. This kind of ODGV showed a 5% and 23% improvement in the C_p at $\psi = 0^\circ$ and $\psi = 45^\circ$ respectively.

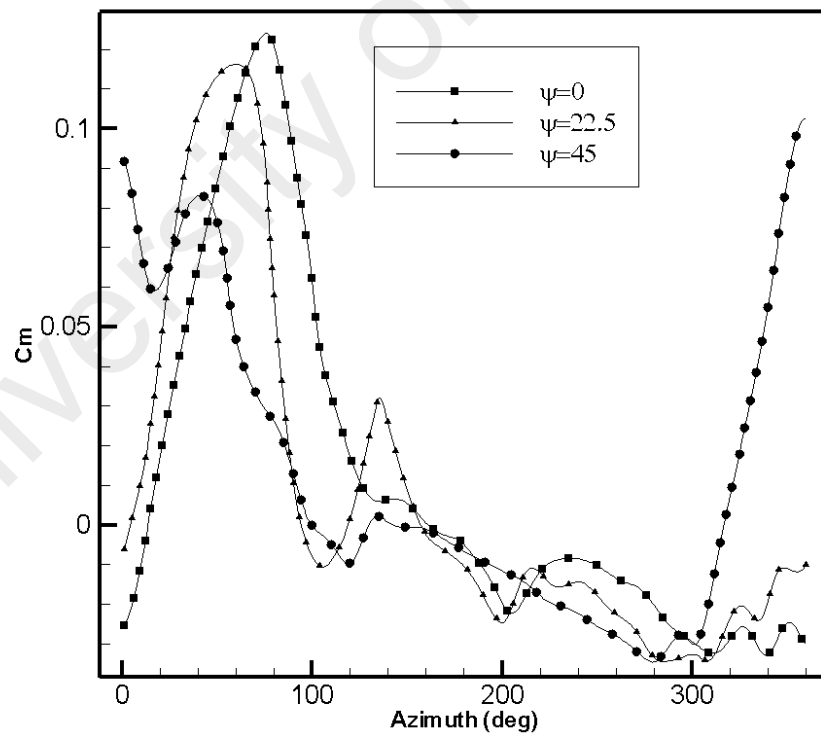


Figure 4.47: C_m vs. azimuth in #G.V=6 at different flow angles, $TSR=0.8$.

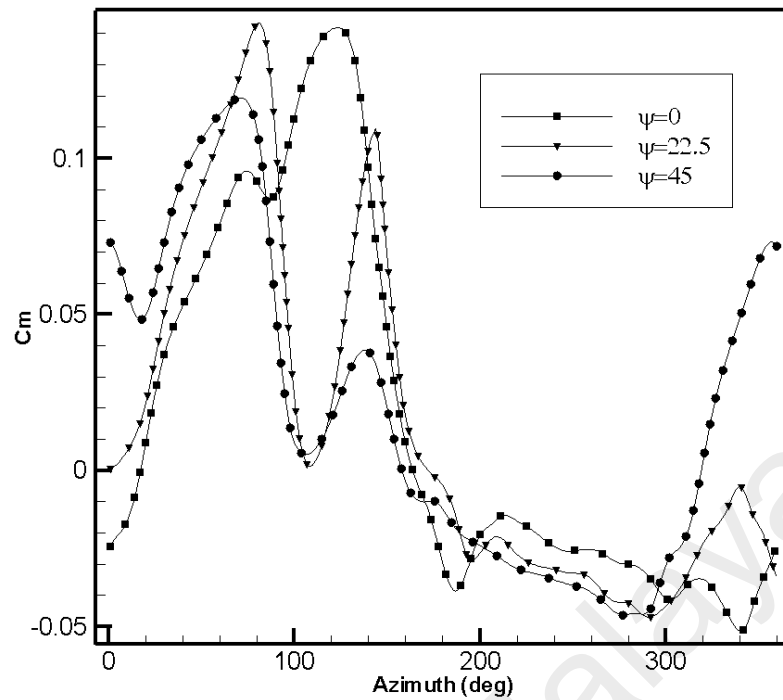


Figure 4.48: C_m vs. azimuth in #G.V=6 at different flow angle, TSR=1.2.

At TSR = 1.2, using the ODGV with the six bladed guide vane helps to improve the performance of the VAWT at all ranges of the flow angles (see Figure 4.48). Similar to the five bladed guide vane ODGV, the highest C_p was observed at the flow angle = 0° (36% improvement). The peak of the C_m at this flow angle can be reported when the azimuth angle = 130 degrees. In addition, the lowest effect of this ODGV occurred at $\psi = 22.5^\circ$; with a 10% improvement of the C_p .

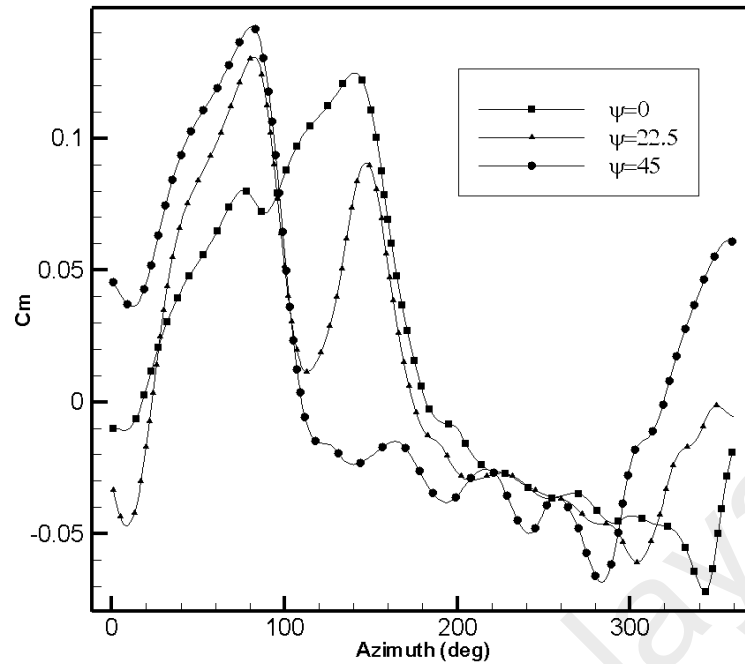


Figure 4.49: C_m vs. azimuth in #G.V=6 at different flow angle, TSR=1.6.

Variations of the C_m versus the azimuth angle in one rotation at different flow angles in TSR = 1.6 for the six bladed guide vane is illustrated in Figure 4.49. The overall average of the C_m between $\psi = 0^\circ$ and $\psi = 45^\circ$ shows almost the same amount. In these two flow angles, a 40% improvement of the C_p was noted. Also for $\psi = 22.5^\circ$, a 17% improvement of the C_p was achieved.

4.6.3.3 Visualization of the Augmented VAWT with Six Bladed ODGV

Figure 4.50 shows the vorticity contour in an augmented VAWT with a six bladed ODGV at different flow angles. As mentioned in Figure 4.45, the lowest effect of the six bladed ODGV on the VAWT performance was achieved during the flow angle of 22.5° . This phenomenon can be illustrated by using the vorticity contour such as below. At flow angle equal to 22.5° The highest amount of vorticity was captured by the CFD simulation compared to the reset flow angles.

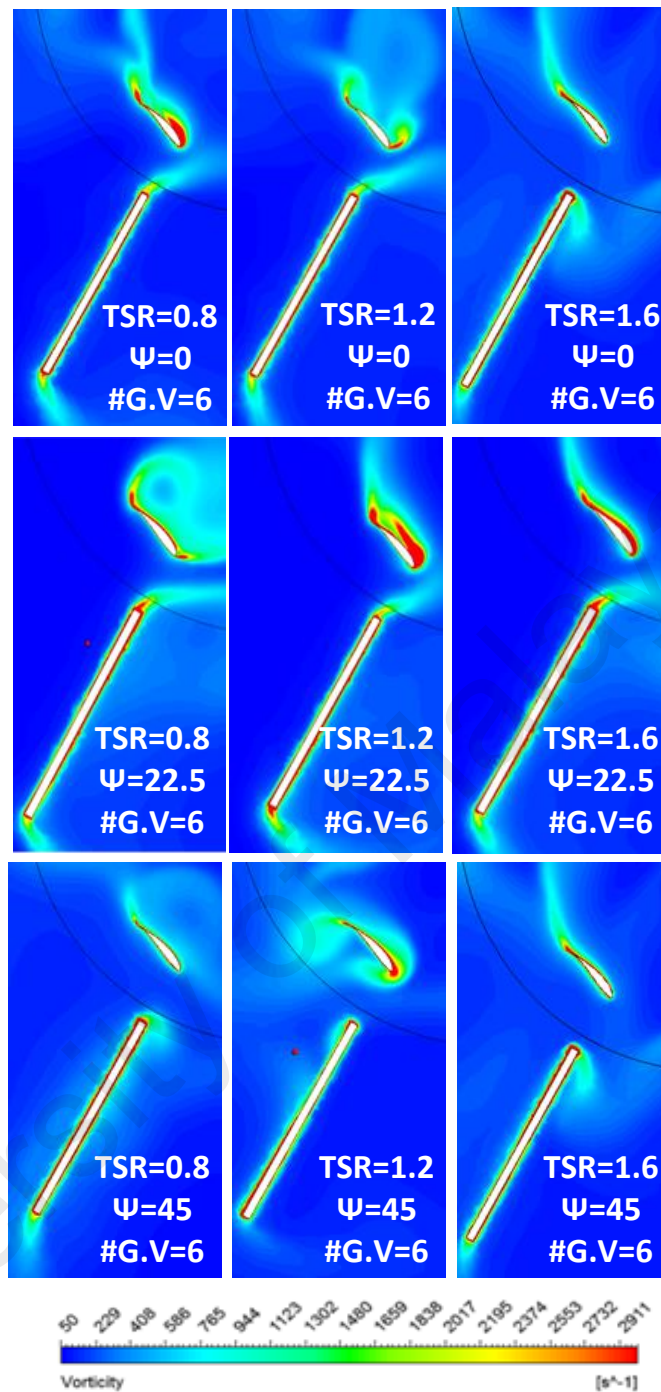


Figure 4.50: Vorticity contour at #G.V=6 around blade number3.

The six bladed ODGV shows almost same results for vorticity during $\psi=0^\circ$ and $\psi=45^\circ$ at TSR=1.6. However, at TSR=0.8, $\psi=45^\circ$ shows positive effect compare to the $\psi=0^\circ$ and $\psi=22.5^\circ$. Same as the other ODGVs this configuration also shows that the best performance of the ODGV is during $\psi = 0^\circ$.

4.6.4 Comparison between Optimized and Conventional ODGV's

In this section, *optimized ODGV* is compared to the mentioned 4, 5 and 6 bladed ODGVs. Three different flow angles and three different TSRs were investigated. Results of this section are plotted Figure 4.51, Figure 4.52 and Figure 4.53. Configuration of the optimized ODGV is shown in Table 4.3.

Table 4.3: Optimized ODGV configuration.

name	Outer diameter	Number of guide vanes	Guide vane angles
<i>Optimized ODGV</i>	1273mm	8	$\beta=20^\circ$ and $\alpha=55^\circ$

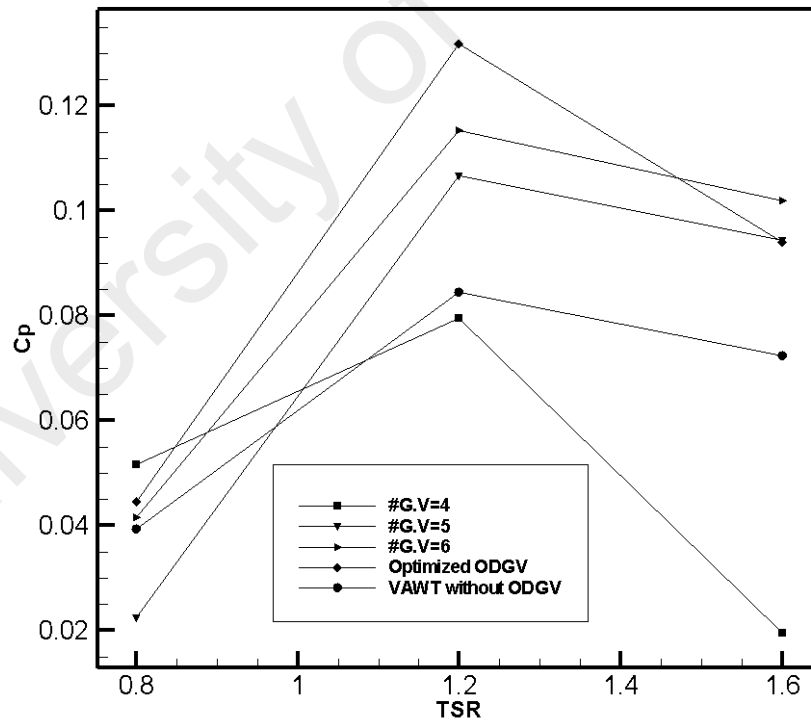


Figure 4.51: C_p vs. TSR using different ODGV numbers at $\psi=0^\circ$.

Figure 4.51 shows a comparison between the C_p versus the TSR for four different kinds of ODGVs when the flow angle equals to zero. The highest C_p was achieved by using the optimized ODGV at TSR = 1.2. At this TSR, the C_p was increased up to 0.13

compared to the open rotor at the same TSR. At low TSRs, our optimized ODGVs also showed a 12% enhancement of the C_p at TSR = 0.8. The highest improvements of the ODGV at TSR = 0.8 was detected but by using the four bladed guide vane at $\psi = 0^\circ$. At the TSR = 1.6, the six bladed guide vane showed better results of the improvements of the C_p compared to the rest of the other ODGV's. The optimized ODGV showed the same results as the five bladed guide vanes ODGV at this TSR with a 30% enhancement of the C_p .

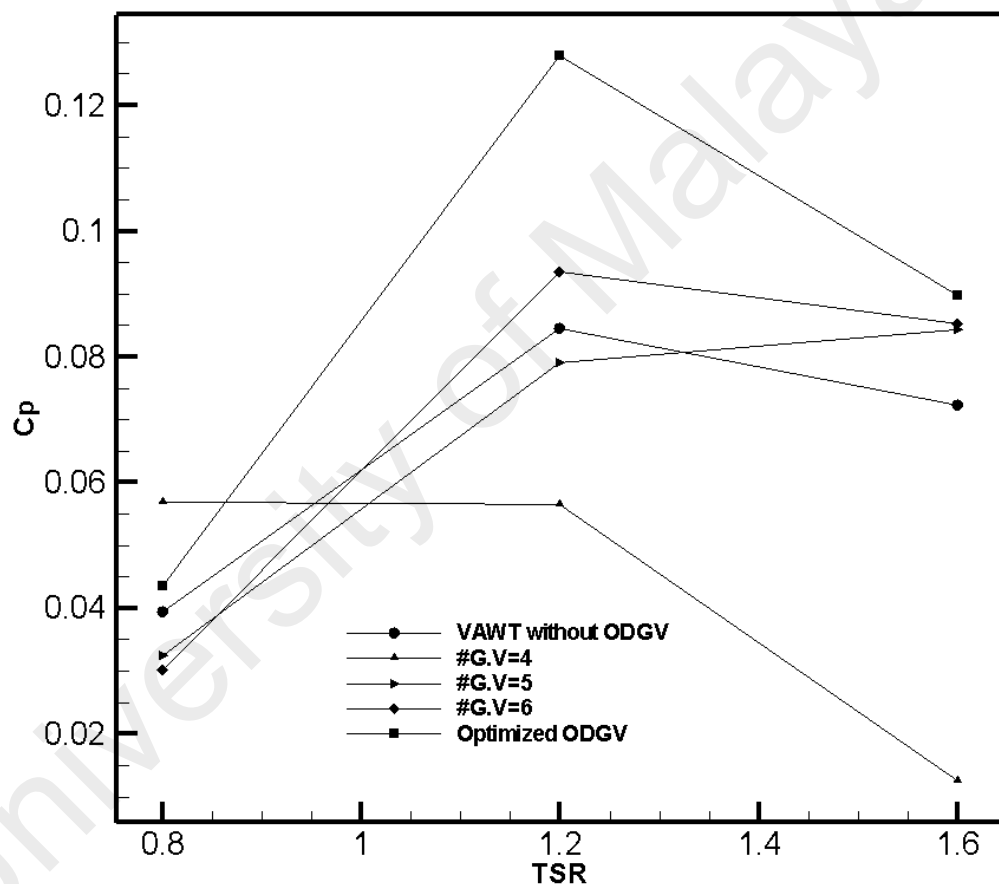


Figure 4.52: C_p vs. TSR using different ODGV number at $\psi=22.5^\circ$.

At $\psi = 22.5^\circ$ except at TSR=0.8, the optimized ODGV showed a better performance compared to the others. At TSR = 0.8, the best ODGV was the four bladed with a 44% improvement on the C_p . At this TSR, the optimized ODGV showed a 10% improvement in the C_p compared to the open rotor case. At TSR = 1.2, a very good improvement of the C_p was detected using the optimized ODGV with a 51%

enhancement in the C_p . This amount is 5% less than the enhancement of the optimized ODGV at $\psi = 0^\circ$. Finally, same as the $TSR = 1.2$, at $TSR = 1.6$ also optimized ODGV improves the C_p of the VAWT up to 25% compare to the open rotor VAWT.

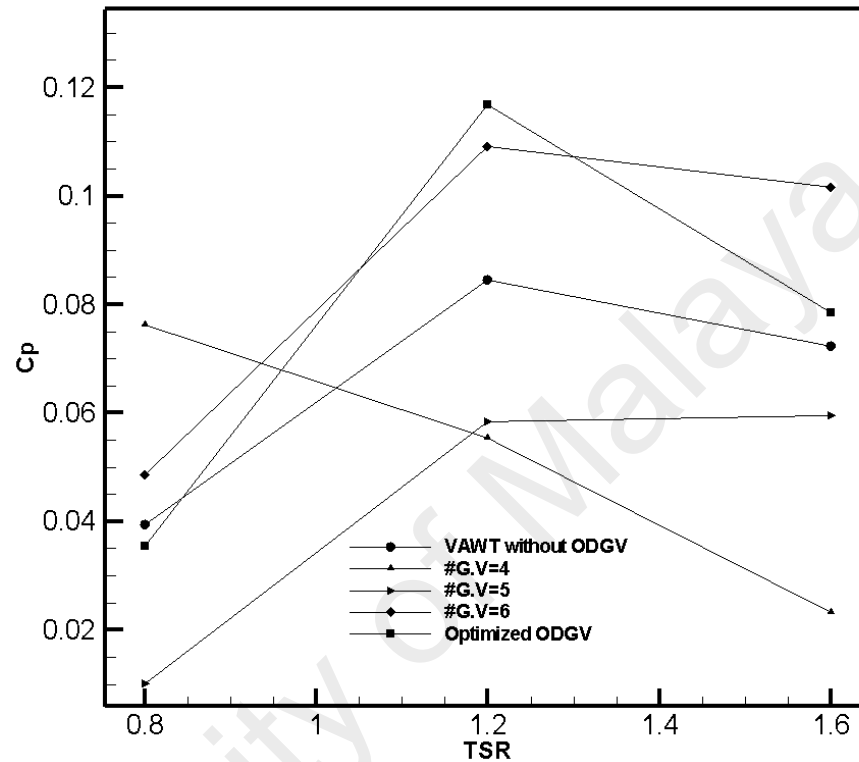


Figure 4.53: C_p vs. TSR using different ODGV number at $\psi=45^\circ$.

At $\psi = 45^\circ$, the optimized ODGV has the better results compared to the other ODGVs at $TSR=1.2$. At this TSR , the optimized ODGV showed a 38% improvement in the C_p . As seen, increasing the flow angle led to the decrease of the performance of the ODGV. At $TSR = 1.6$ and $\psi = 45^\circ$, the optimized ODGV showed an 8% improvement in the C_p while in the same conditions, the six bladed ODGV can enhance the C_p to up to 40%. The overall performance of the ODGVs is highly dependent on the flow angle. However, only the optimized and the six bladed guide vane can survive from a high flow angle. Between these two types of ODGVs, the optimized ODGV showed higher amount of maximum C_p at the ranges of the $TSRs$.

4.7 RESULTS OF THE LAB TEST

In order to validate the optimized performance of the ODGV, five different cases were tested via lab test. In the first step, the bare VAWT was tested. In the next step, the performance of the optimized ODGV was compared to the open rotor and three conventional ODGVs with four, five and six-bladed guide vanes. Results showed a good agreement in terms of the trends and values. It was shown that the optimized ODGV have the highest positive effect on the power generation on the VAWT.

4.7.1 Open Rotor Case

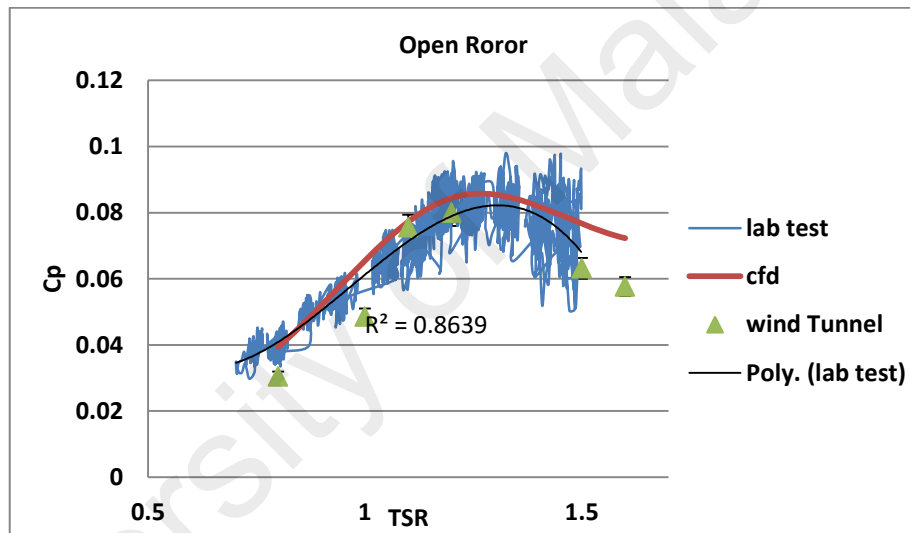


Figure 4.54: Validation of the lab test with wind tunnel.

Figure 4.54 shows the variation of the power coefficient at different TSRs with three types of data. A red line shows the results of the CFD which was discussed in the previous chapter. Green dots shows the results of the wind tunnel and the blue line shows the results of the open rotor performance in a lab test. The reason for using the lab test instead of the wind tunnel is due to the fact that air blown from the fan will perform in a similar manner to the field environment where the wind stream is turbulent and swirling. However, in this test, the error bar is higher than the wind tunnel testing. However, after averaging the output data in each loading, a good agreement in terms of

the shape and trend between the CFD and the experimental data was achieved. This graph shows that our numerical case correctly captures the flow behaviour and torque generation in the VAWT at different TSRs. It is shown that in higher TSRs, the lab test is rather unstable to predict the results. The maximum C_p is 0.082 at $TSR = 1.186$ during the lab test for the open rotor case which shows a 3% deviation compare to the CFD simulation with 0.084.

4.7.2 Augmented Turbine Cases

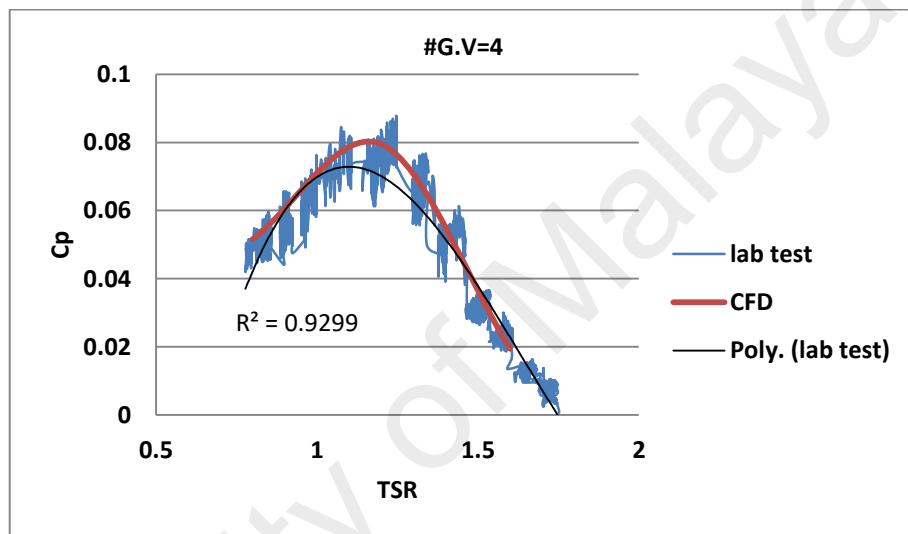


Figure 4.55: C_p vs. TSR in lab test and CFD while #G.V=4.

Results of the lab test during the use of the ODGV with the four bladed guide vane is illustrated in Figure 4.55. There is a good agreement between the CFD and the lab test can be reported in this graph. As it can be seen at the high C_p during the TSR between 1 and 1.3, the lab test shows a lower value compared to the CFD simulation. At $TSR = 1.2$, the C_p in the CFD simulation was 0.0794, while in lab test it is 0.0736 where it is 7% lower than the CFD simulation.

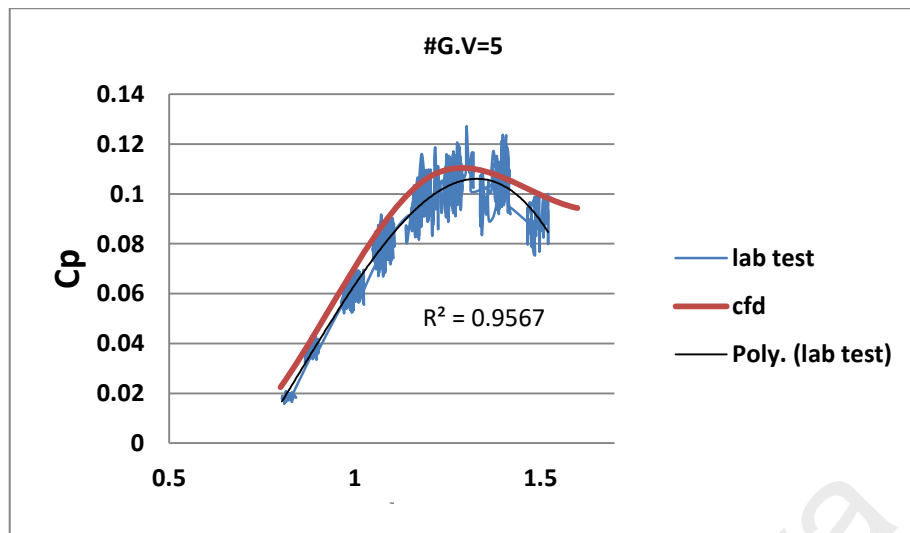


Figure 4.56: C_p vs. TSR in lab test and CFD while #G.V=5.

Same as the previous graph, Figure 4.56 shows a performance graph of the VAWT when it is augmented with the five bladed ODGV. The red line shows the results of the CFD and the blue line presents the lab test results. In this ODGV, the configuration comparison shows that in lower TSRs, the CFD is matched better with the lab test compared to the higher TSRs. The lowest error can be reported in TSR = 0.8, and the highest error is in TSR = 1.6 with a 10% and 25% difference respectively.

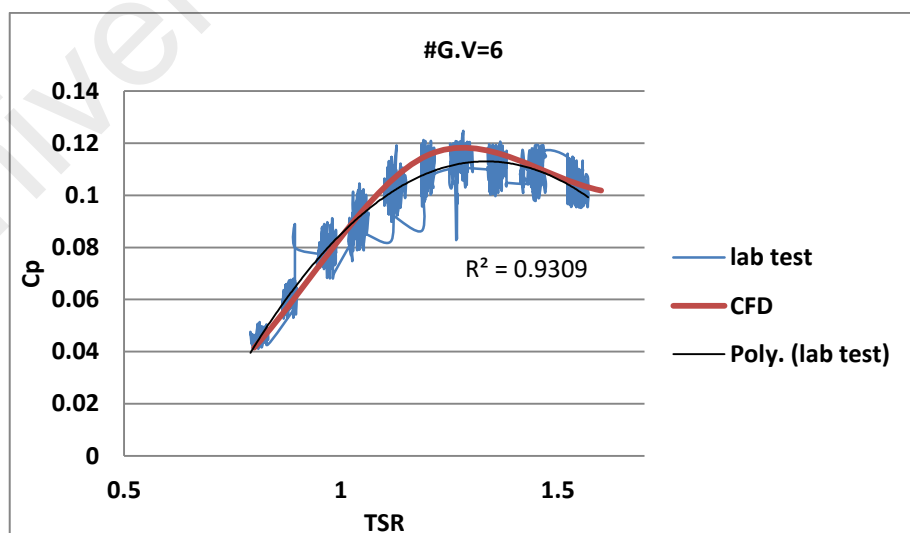


Figure 4.57: C_p Vs. TSR in lab test and CFD while #G.V=6.

A lower prediction of the C_p reported in TSRs smaller than the one in the CFD simulation of the VAWT augmented with the six-bladed guide vane. This result is shown in Figure 4.57. However, the best agreement between the CFD and the lab test was achieved in this configuration. In addition, fluctuation of the lab test results for the C_p is much lower than the other configurations.

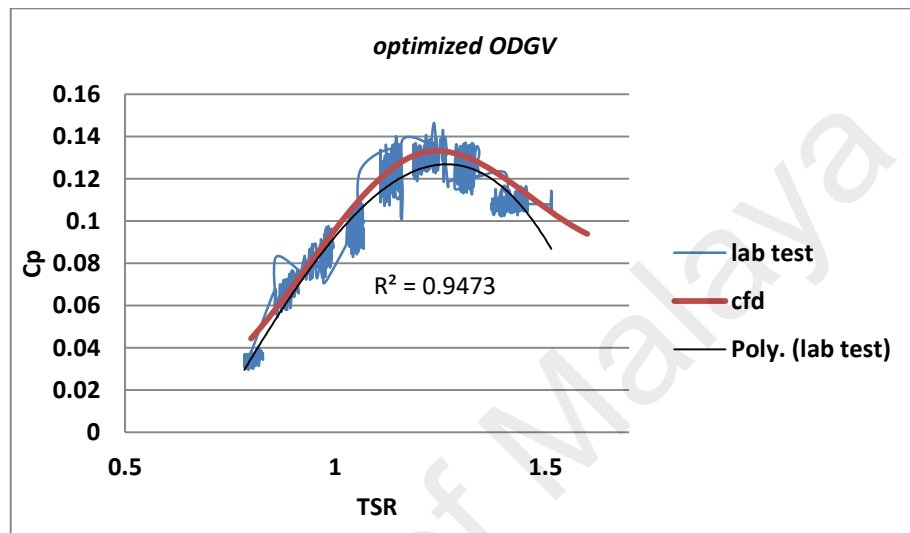


Figure 4.58: C_p vs. TSR in lab test and CFD in *OPT.* ODGV.

Finally, in the last step, *optimized ODGV* is tested in the lab test (see Figure 4.58). As it predicted, in a CFD simulation, this ODGV helps improve the output power in the VAWT significantly. A very good agreement between the CFD and the lab test can be reported by a comparison between these two tests. In this configuration, the CFD shows a better match with experimental data, while the TSR is lower than one.

4.8 SUMMARY

CFD simulation and lab tests have been done on the augmented and open rotor wind turbine. Numerical optimization based on coupling two software which are design expert and CFD software, fluent showed that using shape ratio of $R=0.55$ on augmented rotor with angles of the $\alpha=55\text{deg}$ and $\beta=20\text{deg}$, coefficient of the power in the VAWT is significantly increased and its reached up to 55% improvements. In addition, it was

found that by comparing the results of the CFD simulation for optimized ODGV with conventional 4,5and 6 bladed ODGV, it has higher performance and it was less sensitive to the inlet flow angle. Results of the lab test concluded that the CFD simulation was accurate and same results from lab test were calculated.

University of Malaya

CHAPTER 5: CONCLUSION AND RECOMMENDATION

CFD has been a useful modeling tool for analyzing the performance of a wind turbine. It is an inexpensive and effective method of simulating and testing a large number of models that cannot be readily examined in a wind tunnel.

In this dissertation, we used the Computational Fluid Dynamics (CFD) to present the effects of the Omni direction-guide-vane on the performance of a vertical axis wind turbine (VAWT). For this purpose, a five straight-bladed VAWT was simulated via computational fluid dynamics (CFD). Hence, the VAWT without the ODGV covering was simulated and validated via the experimental fluid dynamics (EFD) data. Grid and time step independency test as well as the effect of the domain size and turbulence model were also conducted. In the next step, the VAWT was shrouded by the ODGV cover and simulated in different shapes and angle conditions. The ODGV's outer diameter and angles were optimized using the coupling of the CFD and RSM methods. Results of this study indicated that the output power of the VAWT with $\alpha = 55^\circ$ and $\beta=20^\circ$ ODGV guide vanes angles were improved by 12%, 56% and 29% respectively at three different TSRs including 0.8, 1.2 and 1.6. In addition, based on these results, all the shape ratios showed improvements in power coefficient, where the best case has a shape ratio of 0.55. This improves the power coefficient by 56% and the torque coefficient to up to 55%. In the final steps, the results of the optimized ODGV was compared with three different types of the guide vanes at different flow angles. Results showed that the optimized ODGV has the best improvement in terms of the performance of the VAWT compared to the 4,5,6 bladed ODGV's. The optimized ODGV also showed that it is not very sensitive to the different flow angles. The optimized ODGV was also fabricated and tested in lab test conditions to validate the

numerical findings. Good agreements in terms of the values and trends were achieved in comparison between the CFD and lab test data.

5.1 SUGGESTIONS FOR FURTHER RESEARCH

This energy conversion device is highly efficient in its ability to operate under low or high wind operating conditions. We encourage its commercialization especially in cities. Its scalable size favors installation on building rooftops. I strongly believe further optimizing on the VAWT that will boost its power output. Future research in this subject is very important. Recommendations listed below are focused on enhancing the performance features, modeling methods and other validation work for the VAWT.

- This study is focused on the optimization of the ODGV. It is recommended that optimizing the VAWT also makes a very good impact on the performance of the whole system.
- Effect of the optimized ODGV can be tested in real urban areas.
- Economic impact of the use of the optimized ODGV can be studied in future researches.
- A fully developed 3-D CFD modelling of the whole system needs very large computational requirements. These models can be studied in high performance or cloud computer labs.
- One of the disadvantages of using the diffuser is that the overall weight of the structure is increased. Furthermore, use of the diffuser makes the design more complicated. Hence, this issue can be studied in future researches.

REFERENCES

- Abe, K., Nishida, M., Sakurai, A., Ohya, Y., Kihara, H., Wada, E., & Sato, K. (2005). Experimental and numerical investigations of flow fields behind a small wind turbine with a flanged diffuser. *Journal of Wind Engineering and Industrial Aerodynamics*, 93(12), 951-970.
- Akwa, J.V., Vielmo, H.A., & Petry, A.P. (2012). A review on the performance of savonius wind turbines. *Renewable and Sustainable Energy Reviews*, 16(5), 3054-3064.
- Alaimo, A., Esposito, A., Messineo, A., Orlando, C., & Tumino, D. (2015). 3d cfd analysis of a vertical axis wind turbine. *Energies*, 8(4), 3013-3033.
- Almohammadi, K.M., Ingham, D.B., Ma, L., & Pourkashan, M. (2013). Computational fluid dynamics (cfd) mesh independency techniques for a straight blade vertical axis wind turbine. *Energy*, 58(0), 483-493.
- Altan, B.D., & Atılgan, M. (2008). An experimental and numerical study on the improvement of the performance of savonius wind rotor. *Energy Conversion and Management*, 49(12), 3425-3432.
- Amet, E., Mažžtre, T., Pellone, C., & Achard, J.-L. (2009). 2d numerical simulations of blade-vortex interaction in a darrieus turbine. *Journal of fluids engineering*, 131(11), 111103.
- Armstrong, S., Fiedler, A., & Tullis, S. (2012). Flow separation on a high reynolds number, high solidity vertical axis wind turbine with straight and canted blades and canted blades with fences. *Renewable Energy*, 41(0), 13-22.
- Beri, H., & Yao, Y. (2011). Effect of camber airfoil on self starting of vertical axis wind turbine. *Journal of environmental Science and Technology*, 4(3), 302-312.
- Bhuyan, S., & Biswas, A. (2014). Investigations on self-starting and performance characteristics of simple h and hybrid h-savonius vertical axis wind rotors. *Energy Conversion and Management*, 87, 859-867.
- Butbul, J., MacPhee, D., & Beyene, A. (2015). The impact of inertial forces on morphing wind turbine blade in vertical axis configuration. *Energy Conversion and Management*, 91, 54-62.
- C Montgomery, D. (1997). Montgomery design and analysis of experiments.

- Castelli, M.R., Ardizzon, G., Battisti, L., Benini, E., & Pavesi, G. (2010). *Modeling strategy and numerical validation for a darrieus vertical axis micro-wind turbine*. Paper presented at the ASME 2010 International Mechanical Engineering Congress and Exposition.
- Chen, C.-C., & Kuo, C.-H. (2013). Effects of pitch angle and blade camber on flow characteristics and performance of small-size darrieus vawt. *Journal of Visualization*, 16(1), 65-74.
- Chong, W., Fazlizan, A., Poh, S., Pan, K., Hew, W., & Hsiao, F. (2013). The design, simulation and testing of an urban vertical axis wind turbine with the omnidirection-guide-vane. *Applied Energy*, 112, 601-609.
- Chong, W., Fazlizan, A., Poh, S., Pan, K., & Ping, H. (2012). Early development of an innovative building integrated wind, solar and rain water harvester for urban high rise application. *Energy and Buildings*, 47, 201-207.
- Chong, W., Gwani, M., Shamsirband, S., Muzammil, W., Tan, C., Fazlizan, A., . . . Wong, K. (2016). Application of adaptive neuro-fuzzy methodology for performance investigation of a power-augmented vertical axis wind turbine. *Energy*, 102, 630-636.
- Chong, W., Naghavi, M., Poh, S., Mahlia, T., & Pan, K. (2011). Techno-economic analysis of a wind-solar hybrid renewable energy system with rainwater collection feature for urban high-rise application. *Applied Energy*, 88(11), 4067-4077.
- Chong, W.T., Pan, K.C., Poh, S.C., Fazlizan, A., Oon, C.S., Badarudin, A., & Nik-Ghazali, N. (2013). Performance investigation of a power augmented vertical axis wind turbine for urban high-rise application. *Renewable Energy*, 51(0), 388-397.
- Consul, C., Willden, R., Ferrer, E., & McCulloch, M. (2009). *Influence of solidity on the performance of a cross-flow turbine*. Paper presented at the Proceedings of the 8th European Wave and Tidal Energy Conference., Uppsala, Sweden.
- Cooper, P., & Kennedy, O.C. (2004). Development and analysis of a novel vertical axis wind turbine.
- Dai, Y., & Lam, W. (2009). Numerical study of straight-bladed darrieus-type tidal turbine. *Proceedings of the ICE-Energy*, 162(2), 67-76.
- Danao, L.A., Edwards, J., Eboibi, O., & Howell, R. (2014). A numerical investigation into the influence of unsteady wind on the performance and aerodynamics of a vertical axis wind turbine. *Applied Energy*, 116(0), 111-124.

- Danao, L.A., & Howell, R. (2012). *Effects on the performance of vertical axis wind turbines with unsteady wind inflow: A numerical study*. Paper presented at the 50th AIAA aerospace sciences meeting including the new horizons forum and aerospace exposition, Nashville, TN, USA.
- Danao, L.A., Qin, N., & Howell, R. (2012). A numerical study of blade thickness and camber effects on vertical axis wind turbines. *Proceedings of the Institution of Mechanical Engineers, Part A: Journal of Power and Energy*, 0957650912454403.
- Devine-Wright, P. (2005). Beyond nimbyism: Towards an integrated framework for understanding public perceptions of wind energy. *Wind energy*, 8(2), 125-139.
- Doman, L.E., & Conti, J. (2010). International energy outlook report. *US Energy Information Administration, Washington, USA*, 10-20.
- Edwards, J., Durrani, N., Howell, R., & Qin, N. (2007). *Wind tunnel and numerical study of a small vertical axis wind turbine*. Paper presented at the 45th AIAA Aerospace Sciences Meeting and Exhibit, Reno, Nevada.
- Edwards, J.M., Danao, L.A., & Howell, R.J. (2012). Novel experimental power curve determination and computational methods for the performance analysis of vertical axis wind turbines. *Journal of Solar Energy Engineering*, 134(3), 031008.
- Elkhoury, M., Kiwata, T., & Aoun, E. (2015). Experimental and numerical investigation of a three-dimensional vertical-axis wind turbine with variable-pitch. *Journal of Wind Engineering and Industrial Aerodynamics*, 139, 111-123.
- Ferreira, C.S., Bijl, H., Van Bussel, G., & Van Kuik, G. (2007). *Simulating dynamic stall in a 2d vawt: Modeling strategy, verification and validation with particle image velocimetry data*. Paper presented at the Journal of physics: conference series.
- Ferreira, C.S., van Bussel, G., & Van Kuik, G. (2007a). *2d cfd simulation of dynamic stall on a vertical axis wind turbine: Verification and validation with piv measurements*. Paper presented at the 45th AIAA aerospace sciences meeting and exhibit.
- Ferreira, C.S., van Bussel, G., & Van Kuik, G. (2007b). *2d cfd simulation of dynamic stall on a vertical axis wind turbine: Verification and validation with piv measurements*. Paper presented at the 45th AIAA Aerospace Sciences Meeting and Exhibit/ASME Wind Energy Symposium.

- Ferreira, C.S., Van Zuijlen, A., Bijl, H., Van Bussel, G., & Van Kuik, G. (2010). Simulating dynamic stall in a two-dimensional vertical-axis wind turbine: Verification and validation with particle image velocimetry data. *Wind Energy*, 13(1), 1-17.
- Fluent, A. (2009). 12.0 theory guide. *Ansys Inc*, 5.
- Geurts, B., Simao Ferreira, C., & Van Bussel, G. *Aerodynamic analysis of a vertical axis wind turbine in a diffuser*. Paper presented at the 3rd EWEA Conference-Torque 2010: The Science of making Torque from Wind, Heraklion, Crete, Greece, 28-30 June 2010.
- Guerri, O., Sakout, A., & Bouhadeif, K. (2007). Simulations of the fluid flow around a rotating vertical axis wind turbine. *Wind Engineering*, 31(3), 149-163.
- Gupta, R., & Biswas, A. (2010). Computational fluid dynamics analysis of a twisted three-bladed h-darrieus rotor. *Journal of Renewable and Sustainable Energy*, 2(4), 043111.
- Hamada, K., Smith, T., Durrani, N., Qin, N., & Howell, R. (2008). *Unsteady flow simulation and dynamic stall around vertical axis wind turbine blades*. Paper presented at the 46th AIAA Aerospace Sciences Meeting and Exhibit, Reno, Nevada.
- Heymann, M. (1998). Signs of hubris: The shaping of wind technology styles in germany, denmark, and the united states, 1940-1990. *Technology and Culture*, 39(4), 641-670.
- Howell, R., Qin, N., Edwards, J., & Durrani, N. (2010). Wind tunnel and numerical study of a small vertical axis wind turbine. *Renewable Energy*, 35(2), 412-422.
- Huang, S.-R., Ma, Y.-H., Chen, C.-F., Seki, K., & Aso, T. (2014). Theoretical and conditional monitoring of a small three-bladed vertical-axis micro-hydro turbine. *Energy Conversion and Management*, 86, 727-734.
- Igra, O. (1977). The shrouded aerogenerator. *Energy*, 2(4), 429-439.
- Igra, O. (1981). Research and development for shrouded wind turbines. *Energy Conversion and Management*, 21(1), 13-48.
- Iida, A., Mizuno, A., & Fukudome, K. (2004a). *Numerical simulation of aerodynamic noise radiated form vertical axis wind turbines*. Paper presented at the Proceedings of the 18 International Congress on Acoustics.

- Iida, A., Mizuno, A., & Fukudome, K. (2004b, 2004). *Numerical simulation of aerodynamic noise radiated from vertical axis wind turbines.*
- Islam, M., Ting, D.S.-K., & Fartaj, A. (2008). Aerodynamic models for darrieus-type straight-bladed vertical axis wind turbines. *Renewable and Sustainable Energy Reviews, 12*(4), 1087-1109.
- Ismail, M.F., & Vijayaraghavan, K. (2015). The effects of aerofoil profile modification on a vertical axis wind turbine performance. *Energy, 80*, 20-31.
- Jha, A.R. (2011). *Wind turbine technology*: CRC Press.
- Khuri, A.I., & Mukhopadhyay, S. (2010). Response surface methodology. *Wiley Interdisciplinary Reviews: Computational Statistics, 2*(2), 128-149.
- Kirke, B. (2005). Developments in ducted water current turbines. Tidal paper 16-08-03 1.
- Kosasih, P., Bryce, N., Tondelli, A., & Beazley, A. (2012). Experimental study of the performance of bare and nozzle–diffuser shrouded micro wind turbine under axial and non-axial inflow condition.
- Laneville, A., & Vittecoq, P. (1986). Dynamic stall: The case of the vertical axis wind turbine. *Journal of Solar Energy Engineering, 108*(2), 140-145.
- Lauder, B.E., & Spalding, D. (1974). The numerical computation of turbulent flows. *Computer methods in applied mechanics and engineering, 3*(2), 269-289.
- Lee, T., & Gerontakos, P. (2004). Investigation of flow over an oscillating airfoil. *Journal of Fluid Mechanics, 512*, 313-341.
- Li, Q.a., Maeda, T., Kamada, Y., Murata, J., Kawabata, T., Shimizu, K., . . . Kasuya, T. (2016). Wind tunnel and numerical study of a straight-bladed vertical axis wind turbine in three-dimensional analysis (part i: For predicting aerodynamic loads and performance). *Energy, 106*, 443-452.
- Maître, T., Amet, E., & Pellone, C. (2013). Modeling of the flow in a darrieus water turbine: Wall grid refinement analysis and comparison with experiments. *Renewable Energy, 51*, 497-512.
- Mann, J. (1998). Wind field simulation. *Probabilistic engineering mechanics, 13*(4), 269-282.

- Manwell, J.F., McGowan, J.G., & Rogers, A.L. (2002). *Front matter and index*: Wiley Online Library.
- Martinat, G., Braza, M., Hoarau, Y., & Harran, G. (2008). Turbulence modelling of the flow past a pitching naca0012 airfoil at 105 and 106 reynolds numbers. *Journal of Fluids and Structures*, 24(8), 1294-1303.
- McCroskey, W. (1981). The phenomenon of dynamic stall: DTIC Document.
- McIntosh, S.C. (2009). *Wind energy for the built environment*. University of Cambridge.
- McIntosh, S.C., & Babinsky, H. (2012). Aerodynamic modeling of swept-bladed vertical axis wind turbines. *Journal of Propulsion and Power*, 29(1), 227-237.
- McLaren, K., Tullis, S., & Ziada, S. (2012). Computational fluid dynamics simulation of the aerodynamics of a high solidity, small-scale vertical axis wind turbine. *Wind Energy*, 15(3), 349-361.
- McLaren, K.W. (2011). A numerical and experimental study of unsteady loading of high solidity vertical axis wind turbines.
- Menter, F., Kuntz, M., & Langtry, R. (2003). Ten years of industrial experience with the sst turbulence model. *Turbulence, heat and mass transfer*, 4(1).
- Mertens, S., van Kuik, G., & van Bussel, G. (2003). Performance of an h-darrieus in the skewed flow on a roof. *Journal of Solar Energy Engineering*, 125(4), 433-440.
- Mohamed, M.H. (2012). Performance investigation of h-rotor darrieus turbine with new airfoil shapes. *Energy*, 47(1), 522-530.
- Mohamed, M.H., Ali, A.M., & Hafiz, A.A. (2015). Cfd analysis for h-rotor darrieus turbine as a low speed wind energy converter. *Engineering Science and Technology, an International Journal*(0).
- Nobile, R., Vahdati, M., Barlow, J., & Mewburn-Crook, A. (2011). Dynamic stall for a vertical axis wind turbine in a two-dimensional study. *World Renew. Energ. Congr*, 4225-4232.
- Nobile, R., Vahdati, M., Barlow, J.F., & Mewburn-Crook, A. (2014). Unsteady flow simulation of a vertical axis augmented wind turbine: A two-dimensional study. *Journal of Wind Engineering and Industrial Aerodynamics*, 125(0), 168-179.

- Noordin, M.Y., Venkatesh, V.C., Sharif, S., Elting, S., & Abdullah, A. (2004). Application of response surface methodology in describing the performance of coated carbide tools when turning aisi 1045 steel. *Journal of Materials Processing Technology*, 145(1), 46-58.
- Oehlert, G.W. (2000). Design and analysis of experiments: Response surface design. *New York*.
- Ohya, Y., Karasudani, T., Sakurai, A., Abe, K.-i., & Inoue, M. (2008). Development of a shrouded wind turbine with a flanged diffuser. *Journal of wind engineering and industrial aerodynamics*, 96(5), 524-539.
- Panwar, N., Kaushik, S., & Kothari, S. (2011). Role of renewable energy sources in environmental protection: A review. *Renewable and Sustainable Energy Reviews*, 15(3), 1513-1524.
- Passel, J.S., Cohn, D.V., Agarwal, S., Srivastava, A., Choudhary, B., Kaushik, S., . . . Banoba, P. (2007). Us population projections: 2005-2050. *MMWR. Morbidity and Mortality Weekly Report*, 56(48), 1257-1261.
- Patel, M.R. (1999). Wind and solar power systems. 1999: Boca Raton [Fla.]: CRC Press.
- Pope, K., Rodrigues, V., Doyle, R., Tsopelas, A., Gravelins, R., Naterer, G.F., & Tsang, E. (2010). Effects of stator vanes on power coefficients of a zephyr vertical axis wind turbine. *Renewable Energy*, 35(5), 1043-1051.
- Qin, N., Howell, R., Durrani, N., Hamada, K., & Smith, T. (2011). Unsteady flow simulation and dynamic stall behaviour of vertical axis wind turbine blades. *Wind Engineering*, 35(4), 511-528.
- Raciti Castelli, M., Dal Monte, A., Quaresimin, M., & Benini, E. (2013). Numerical evaluation of aerodynamic and inertial contributions to darrieus wind turbine blade deformation. *Renewable Energy*, 51(0), 101-112.
- Raciti Castelli, M., Englaro, A., & Benini, E. (2011). The darrieus wind turbine: Proposal for a new performance prediction model based on cfd. *Energy*, 36(8), 4919-4934.
- Razavykia, A., Farahany, S., & Yusof, N.M. (2015). Evaluation of cutting force and surface roughness in the dry turning of al-mg 2 si in-situ metal matrix composite inoculated with bismuth using doe approach. *Measurement*, 76, 170-182.

- Riegler, G. (1983). Principles of energy extraction from a free stream by means of wind turbines. *Wind Engineering*, 7, 115-126.
- Roa, A.M., Aumelas, V., Maître, T., & Pellone, C. (2010). *Numerical and experimental analysis of a darrieus-type cross flow water turbine in bare and shrouded configurations*. Paper presented at the IOP Conference Series: Earth and Environmental Science.
- Scheurich, F., Fletcher, T.M., & Brown, R.E. (2011). Simulating the aerodynamic performance and wake dynamics of a vertical-axis wind turbine. *Wind Energy*, 14(2), 159-177.
- Schlichting, H., & Gersten, K. (2003). *Boundary-layer theory*: Springer Science & Business Media.
- Shahzad, A., Asim, T., Mishra, R., & Paris, A. (2013). Performance of a vertical axis wind turbine under accelerating and decelerating flows. *Procedia CIRP*, 11, 311-316.
- Sheldahl, R.E., & Klimas, P.C. (1981). Aerodynamic characteristics of seven symmetrical airfoil sections through 180-degree angle of attack for use in aerodynamic analysis of vertical axis wind turbines: Sandia National Labs., Albuquerque, NM (USA).
- Takahashi, S., Hamada, J., & Takashi, Y. (2006). Numerical and experimental studies of airfoils suitable for vertical axis wind turbines and an application of wind-energy collecting structure for higher performance. *Journal of Wind Engineering*, 108, 327-330.
- Takao, M., Maeda, T., Kamada, Y., Oki, M., & Kuma, H. (2007). *A straight-bladed vertical axis wind turbine with a directed guide vane row*. Paper presented at the ASME/JSME 2007 5th Joint Fluids Engineering Conference.
- Templin, R. (1974). Aerodynamic performance theory for the nrc vertical-axis wind turbine: National Aeronautical Establishment, Ottawa, Ontario (Canada).
- Tescione, G., Ragni, D., He, C., Ferreira, C.S., & van Bussel, G. (2014). Near wake flow analysis of a vertical axis wind turbine by stereoscopic particle image velocimetry. *Renewable Energy*, 70, 47-61.
- Trivellato, F., & Raciti Castelli, M. (2014). On the courant–friedrichs–lewy criterion of rotating grids in 2d vertical-axis wind turbine analysis. *Renewable Energy*, 62, 53-62.

- Tullis, S., Fiedler, A., McLaren, K., & Ziada, S. (2008). Medium-solidity vertical axis wind turbines for use in urban environments.
- Untaroiu, A., Wood, H.G., Allaire, P.E., & Ribando, R.J. (2011). Investigation of self-starting capability of vertical axis wind turbines using a computational fluid dynamics approach. *Journal of Solar Energy Engineering*, 133(4), 041010.
- Versteeg, H.K., & Malalasekera, W. (2007). *An introduction to computational fluid dynamics: The finite volume method*: Pearson Education.
- Wang, S., Ingham, D.B., Ma, L., Pourkashanian, M., & Tao, Z. (2010). Numerical investigations on dynamic stall of low reynolds number flow around oscillating airfoils. *Computers & Fluids*, 39(9), 1529-1541.
- Wang, S., Ma, L., Ingham, D.B., Pourkashanian, M., & Tao, Z. (2010). Turbulence modelling of deep dynamic stall at low reynolds number. *Lecture Notes in Engineering and Computer Science*, 2184.
- Wang, Y.-F., & Zhan, M.-S. (2015). Effect of barchan dune guide blades on the performance of a lotus-shaped micro-wind turbine. *Journal of Wind Engineering and Industrial Aerodynamics*, 136, 34-43.
- Wang, Y., Sun, X., Dong, X., Zhu, B., Huang, D., & Zheng, Z. (2016). Numerical investigation on aerodynamic performance of a novel vertical axis wind turbine with adaptive blades. *Energy Conversion and Management*, 108, 275-286.
- Wernert, P., Geissler, W., Raffel, M., & Kompenhans, J. (1996). Experimental and numerical investigations of dynamic stall on a pitching airfoil. *AIAA journal*, 34(5), 982-989.
- West, J.M., Julius, S.H., Kareiva, P., Enquist, C., Lawler, J.J., Petersen, B., . . . Shaw, M.R. (2009). Us natural resources and climate change: Concepts and approaches for management adaptation. *Environmental Management*, 44(6), 1001-1021.
- Wilcox, D.C. (1988). Reassessment of the scale-determining equation for advanced turbulence models. *AIAA journal*, 26(11), 1299-1310.
- Wilcox, D.C. (1998). *Turbulence modeling for cfd* (Vol. 2): DCW industries La Canada, CA.

LIST OF PUBLICATIONS: JOURNAL PAPERS

Shahizare, B., Nazri Bin Nik Ghazali, N., Chong, W.T., Tabatabaeikia, S.S., & Izadyar, N. (2016). Investigation of the optimal omni-direction-guide-vane design for vertical axis wind turbines based on unsteady flow CFD simulation. *Energies*, 9(3), 146.

Shahizare, B., Nik-Ghazali, N., Chong, W., Tabatabaeikia, S., Izadyar, N., & Esmailzadeh, A. (2016). Novel investigation of the different omni-direction-guide-vane angles effects on the urban vertical axis wind turbine output power via three-dimensional numerical simulation. *Energy Conversion and Management*, 117, 206-217.

University of Malaya